A Lidar for Cirrus and Mixed Phase Cloud Studies

Simon André Curtis B.Sc. (Honours)

Supervised by: Murray Hamilton and David Ottaway

Faculty of Science, School of Chemistry and Physics

The University of Adelaide

January 2015

A thesis submitted to The University of Adelaide

as the requirement for the degree of Master of Philosophy

Declaration of Originality:

I certify that this work contains no material which has been accepted for the award of any other degree or diploma in my name, in any university or other tertiary institution and, to the best of my knowledge and belief, contains no material previously published or written by another person, except where due reference has been made in the text. In addition, I certify that no part of this work will, in the future, be used in a submission in my name, for any other degree or diploma in any university or other tertiary institution without the prior approval of the University of Adelaide and where applicable, any partner institution responsible for the joint-award of this degree.

I give consent to this copy of my thesis, when deposited in the University Library, being made available for loan and photocopying, subject to the provisions of the Copyright Act 1968.

I also give permission for the digital version of my thesis to be made available on the web, via the University's digital research repository, the Library Search and also through web search engines, unless permission has been granted by the University to restrict access for a period of time.

Simon André Curtis

31/10/2014

Table of Contents

Table of Figures

List of Acronyms and Symbols

%	Percentage
°C	Degrees Celsius
CALIOP	Cloud-Aerosol Lidar with Orthogonal Polarisation
CALIPSO	Cloud-Aerosol Lidar and Infrared Pathfinder Satellite Observations
CW	Continuous Wave
I	Stokes Parameter - Total intensity
KHz	Kilo hertz
Km	Kilo metre
LIDAR	LIght Detection And Ranging
m	Metre
mA	Milli amp
nJ	Nano joule
MHz	Mega hertz
ms	Milli seconds
ns	Nano seconds
m^{-1}	per Metre
mrad	Milli radian
Q	Stokes Parameter - Degree of horizontal/vertical polarisation
Qt	A C++ development environment
s	Second
U	Stokes Parameter - Degree of oblique polarisation
µs	Micro second
v	Volts
V	Stokes Parameter - Degree of circular polarisation
W	Watt

Acknowledgements

I would like to thank a variety of people and organisations for their direct and indirect contributions to this work. Without them, the quality and quantity of the work done in this project would have suffered.

Firstly my supervisors, Murray Hamilton and David Ottaway, for their expertise and support.

The Australian Antarctic Division for lending us the polarisation equipment. Without it, the depolarisation ratio measurements wouldn't be possible.

NASA for supplying the CALIPSO data, the primary source of validation data.

The Bureau of Meteorology, in particular Samantha Conner, for making their various data products available.

Wyoming University for their radiosonde data archive website.

Ping Yang for supplying the modelled scattering properties of ice crystals dataset (Yang, 2013). Unfortunately, I didn't get to do much with it.

Richard White for constructing the original lidar hardware and software, and then showing me how to use it. I would have had no idea how to write the lidar control program from scratch.

And finally, the workshop support people.

Software used:

MATLAB.

Qt; in particular the QWT library.

Licel Software.

Abstract

Cirrus and mixed phase clouds represent a major uncertainty in climate and weather models. This uncertainty can be reduced with a better understanding of the lifecycle and radiative properties of cirrus and mixed phase clouds, and by inputting local measurements into models. A cloud's radiative properties are dependent on the thermodynamic phase of the cloud particles. Measurements made with a polarimetric lidar can be used to determine thermodynamic phase and improve our understanding of cirrus and mixed phase clouds. Few polarimetric lidar instruments are used in the southern hemisphere, representing a gap in understanding and measurements. An existing lidar instrument was upgraded and run for 6 months; 3 months with polarisation measurements. Important properties such as height, frequency of occurrence and thermodynamic phase have been measured up to heights of around 6 km. These measurements are consistent with ground and satellite based lidar, and with radiosonde measurements. Methods for determining additional properties of the clouds, such as the optical thickness and lidar ratio were researched. Sufficient measurements of cloud macrophysical properties allow for the determination of cloud microphysical properties, such as particle density and shape. To assist with determining these properties a polarimetric lidar simulation was written. Microphysical properties were not determined due to the lidar lacking sufficient range and resolution. Due to the low peak power of the laser used, increasing the range and resolution by increasing the peak power of the laser would be relatively easy.

1: Introduction

1.1: Aim

The aim of this project was to upgrade an existing lidar to study cirrus and mixed phase clouds.

Cirrus and mixed phase clouds are of particular interest due to their poorly understood radiative properties, which are dependent on various properties such as temperature, thickness and thermodynamic phase. These properties are therefore the minimum of what we want to measure. Any additional properties that can be derived from these data, such as particle size, are also of interest for improving our understanding of cloud formation and other processes, and for constraining climate and weather models. While many lidar studies of clouds have been made already, most of the mid latitude studies have been done in the northern hemisphere, which has different properties (such as more land and less ocean) to the southern hemisphere. Therefore, it is important to check if these models are appropriate to the southern hemisphere, which will require local measurements that can be used to validate and improve local models.

In this project, we improved an existing lidar by: doubling the logging range, increasing the pulse energy, narrowing the bandpass filter and adding polarisation detection capability. This required many alterations to the existing lidar setup, including to the control program and post processing software.

As the lidar was worked on, we tested and compared its data with similar data from other sources to ensure the lidar worked as expected, this validation data included: Measurements of cloud base heights provided by ceilometers at local airports. Temperature profiles were obtained from radiosonde data, for thermodynamic phase estimates. Cloud top heights, geometric thicknesses and thermodynamic phase estimates were obtained from the CALIPSO satellite instrument, CALIOP.

1.2: Background and Motivation

1.2.1: Clouds

The role of clouds in the atmosphere includes absorbing and reflecting thermal radiation, absorbing and releasing heat during phase changes, and contributing to the hydrological cycle by producing precipitation.

The atmosphere consists of multiple layers classified by their change of temperature with height. The lowest section of the atmosphere is called the troposphere and is characterised as having temperature decreasing with increasing height. The layer above the troposphere is called the stratosphere and has increasing temperature with height. The boundary between these two regions is called the tropopause. The height of the tropopause ranges from around 9 km at the poles to 17 km at the equator. The majority of weather phenomena occur in the troposphere.

Cirrus clouds occur high in the troposphere, often just below the tropopause. They are thin, both physically and optically, and tend to appear as faint wispy strands (Sassen and Wang, 2008). Recent satellite observations show that cirrus clouds cover at least a third of the earth's surface at any one time (Dupont *et al*., 2010), making them an important factor in the radiation budget of the atmosphere. Optically thin cirrus clouds are widespread across the globe and do not just occur in the tropics, as was previously assumed (Sassen and Wang, 2008). Powerful optical instruments are required for accurate profiling of these (sub visual) cirrus clouds because of their optical thinness and height.

Clouds form when the relative humidity of an air mass reaches 100%. Droplets precipitate because the air can no longer hold them as a vapour. A recent analysis suggests that cirrus morphologies can be linked to the mechanism of their formation (Dionisi *et al*., 2013). Natural cirrus cloud formation mechanisms are classified into two main groups. First, cirrus clouds are formed due to the transport of moist air to the upper troposphere, such as in cyclone and anvil outflow, fronts or gentle uplift. Second, cirrus clouds are formed due to temperature perturbations in the proximity of the tropopause. Sources of these perturbations include a variety of atmospheric waves and volcanic eruptions. Interactions between planetary scale waves and cirrus cloud formation were recently studied over Taiwan (Das *et al*., 2013) and over the tropical Indian Ocean (Suzuki *et al*., 2013).

A third type of cirrus formation is caused by aircraft: contrails. These are not only formed from the moisture content of the exhaust, but also from seeding by particulates in the exhaust or even the disruption to the air as the aircraft moves through it. Sometimes contrails do not fade quickly, but spread out forming a unique type of cirrus cloud. The existence of contrail cirrus clouds are known to have an effect on climate through their effect of the radiation budget (Minnis *et al*., 2013).

A poorly understood aspect of clouds is the occurrence of mixed phase clouds (Shupe *et al*., 2008). Mixed phase clouds are composed of a mixture of both water droplets and ice crystals, at temperatures below 0°C. Ice and liquid water can exist in clouds simultaneously provided that the temperature remains between 0°C and -38°C (Rosefeld and Woodley, 2000). Liquid water droplets that are below 0°C are called supercooled droplets, which cause dangerous icing to aircraft by freezing instantly on contact with the aircraft. When droplets cool down to -38°C they will freeze instantly, in a process called homogenous freezing.

Freezing of water droplets above -38°C occurs when a water droplet comes in to contact with aerosol particles called ice nuclei (or when a water droplet is cooled enough for an ice nuclei it already contains to function). These nuclei act as a catalyst for the transition from liquid to solid, and are then trapped inside the ice (Rosefeld and Woodley, 2000). Ice nuclei differ from cloud condensation nuclei in that they are relatively effective at catalysing the freezing transition, rather than the condensation transition. A lack of potential nuclei is thought to cause droplets to remain in the liquid state below 0°C. The southern hemisphere has less land mass than the northern hemisphere, supplying the atmosphere with fewer potential ice nuclei. Air traffic, which produces aerosols, is also more common in the northern hemisphere. This leads to a greater frequency of clouds containing supercooled water droplets in the southern hemisphere (Kanitz *et al*., 2011), thus making it easier to study such clouds in the southern hemisphere. A greater frequency of mixed phase clouds makes understanding their radiative properties more important in the southern hemisphere.

1.2.2: Effect on Climate

Cirrus clouds have been recognised as important regulators of the radiative balance of the earth-atmosphere system (Twomey, 1991), (Thorsen *et al*,, 2013). Higher thinner cirrus clouds are colder and tend to induce a net warming effect by trapping more heat than they radiate into space, whereas lower thicker cirrus are warmer and tend to improve cooling by

radiating more heat into space than they trap. To understand and model the effects of these clouds on climate, detailed information about the distributions of cirrus clouds around the world, their altitudes, densities, particle shapes and thermodynamic phases are needed. Understanding of thermodynamic phase is critical for two reasons. Firstly, the radiative properties of a cloud are related to a variety of properties including crystal habit or droplet size (Baran, 2012). Secondly, the latent heat released or absorbed by a phase change can be a significant driving force in the atmosphere (Franklin *et al*., 2013). This dependence of radiative properties on thermodynamic phase makes it difficult to estimate the radiative properties of mixed phase clouds.

Anthropogenic clouds also affect the climate in ways not fully determined (Minnis *et al*., 2013). Contrail cirrus clouds have higher optical thicknesses and lower particle sizes than naturally formed cirrus clouds in similar locations. Natural cirrus clouds can also have their properties altered by the presence of a contrail, without altering the appearance of the cloud (Minnis *et al*., 2013). This makes it harder to define the full effects of aviation on the radiative balance of the atmosphere (Minnis *et al*., 2013). The report of the International Panel for Climate Change (IPCC, 2007) demonstrated that errors in the estimation of cirrus cloud radiative impact are still one of the largest sources of uncertainties in global climate models. Despite this, little work has been done to improve parameterisation of cirrus in the southern hemisphere at mid-latitudes. It is essential to document cirrus altitude and vertical extent at different geographical locations to improve their parameterisation in numerical models and decrease uncertainties in climate prediction (Hoareau *et al*., 2013). Another important relationship between cirrus and climate is how changes to the climate affect cirrus formation. Therefore, climate modelling requires improved characterisation of cirrus formation processes (Nazaryan *et al*., 2008).

1.2.3: Interaction with Aerosols

Aerosols are any solid or liquid particles suspended in air. Aerosols strongly influence the formation of clouds by acting as nuclei for condensation of water vapour or freezing of water droplets (Rosefeld and Woodley, 2000). In addition to water, other aerosols found in our atmosphere include mineral dust, ash, sea salts, pollen, spores and bacteria (Cziczo *et al*., 2013). High levels of aerosols can lead to the formation of clouds that have smaller, more numerous droplets/crystals (Twomey, 1991). More numerous particles cause clouds to have

higher reflectivities. In addition to dust being carried by winds and human created pollution, volcanos also have a significant contribution to the global aerosol content (Robock, 2000). However, their sporadic nature makes them harder to study. The increasing instrument sensitivity and layer classification methods have demonstrated the study of aerosol and cloud interactions, and a recent study undertaken in the Amazon Basin found increased cloud geometric thickness correlated with high levels of aerosols (Manoj *et al*., 2012).

1.2.4: Lidar Techniques

LIDAR (LIght Detection And Ranging) is a method for detection and analysis of thin cirrus clouds and aerosol layers. This involves firing a laser pulse at the target and measuring the strength and delay of the returned light. This gives a measurement of the backscatter coefficient of the atmosphere at specific heights and the integral of the extinction coefficient up to that height (Klett, 1981). The backscatter coefficient describes how much light per unit length is scattered in the 180° direction and the extinction coefficient describes how much light per unit length is scattered in any direction or absorbed. However, separating these values solely with lidar measurements has previously been demonstrated to be difficult (Klett, 1981). An important value is the lidar ratio, which is the extinction coefficient of a layer divided by its backscatter coefficient. As such, it is an indication of the scattering properties of the detected medium (Ansmann *et al*., 1992). The lidar ratio varies from cloud to cloud and could be variable inside a single cloud. Since the lidar ratio is the ratio of the total amount of scattered light to how much light is scattered in the 180° direction, it is therefore 4π divided by the value of the scattering phase function at 180° (Josset *et al*., 2012).

A variety of properties can be determined from a lidar profile. Boundaries of clouds and therefore the thickness, position and persistence of clouds can be distinguished by changes in the strength of the returned light. With the inclusion of additional information about the atmospheric conditions (from measurements or models), previous studies have determined the optical thicknesses of these clouds (e.g. Chen *et al*., 2002). By measuring the depolarisation of the returned light, the thermodynamic phase of the scatterer can be estimated. The laser pulse starts with 100% linear polarisation, so the ratio of different polarisations of the returned light is a measure of the change in polarisation of the light, which is termed the depolarisation ratio (Allemand, 1970). The depolarisation ratio is heavily dependent on the shape (and therefore thermodynamic phase) of the cloud particles, and on

multiple scattering effects. Multiple scattering is when a photon scatters off multiple particles before it is detected. The depolarisation ratio and the lidar ratio have been demonstrated to characterise the different shapes of ice crystals in a cloud (Sassen and Cho, 1992). A recent study has shown that exploiting the multiple scattering effect on the depolarisation ratio allows determination of the liquid particle size and liquid water content of a cloud (Kim and Lee, 2014), however it requires a resolution of approximately 10 m.

Lidar measurements have been obtained in conjunction with other measurement technologies to increase the range of properties quantified. An early study used a combination called LiRad which involved using a passive radiometer to determine the optical thickness of the cloud being measured with the lidar (Platt, 1973). Once the optical thickness was determined, being the integral of the extinction coefficient over the cloud; the lidar ratio was calculated. Collocating a 35 GHz radar with a lidar allows the determination of the size and amount of ice particles in a cloud, by exploiting the different dependencies on particle sizes for the two instruments (Shupe *et al*., 2008).

Three types of scattering are involved in atmospheric lidar systems, namely Rayleigh, Mie and Raman. Rayleigh scattering is the elastic scattering of the photons by atmospheric molecules, which are smaller than the laser wavelength, providing a background signal at heights without clouds. This is often referred to as the clear air signal, and it is a useful value for determining extinction. Mie scattering is the elastic scattering of the photons by aerosols/cloud particles, which are of comparable size to the laser wavelength. This scattering is the dominant return signal from the clouds. Raman scattering is any inelastic scattering. This inelastic scattering causes a change in the wavelength of the backscattered photons. Raman detection requires more complicated detection equipment, but can make a direct measurement of the extinction ratio, and the temperature at different heights. The Mie scattering signal provides information as to the location of the clouds. However when combined with the Rayleigh or the Raman signal, the optical thickness and lidar ratio of a cloud can be determined. A combined Rayleigh-Mie-Raman lidar has previously demonstrated its effectiveness in the characterisation of cirrus clouds (Dionisi *et al*., 2013).

Satellite based lidar provide different coverage to ground based lidar. They have good spatial range; however provide poor spatial and temporal resolution. In contrast, ground based lidar has demonstrated high spatial and temporal resolution, but low spatial range. Combined use of these two types of lidar covers both ends of the range/resolution spectrum.

1.2.5: Recent Studies of Interest

Some recent cloud studies using lidar that took place at similar latitudes to Adelaide are (Kim *et al*., 2014, Wang *et al*., 2013, Lakkis *et al*., 2011 and Lakkis *et al*., 2009), though two of the three locations are in the northern hemisphere. They give an indication of how high cirrus clouds are expected to occur at this latitude (34°55'44.4"S). Such studies also demonstrate what can be done with lidar data and how.

Another recent publication uses CALIOP (a satellite instrument. See 1.3.1: CALIOP) data to look for anti-correlations between different species of aerosol clouds and supercooled water clouds (Tan 2014). The study also compares super cooled water cloud frequencies between the northern and southern hemispheres, and also between continental and oceanic clouds. The study finds an increased amount of supercooled water in the southern hemisphere.

An Australian perspective on the effects of aerosols on clouds was made by Rotstayn *et al*. (2009). This study finds that aerosol emission from around the world, including from the northern hemisphere, has an effect on the climate in Australia. It also highlights the high uncertainties in our understanding and measurements of aerosol effects.

Another interesting publication is (Kim and Lee, 2014). It shows that the multiple scattering effect on depolarisation measurements inside a liquid water cloud can be used to determine the extinction coefficient, liquid water content and droplet effective size. These methods are potentially usable with the data from our lidar. This would provide a method of calculating the extinction coefficient of a cloud, and hence the optical thickness.

1.3: Data Validation Sources

1.3.1: CALIOP

In 2006 the CALIPSO (Cloud-Aerosol Lidar and Infrared Pathfinder Satellite Observations) satellite was launched and became part of the A-train satellite group, a cluster of atmospheric sensing satellites in the same orbit (Vaughan *et al*., 2009). It carries the CALIOP (Cloud-Aerosol LIdar with Orthogonal Polarization) instrument, which is a lidar with depolarisation measuring capabilities. Since its instigation, many studies have used the data from this instrument to investigate clouds on a global scale (Hlavka *et al*., 2012). However, a comparison study between CALIPSO data and a ground based Raman lidar determined that CALIPSO was unable to detect some thin cirrus clouds during the day and misinterprets the thickness of those clouds it does detect (Thorsen *et al*,, 2013).

The work done for this thesis was undertaken in the city of Adelaide, South Australia, Australia (34°55'44.4"S 138°36'3.6"E). Adelaide is located half way between the ground tracks of two adjacent CALIPSO night-time passes (see Figure 1 and Figure 2), therefore collocated measurements are unable to be obtained. However, there is minimal ground based minimal obstruction between Adelaide and the western ground track meaning that similar clouds were observed in both locations. There is a range of hills between the lidar and the Eastern ground track, it was observed that the clouds were similar in both cases meaning that the hills did not significantly affect the high clouds that are relevant to this study The two ground tracks meant that two comparisons could be made every 16 days instead of just one, doubling the number of potential comparable measurements. The satellite passes are at approximately the same time of day each pass, of around 1:40 am.

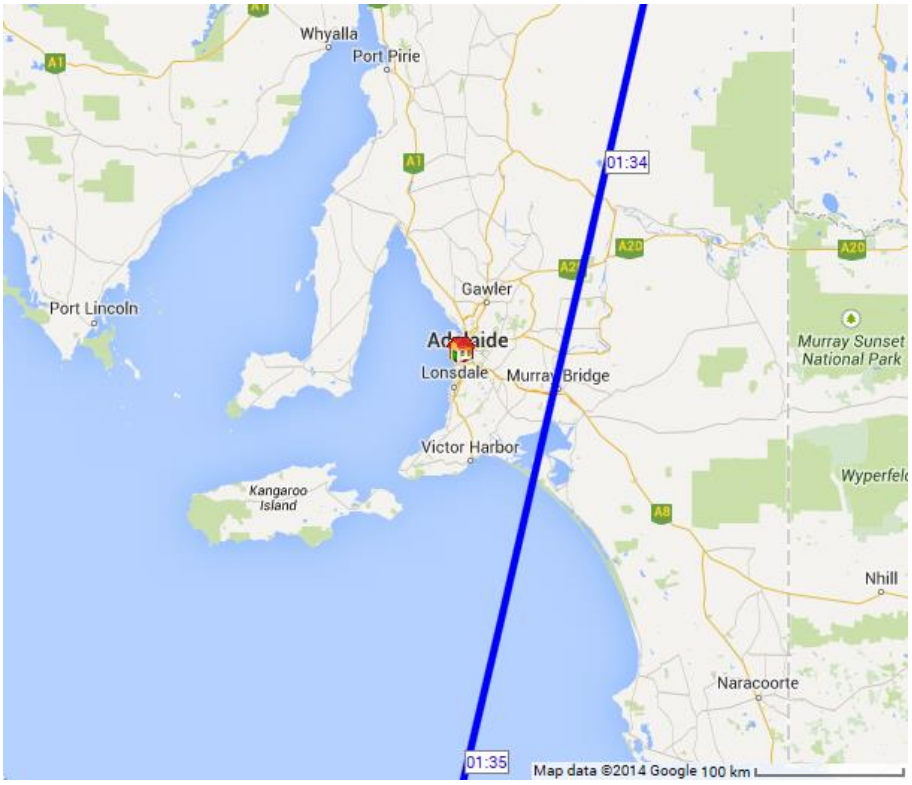

Figure 1: The ground track of the eastern of the two CALIPSO satellite overpasses. The times show when it passes over and give an indication of how fast the satellite moves. (Source: www.n2yo.com)

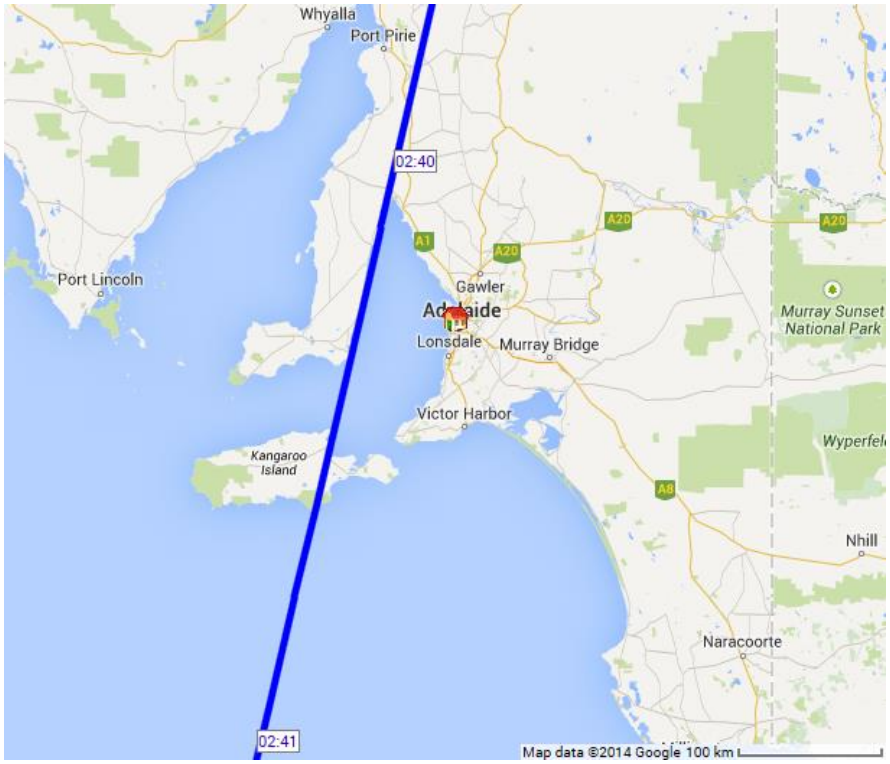

Figure 2: The ground track of the western of the two CALIPSO satellite overpasses. Note that these times now reflect the local summer time, so they are one hour ahead of the times in the previous image. (Source: www.n2yo.com)

1.3.2: Airport Instruments

The Bureau of Meteorology run a variety of instruments at the nearby Adelaide Airport (latitude: -34.95, longitude: 138.53), two of which are used to validate the data from this lidar. These two instruments are a ceilometer and regular radiosonde launches. The airport is located 7 km away from the lidar.

A ceilometer is a weak lidar instrument that is designed to measure the height of the base of the first cloud above the ground. These data was used to validate the cloud height measurements.

A radiosonde is a device that is attached to a weather balloon that measures various atmospheric properties as it rises. These include wind speed and direction, air pressure, temperature and humidity. Wind speed and direction data was used to estimate the delay between a cloud intersecting the CALIPSO ground track and the lidar. Humidity data was used to verify that a cloud is likely to exist at the heights detected. Temperature data was used to validate ice detection.

1.4: Thesis Outline

This thesis describes the work done on improving an existing lidar in both hardware and software, the results given by the improved lidar, and a lidar simulation. Chapter 2 describes the main upgrade before the polarisation detection capability was added. This includes what was done to the hardware and software, the validation measurements, a results overview and specific interesting cases. Chapter 3 describes the polarisation detection equipment and software changes in addition to validation measurements, result statistics and some case studies. Chapter 4 describes the lidar simulation programs and presents some initial results. Chapter 5 reviews what has been achieved and compares this with the goals. Recommendations are made about how to move forward.

2: Main Upgrade

This chapter describes the non polarimetric improvements to the lidar hardware and software. It begins with a general overview of the original lidar and describes the hardware and software changes to the system. Then there is a comparison of the data from before and after this upgrade, followed by an overview of the measurements collected and case studies including the validation measurements. It finishes with a method of how to derive a cloud's optical thickness and lidar ratio using the lidar data and presents some results from applying this to the data collected with this instrument.

2.1: Methods and Instrumentation

2.1.1: Overview

A lidar is an active remote sensing instrument, so it consists of a transmitter and a receiver. The transmitter is a laser diode with a lens and mirrors. The receiver is a telescope and a photomultiplier tube. To control these devices, there is a timing system and a computer. The timing system generates pulses at set intervals to trigger the various devices. The computer is used to display and store the data.

The lidar equipment used in this work was placed on a moveable trolley, to keep the lidar as mobile as possible. This included the receiver equipment (telescope, polarisation rotator, photomultiplier tube and Licel data acquisition system), the transmitter equipment (laser mount, lens and mirrors) and the driver equipment (power supply, pulse generator, temperature controller and laser driver). The computer that runs the control program was placed on a small table to the side, along with the screen of an infra-red camera. This infra-red camera was used to assist with coarse alignment of the lidar. Wooden blocks and spacers placed under the trolley frame were used for alignment by keeping the lidar flat, since the trolley wheels had deflated unevenly. A timer switch was used to turn off the laser and photomultiplier tube during the day, to protect lab users from the laser and the photomultiplier tube from the sun.

The trolley and computer were kept inside a lab in the Braggs building, which has roof hatches that could be opened to allow direct access to the atmosphere (Figure 3). A glass skylight was constructed to fit over the roof hatch frame, allowing the lidar to be used in all weather. The skylight was made from non-toughened float glass, as the toughening process leaves strains in the glass that would disrupt the polarisation of light passing through it.

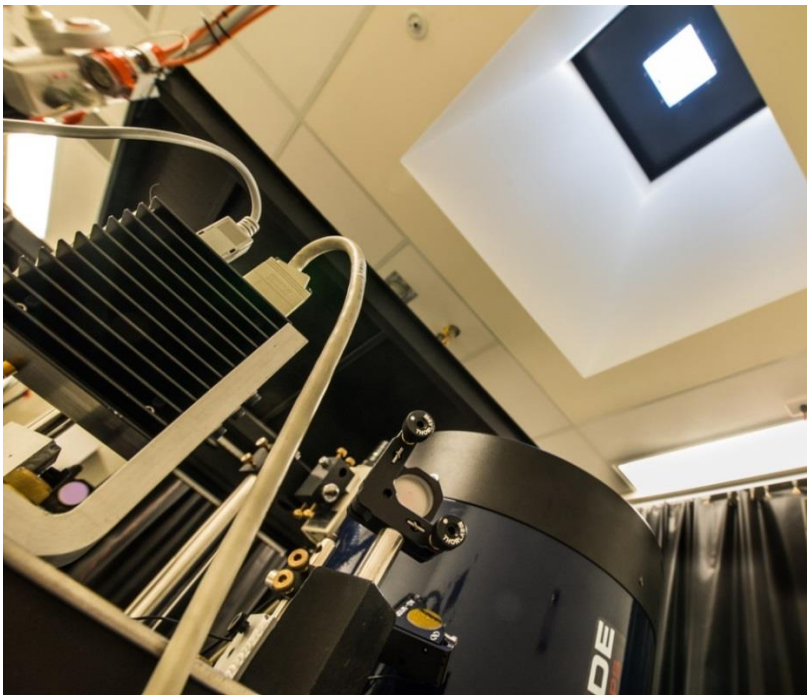

Figure 3: Photo of equipment and roof hatch. The laser mount and mirrors in the bottom left, telescope in the bottom centre, and the roof hatch in the top right.

2.1.2: Physical Components

Lidar Overview:

The original lidar system used an acousto-optic modulator to generate a train of pulses from an 808 nm CW laser source. These pulses were reflected into the sky with a mirror. The returned photons were collected using a 14 inch telescope, directed through a 10 nm bandpass filter, and counted by the photomultiplier tube, in photon counting mode. These counts were recorded by the Licel transient recorder, which summed them into 50 ns (7.5 m) bins. The data was transferred to the computer after the returns from 4096 pulses had been summed (which takes just over a second). The original lidar logged data up to 7 km, but only received a faint signal return from above 6 km. A schematic illustrating the final operation of the lidar is given in Figure 4.

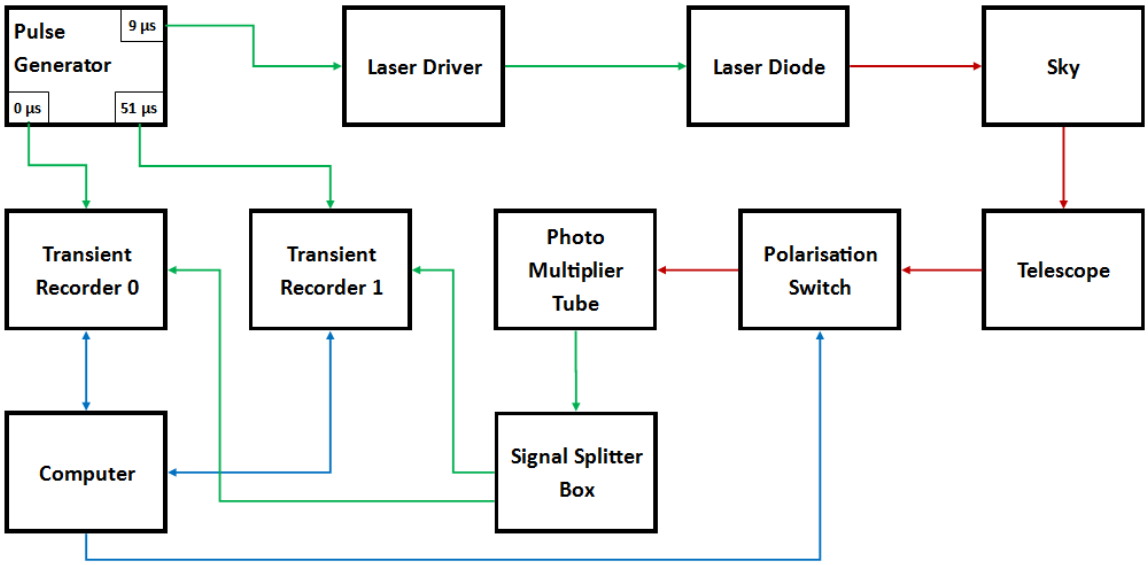

Figure 4: Schematic of operation of the lidar. Green links represent electrical impulses. Red links represent optical impulses. Blue links represent digital communication. The times on the Pulse Generator are the different delays of the pulses.

Cirrus measurements require two criteria to be met: Firstly, the return signal from the clouds at cirrus cloud heights is sufficiently above the background noise. Secondly, the data acquisition system needs to be recording at a delay that corresponds with cirrus cloud heights.

The returned signal strength was increased by increasing the output power of the laser. The acousto-optic modulator was removed and a square wave was fed into the ‘mod in’ port of the laser driver (Thorlabs LDC 205). Unfortunately, this generated pulses with a long rise/fall time of around 1 µs. As pulse energy was deemed more important than spatial resolution, a pulse length of 1.5 µs was used. This decreased the spatial resolution from 150 m to 225 m. The new energy of the pulse was 125 nJ, up from 45 nJ, which corresponds to a 2.5 times increase in the signal to noise ratio. The loss of resolution was corrected later when a new laser driver was constructed to produce square pulses of 125 nJ but with the pulse length reduced back to 1 µs.

Background light noise was reduced by changing the laser diode from one with a wavelength of 808 nm to one with a wavelength of 829 nm, to match a 1 nm bandwidth filter that replaced the 10 nm bandwidth one. This reduced the background light noise by a factor of 10.

The logging equipment of the original system did not record up to the full height at which cirrus clouds could occur at the study location, which is up to 12-15 km, depending on the season. The range of the Licel TR20-10 transient recorder was 7680 m, so two were used in combination to increase the range to 15 km. The second recorder was triggered at a suitable delay for taking over after the first recorder stops. The first recorder is triggered 10 μs before the laser is fired, so that a measurement of the background noise can be made and removed from each shot (see Table 1). This reduced the effective height range to 13 km. It was discovered that the two transient recorders have different sensitivities, so the background measurement had to be done once for each recorder. The background measurement for the second recorder is done above 13 km, where the return signal should be negligible. It is also possible to use the second memory register of a transient recorder for logging higher range data; however this could cause a small gap to appear in the height range as you cannot trigger the second memory while it is summing the data it just collected into the memory.

Timings Table:

Delay	**0 μs**	**10 μs**	**51 μs**	**102 μs**
Effective Height	-1500 m	0 m	6150 m	13800 m
Action	Transient Recorder 0 starts recording.	Laser pulse fired.	Transient Recorder 0 stops and Transient Recorder 1 starts.	Transient Recorder 1 stops recording.

Table 1: This table displays the delays used to manage the transient recorders, and the effective heights that these delays correspond to.

Laser Driver:

A new laser driver was built since the existing device was not capable of producing current pulses with a fast enough rise/fall time. This new laser driver uses an EL7158 ultra-high current pin driver chip to send 1 µs long pulses of 250 mA into the laser diode (see Figure 5). This is overdriving the diode by 25%, but it gives 125 nJ pulses and the low duty cycle of 0.4% prevents diode failure. The resulting laser pulse had a rise time of 200ns and a fall time of 100ns. The response time could be made even faster by connecting pin 8 of the chip to ground. This was not done as these chips are sensitive and can be destroyed by having a voltage difference between pin 8 and pin 6 of greater than 10 v, nor was a faster response time needed. Because the circuit uses a positive ground, the +5 v trigger pulse from the pulse generator was not triggering the switching. A simple pre-amplifier was added to the driver box. However, this introduced an extra 1 µs delay, so the triggering pulse is generated 1 µs earlier. If the laser driver box is rebuilt, it should be possible to adjust the circuit and remove the need for the pre-amplifier and hence remove the extra delay.

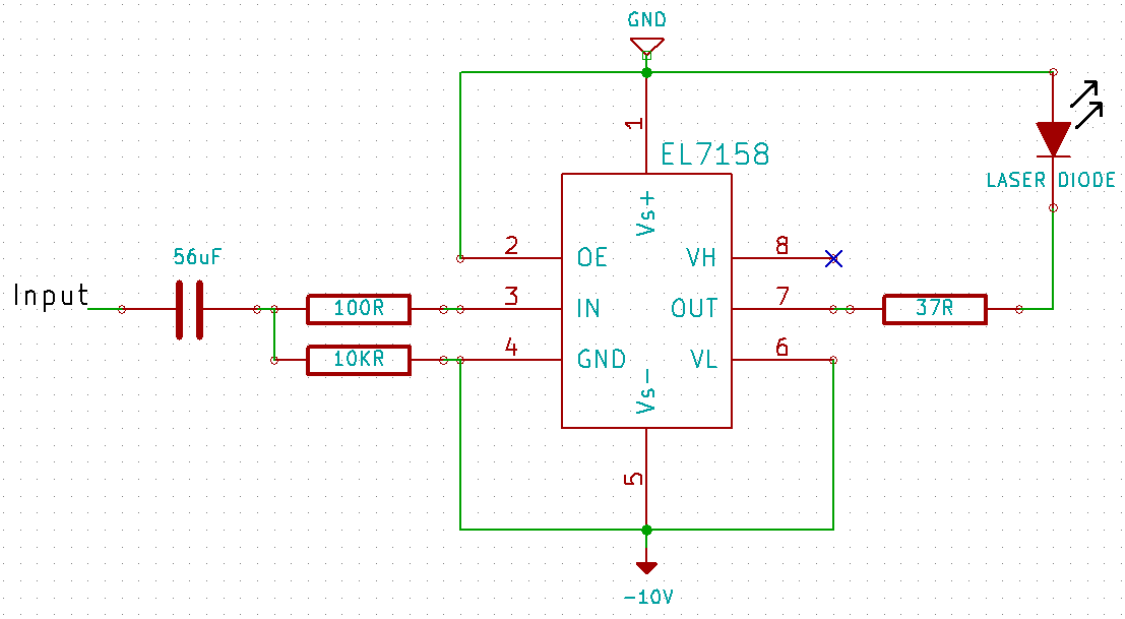

Figure 5: Schematic of the new laser driver circuit, without the preamplifier. Red represents electronic components. Green represents connections.

Pulse Generator:

A pulse generator was assembled to produce all the required trigger pulses. A 1 µs long pulse was required for the laser pulse, so a 1 MHz crystal oscillator was chosen to be the clock to base the timings on. This 1 MHz pulse train was fed into an 8 bit ripple counter chip, allowing digital counting up to 256 µs. Logic gates are used to generate 4 pulses at specific delays: 0 µs delayed pulse to trigger the first transient recorder. 9 µs delay for the laser driver (an extra 1 µs delay is added by a preamplifier). 51 µs delayed pulse to trigger recorder 2. 250 µs delayed pulse to internally reset the counter and lock the frequency to 4 kHz.

2.1.3: Software Components

Lidar Control Program:

The original lidar program was written by Richard White, using Qt, a C++ development environment. The program takes care of all communication with the Licel box; such as changing settings and reading data, via TCP-IP. It saves and displays the data to the screen. It also has a delayed stop function, allowing the user to start up the lidar and have it automatically turn off when desired, without the user being there.

The program displayed the data as three graphs (

Figure 6: A screenshot of the lidar control program showing the new logarithmic scale function in use.

). First, there is a plot of the last received data from the Licel box, displayed as a line of return counts versus height (top left). Second, there is a temporal running average of the first graph, over a user specified averaging range (bottom left). Finally, all the data collected in that run is displayed as a colour contour graph, with the colour axis set as a logarithm (or linear) of the signal count above the background level (right).

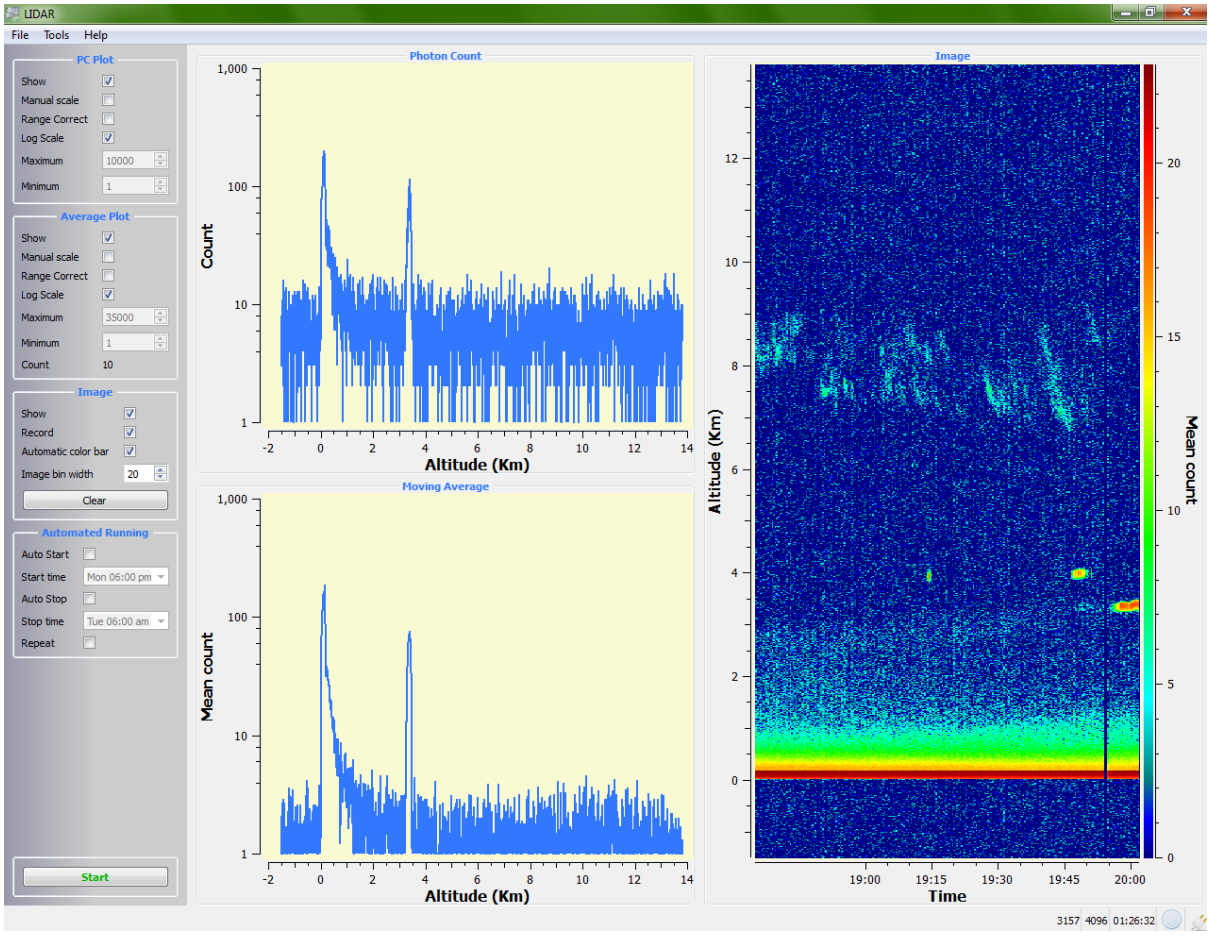

Figure 6: A screenshot of the lidar control program showing the new logarithmic scale function in use.

The first adjustment made to this program was to add in the ability to read from two transient recorders, when they are being used to double the height range. This was done by enabling and reading data from the second recorder, and appending it to the data from the first recorder. The rest of the program was then altered to accept data covering double the height range. Additionally, some ease of use functions were added; the main being the delayed start and automated running settings, which tells the program to turn on and off automatically at set times every day. This required a small alteration to how and where the program saved the data. Some extra buttons were also added to the instantaneous and running average graphs, to enable/disable logarithmic return count scales or a range squared correction. Since there was another ongoing lidar project which used a Licel data acquisition system some settings were added to the program that allow it to work correctly with different transient recorders.

Matlab Script:

Richard White wrote a Matlab script that imports the data files from the control program into Matlab, for visualisation or further processing, such as summation in the time domain. This was altered to read and process the doubled height data. Extra settings for adding a range squared correction and applying a low-pass Gaussian filter to the data/plot was also included in the program.

The adjusted script worked as follows (Figure 7): It loads a single run of data and reduces the time resolution of the data to a specified amount. 30 s or 60 s was used for producing plots or 1 hour when numbers were wanted for further calculations. Next the data is filtered with a low pass Gaussian shaped filter, to smooth background noise. The 'averaging' field controls the standard deviation width of the Gaussian. 1 (a full width at half maximum of 2 pixels) was used when the time bin was set to 30 or 60 seconds and no cirrus clouds were detected. Higher values can make faint cirrus more visible, but reduce detail. Finally, a zero correction is used to remove the ambient background noise; this is done by averaging a section of data where no return signal exists. As the two transient recorders had different sensitivities, this was undertaken in two halves. The lower half of the data uses the background measured during the 10 µs delay before the laser is triggered. The upper half is corrected using the top 1 km of data, as any signal above 13 km is unlikely at this pulse energy. Care is taken not to use data too close to the ends of the top or bottom of the height range, as these get distorted by the effect of the filtering around the edges. The data was then plotted on a pseudo colour plot with the signal strength on a logarithmic or linear scale.

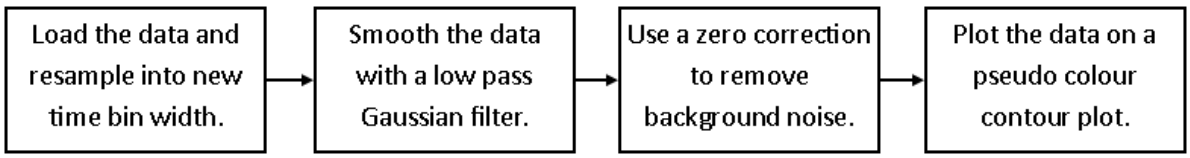

Figure 7: Flowchart of the MATLAB processing script.

2.2: Results

2.2.1 Comparison:

A comparison was made between plots of the data before (Figure 8) and after (Figure 9) increasing the pulse energy. Figure 8 shows a thin cloud layer at 3-4 km with rain falling before 00:00. After 00:00 the cloud layer has thin strips of signal return directly above it, this suggests that the laser pulse is being fully attenuated and that the full thickness of the cloud was occulted. Figure 9 shows a similar layer of cloud. In patches where the cloud was relatively thin, there is no indication of incomplete penetration of the pulse. The clear air signal also reaches higher that it does in the pre modification data.

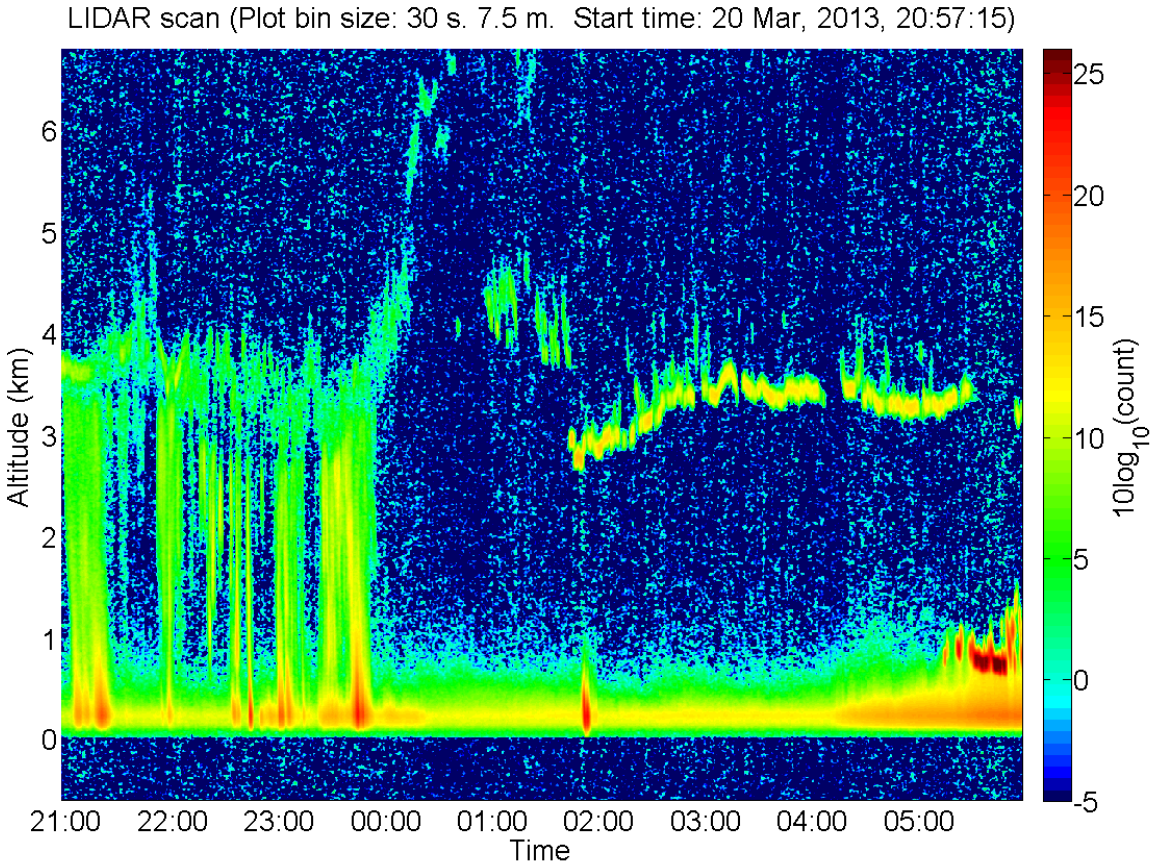

Figure 8: Lidar data from the night of the 20th of March 2013, from the original lidar. This is a plot of signal strength as a logarithm on the colour axis, versus height (y axis) and local time (x axis). These data shows a cloud layer measured between 3 and 4 km, with precipitation falling until 00:00. The same layer after 00:00 had streaks of return from above it; this suggests that the laser pulse is not fully penetrating the cloud. A faint signal from a cloud around 6 km happens around 01:00. The signal return stretching from 0 to almost 1 km is due to scattering by aerosols and air molecules. Note that all plots of lidar data are in local time, not universal time.

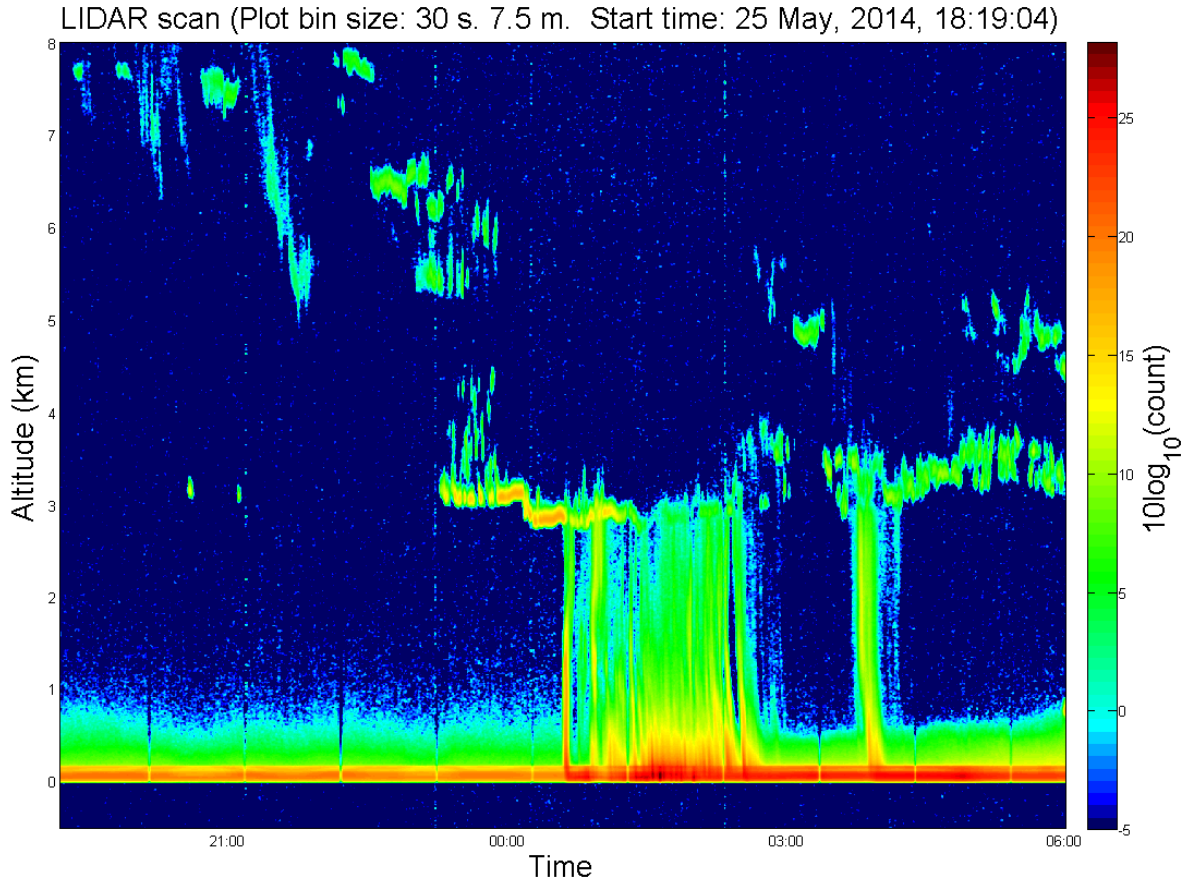

Figure 9: Data from the 25 of May 2014, a night with similar weather conditions to the data collected before the pulse energy increase. There was a similar cloud layer at 3 to 4 km, which does not appear to have fully attenuated the laser pulse, and some clouds detected up to heights of 8 km. Also of interest is the increased strength of the clear air signal, which is not obscured by the background noise until around 1 km. Times are in local time, not universal time.

2.2.2 Statistics:

To quantify cloud detections, each night was divided into 1 km height and 3 hour time bins. The time bins were 18:00-21:00, 21:00-00:00, 00:00-03:00 and 03:00-06:00. If the signal return indicated a cloud existed inside the bin, then it was counted as a detection at that height. The number of detections at each height was then summed for each month, and normalised into an average nightly occurrence fraction (see Figure 10). The resulting profile for April has three peaks in the frequency, at 1, 4 and 9 km. The profiles for May and June appear bi-modal with a low cloud peak around 1 to 2 km and the high cloud peak around 7 km. The highest occurrence fraction for the low cloud peak was in June with cloud almost 60% of the time at 1 km, while the lowest peak occurrence fraction value was in May with cloud around 30% of the time at 2 km. The high cloud peaks decreased in fraction and height from April to June, with the peak height decreasing from 9 km to 7 km. A reduction in the number of high clouds is expected, as the increased number of low clouds would obscure higher clouds. Also as the atmosphere contracts in winter, the tropopause lowers, and would likely reduce the height of the high cloud peak. If the clouds were divided into sharp edged and diffuse edged clouds (not shown), the sharp edged clouds would dominate the low cloud peak and the diffuse shaped clouds would dominate the high cloud peak, suggesting that the sharp edged clouds contain liquid, while the diffuse edged clouds are composed of ice.

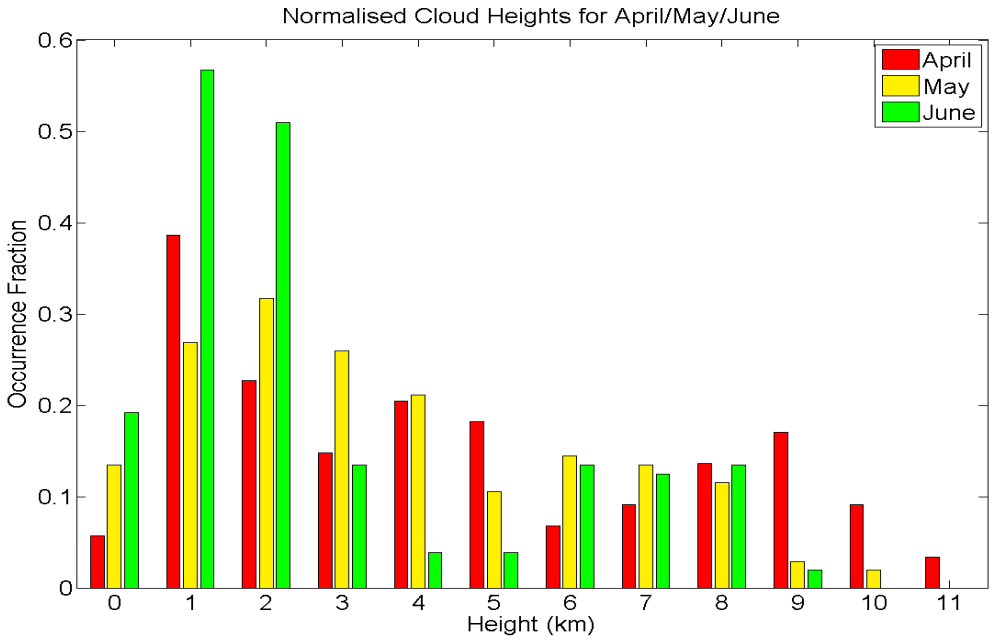

Figure 10: Normalised cloud occurrence fractions at different heights for the months of April, May and June. Cloud heights were counted for each quarter of each night, and the data was summed for each month and then normalised into the fraction of time a cloud was detected at each height. The resulting profiles show a strong peak in frequency around 1-2 km and a weaker peak at 7-9 km.

2.2.3: CALIOP Comparison Summary

A total of nineteen comparable measurements between the post-modification lidar and the CALIOP instrument were collected between April 1st and September 31st, 2014. Details of these comparisons are given in Table 2. Allowing for a plus or minus 1 km variation in cloud boundary locations due to the 1 hour time difference between the measurements, the lidar and the CALIOP instrument were mostly in agreement about the vertical edges of the clouds. Disagreements only occurred when clouds were thick enough to block the signals from one or both instruments. The only other disagreement was due to a cloud being above the detection range of the lidar. For an example of thick clouds, see case 2 of the Satellite Comparison case studies (page 27).

Date	CALIOP Cloud Base (km)	Lidar Cloud Base (km)	CALIOP Cloud Top (km)	Lidar Cloud Top (km)	Lowest CALIOP Return (km)	Overlap	Agreement
15th April	9	9	11	11	0	Good	Good
24th April	2	2	2	2	0	Good	Good
1st May	1, 6	1	4, 10	4	1	Bad	50%
10th May	0	0	1	1	0	Good	Good
17th May	4	4	6	6	4	Bad	Good
26th May	4	0	6	0	4	Bad	Bad
2nd June	1	1	2	2	1	Bad	Good
11th June	5	5	10	7	5	Bad	50%
18th June	5	5	9	7	5	Bad	50%
27th June	1	1	2	4	1	Bad	50%
4th July	1	1	1	2	0	Good	Good
13th July	7	6	11	8	7	Bad	50%
29th July	1	0	1	1	0	Good	Good
5th August	nil	nil	nil	nil	0	Good	Clear
14th August	nil	nil	nil	nil	0	Good	Clear
30th August	9	nil	11	nil	0	Good	Bad
6th September	nil	nil	nil	nil	0	Good	Clear
15th September	1	1	1	2	0	Good	Good
22nd September	nil	nil	nil	nil	0	Good	Clear

Table 2: Details of CALIOP comparison events. Cloud boundaries and return heights are given in km. A cloud height of nil refers to no clouds being detected for that event. Lowest CALIOP Return refers to the height at which the CALIOP instrument receives no signal below for each event. As of the 13th of July the lidar was reduced from 12 km to 8 km by the polarisation equipment. This is why it failed to detect the cloud on the 30th of August.

2.3: Case Studies

2.3.1: Aerosol Layer

In addition to detecting clouds, the modified lidar can also detect thick aerosol layers just above ground level (Figure 11). Aerosol layers only return a small fraction of the signal that a cloud does. This makes them appear very faint and only visible as perturbations of the clear air background. Any returned signal from an aerosol layer will have a very low depolarisation ratio of around 0.1, since they are effectively spherical relative to the laser wavelength, though this instrument doesn't usually receive a high enough signal for a clear measurement of the depolarisation ratio of aerosols.

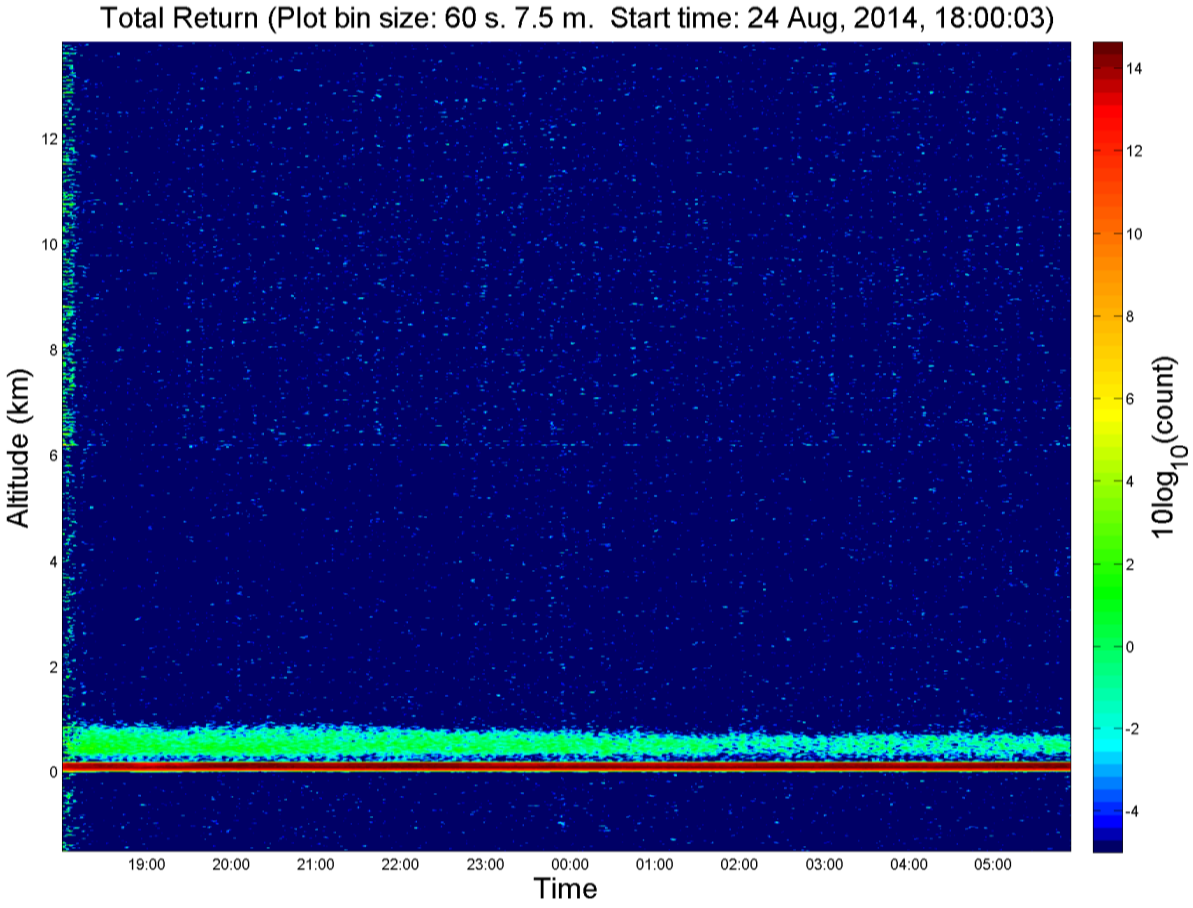

Figure 11: Lidar data for the night of the 24th of August, 2014. It shows a thick aerosol layer at ground level. It was trapped under an inversion layer during a still period, and persisted for a few nights. The red bar, seen clearly in this figure, is interference from the laser driver. Times are in local time, not universal time.

2.3.2: Ceilometer Comparison

After the first major modification of the lidar, the data (Figure 9, page 20) was compared with the data from the ceilometer instrument (Figure 12) and data from a radiosonde (Figure 13), both from Adelaide Airport (7 km away, latitude: -34.95, longitude: 138.53). This was done to verify that the modification did not produce anomalous results. The lidar measured the cloud base to be at 5 km, whereas the ceilometer measured the cloud base of the same cloud to be at 5.5 km. This discrepancy is acceptable, due to the different locations of the instruments, the 200 m (at the time) resolution of the lidar and, and lack of clear edges to the cloud. Further the ceilometer is a weaker instrument and wouldn't have received a strong signal from the edge of the cloud, but would at the thicker part of the cloud further up. The radiosonde data gives a high relative humidity between 5 and 6 km, and also at 8 km. High relative humidity indicates an area where cloud could persist without evaporating.

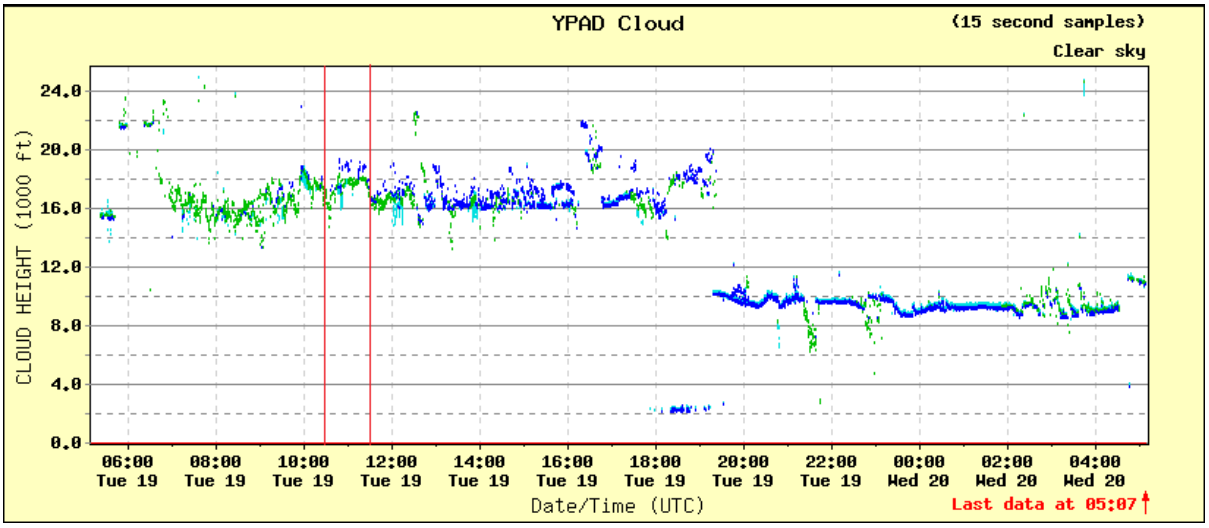

Figure 12: 24 hours of cloud base heights from the Adelaide Airport ceilometer. The lidar data corresponds with 10:30 to 11:30 UTC on this plot (between the red lines). Cloud base during this period is given as 18 kilo feet (That is 5.5 km). (Source: Bureau of Meteorology)

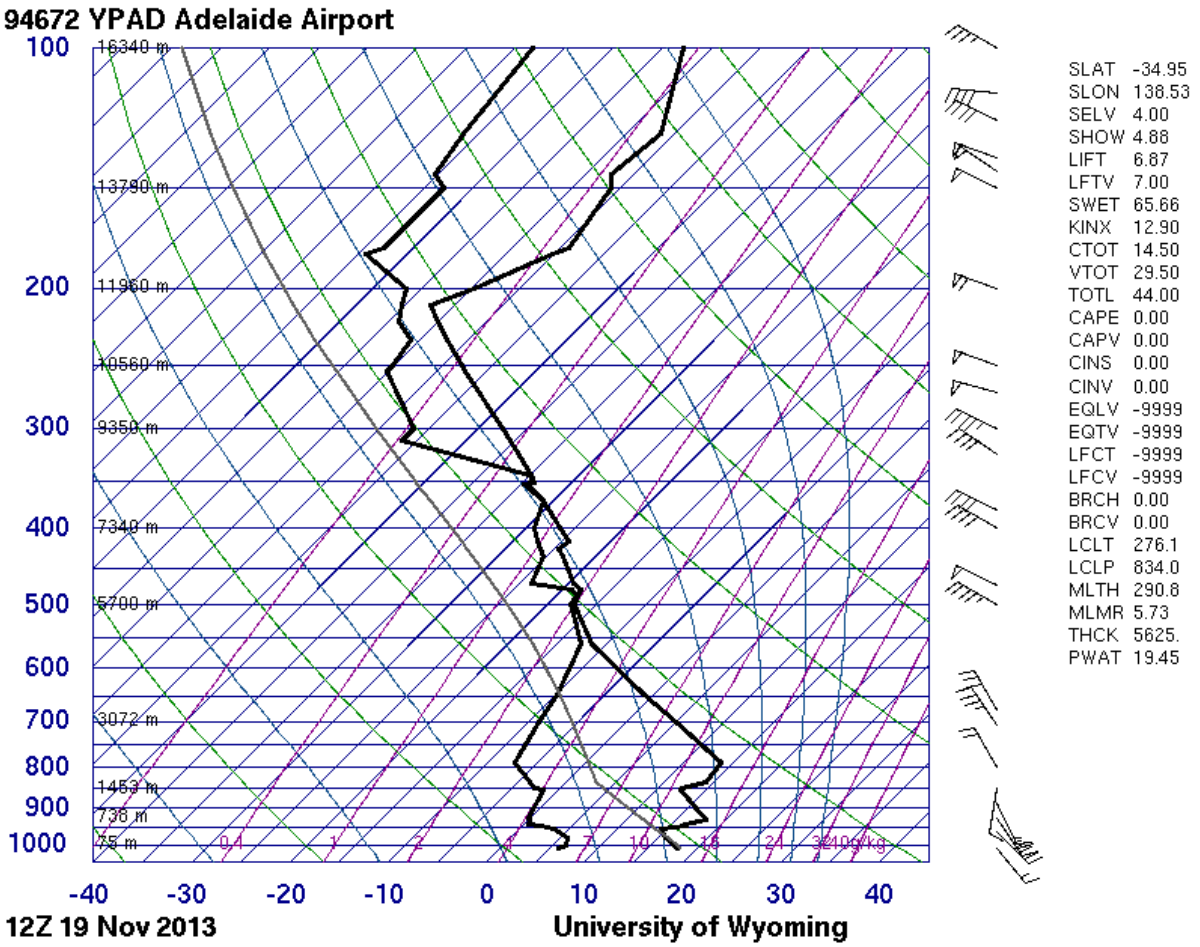

Figure 13: Radiosonde data plotted onto a skew-t chart by the University of Wyoming's radiosonde data archive. These data is from a radiosonde launched at Adelaide Airport 30 minutes after the lidar was turned off. The isotherms are the blue lines running up and right from the base, with their temperatures being the blue values on the x axis. The leftmost thick black line is the dew point temperature and the rightmost thick black line is the actual temperature (These lines may touch but never cross). The blue numbers on the left indicate the air pressure in hectopascals. The featherlike lines to the right of the chart indicate the wind direction and speed. The section between 5 and 8 km where the dew point temperature is only a little under the actual temperature means that the relative humidity is near 100% at those heights. (Source: http://weather.uwyo.edu/upperair/sounding.html)

2.3.3: Satellite Comparison

Case 1:

The first cirrus cloud detection that corresponded with a CALIPSO satellite overpass occurred on the night of the 15th of April, 2014 (Figure 14). Cloud was detected between 9 and 11 km, from midnight until dawn (technically on the 16th; however a convention of labelling each night's data with the date it starts was used). This night included a western satellite overpass (see Figure 2, Page 9), with the closest point of the pass occurring at 2:40 am (ACDT), approximately 70 km west of Adelaide. This discrepancy of measurement locations is accounted for by noting that the local winds at cirrus cloud heights tend to be around 70 km per hour and westerly (from radiosonde profiles). This means that we can expect to see whatever the satellite saw, over Adelaide 1 hour later. The CALIPSO satellite also detected cirrus clouds at heights between 9 and 11 km (Figure 15). While the returned signal was barely above the background noise, the satellite agreement shows that such low signals are reliable.

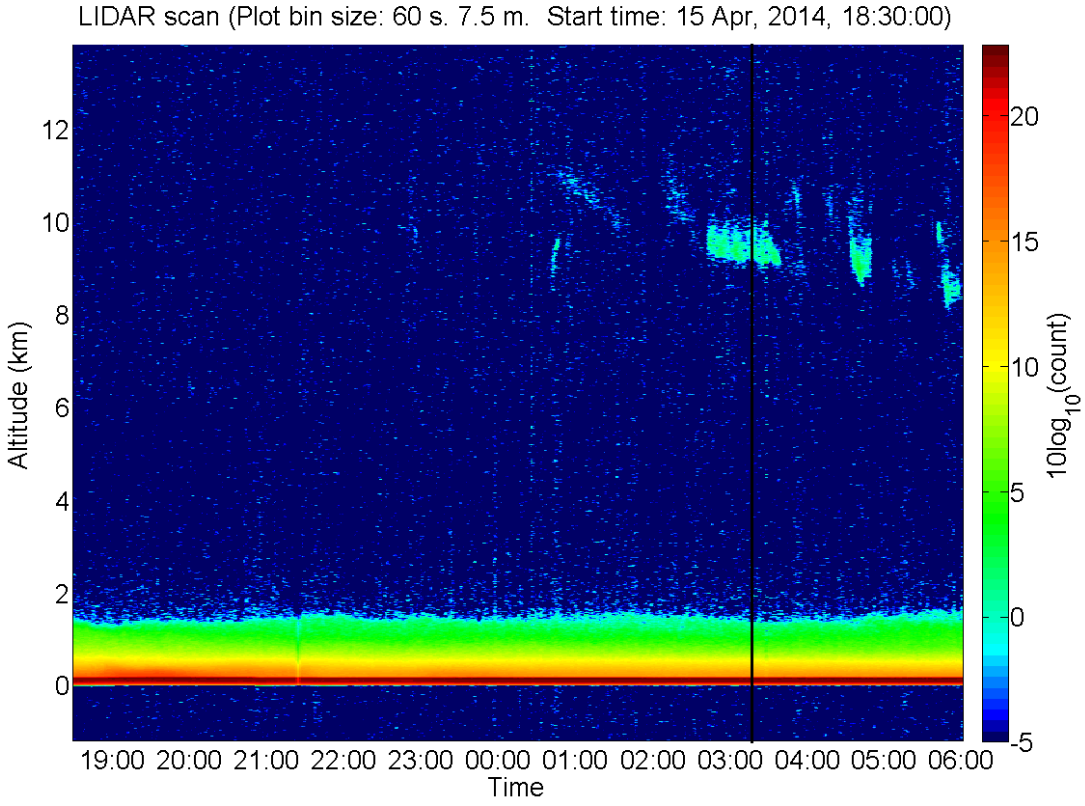

Figure 14: Lidar data for the night of the 15th of April, 2014. This plot shows a layer of Cirrus cloud around 10 to 11 km, on the edge of the detection range. The time of comparison with the CALIOP instrument is an hour after the Callipso flyover(03:40), because the satelitepasses approximately 70km to the west of the lidar location . Times are in local time, not universal time.

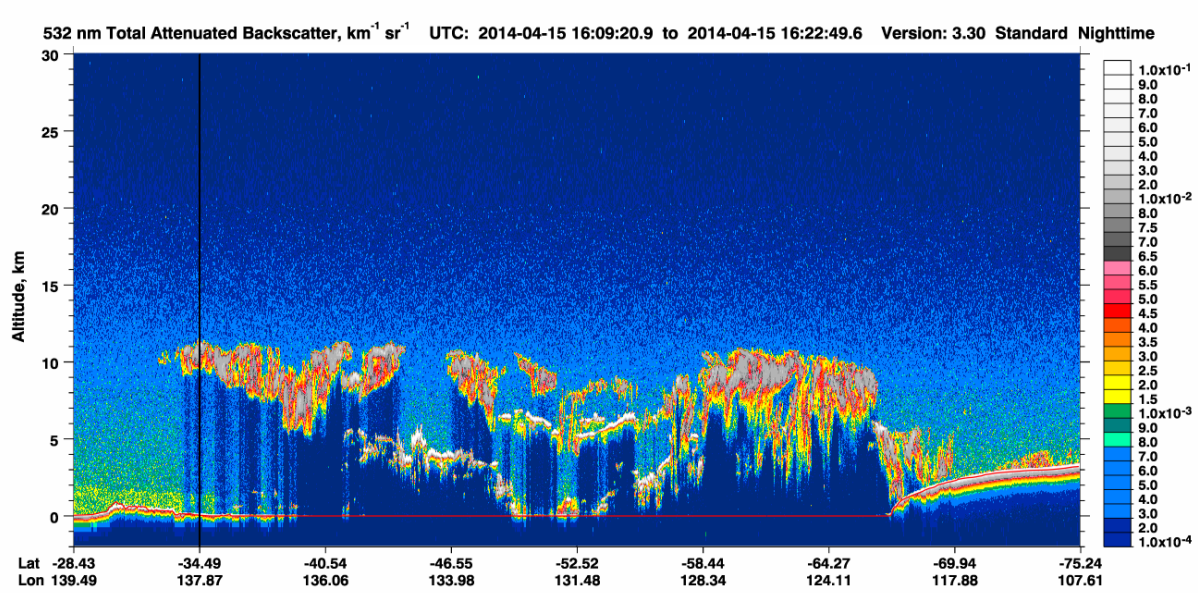

Figure 15: The satellite data corresponding to the night of the 15th of April, 2014. On the left of this plot can be seen the Australian continent, on the right can be seen the Antarctic continent. A black line marks the position of the closest point (Lat: -34.5), which has a strong return from 9 to 11 km. This image also shows another difficulty with comparing satellite measurements with ground based lidar: Thick clouds can fully attenuate the signal, seen here as the dark blue sections under the clouds, so the satellite can't always see the same clouds that the ground based lidar detects. (Source: http://www-calipso.larc.nasa.gov/)

Case 2:

As an example of lidar data that doesn't overlap with CALIOP data, the night of the 26th of May, 2014 is shown in Figure 16. The lidar detected a dense cloud layer below 1 km and cannot see anything higher. While signals at this height usually correspond to the ground level aerosols, the return strength being 300 times the usual aerosol return indicates that it is in fact due to cloud composed of liquid water. CALIOP detected a dense cloud at 5 km and cannot see anything below it, not even a clear air return (Figure 17). These incidents where one or both instruments fail to detect a cloud, because intervening clouds were too thick, comprise all of the disagreements between the instruments.

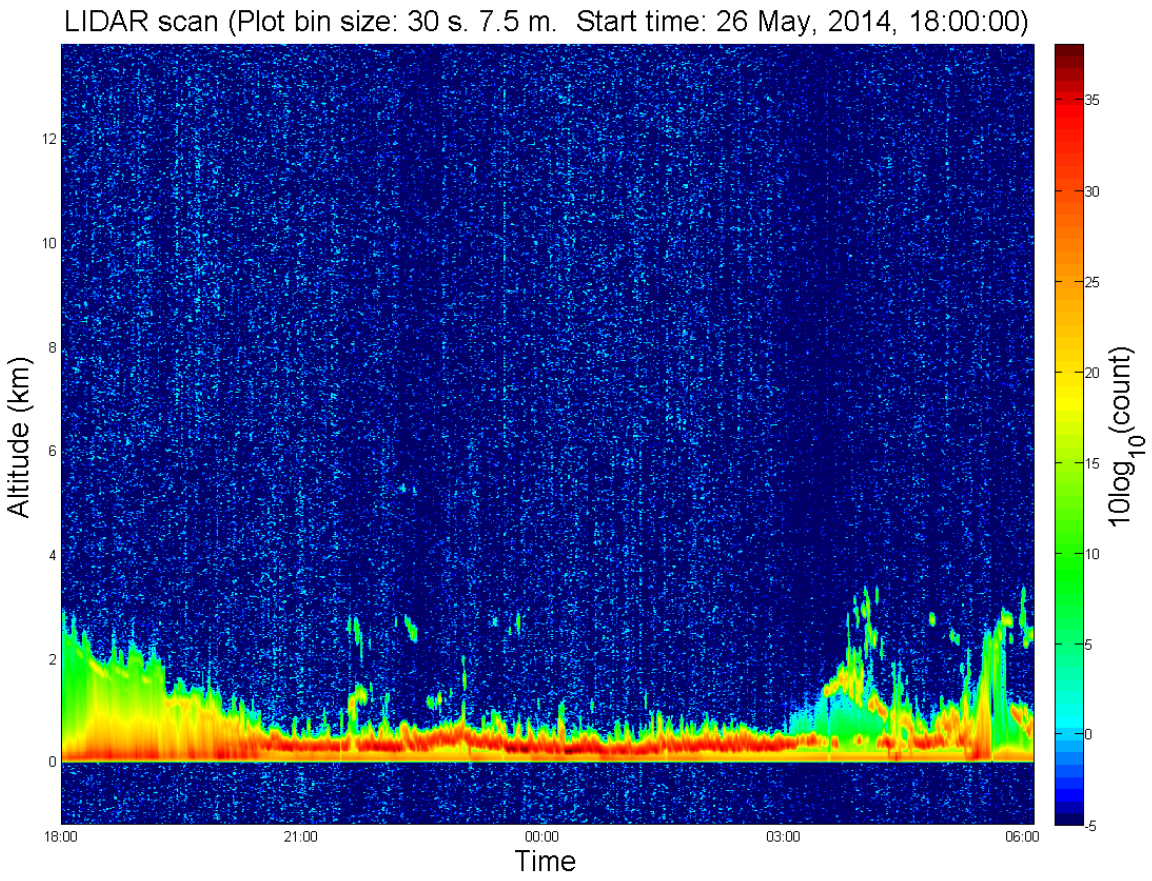

Figure 16: Lidar data from the night of the 26th of May, 2014. A very low and optically thick cloud is stopping the lidar from getting any returned signal above the cloud base for most of the night. Some precipitation streaks are visible before 9pm and around 5am. Times are in local time, not universal time.

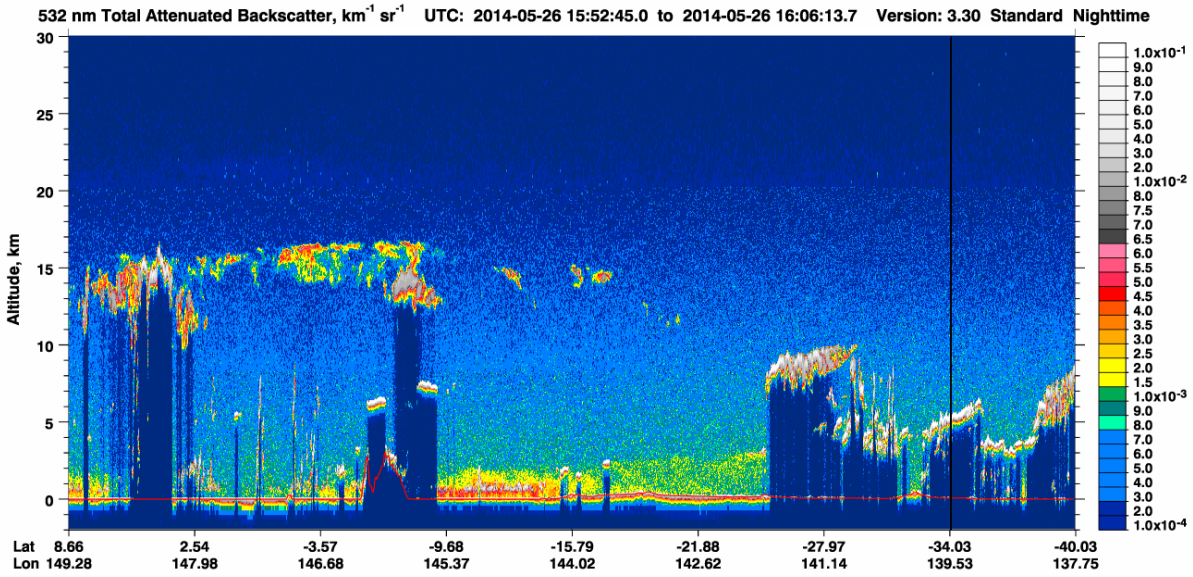

Figure 17: The satellite data for the night of the 26th of May, 2014. At the same time as the above obscurement, an optically thick cloud at 5 km (Lat: -34), is stopping the satellite from getting any returned signal from below it. (Source: http://www-calipso.larc.nasa.gov/)

2.3.4: Streaky Clouds

Case 1:

While most clouds detected are only a few hundred metres thick and have clearly defined boundaries, some clouds were represented by diffuse smudges in the plots, which could be over a kilometre thick, with weaker returned signals. A subset of these diffuse edged clouds was labelled downward streaks (see Figure 18, 2200 to 0600). While still quite diffuse, downward streak clouds showed clear internal structure, that of rapidly falling patches of increased return signal, whereas standard diffuse edged clouds showed no clear structure. This apparent downward motion of the cloud particles was independent of the position of the cloud layer as a whole. As a whole, these clouds tended to remain at the same height, though they would regularly drift by up to a kilometre in height. These clouds are similar in appearance to fall streaks, but no parent clouds are detected above them. While this could be due to insufficient signal strength to detect a higher level cloud, comparison with satellite data did not indicate any high level cloud existed above these clouds.

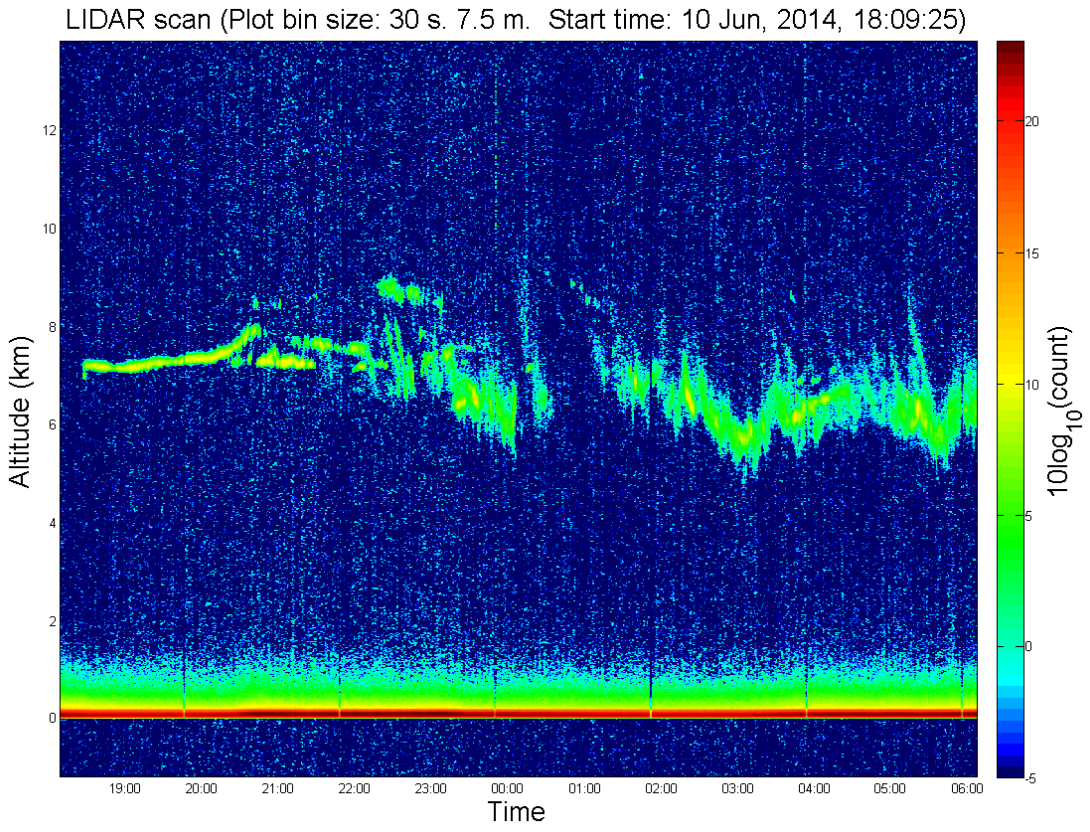

Figure 18: Lidar data for the night of the 10th of June, 2014. It shows a sharp edged cloud layer changing to a downward streak diffuse edged cloud. While the cloud base is fairly stable for the sharp edged clouds earlier in the night, the base of the streaky clouds varies by up to a km. When there is a gap in the streaky cloud, no higher cloud that could be producing these fall streak like clouds is seen. Times are in local time, not universal time.

Case 2:

Three separate nights of all night coverage of similar looking streaky clouds coincided with a CALIPSO overpass. These clouds were generally around 6 km, ranging from 4 to 8 km. The depolarisation data from the satellite indicated that two of these events were ice crystals, and the other was liquid water. Plots for the liquid water cloud are given in Figure 19 and Figure 20. Radiosonde data for the night of the liquid streaky cloud puts the freezing level at 3 km, which makes the cloud droplets supercooled with a temperature range of -15 to -5°C. Unfortunately, there has not been such a clearly measured event since the depolarisation equipment was added to the lidar. A possible explanation of the structure of these clouds is that they consist of rapidly falling particles, which are then evaporating at the cloud base. Further investigation of weather conditions during these events is needed to get a better understanding of these clouds.

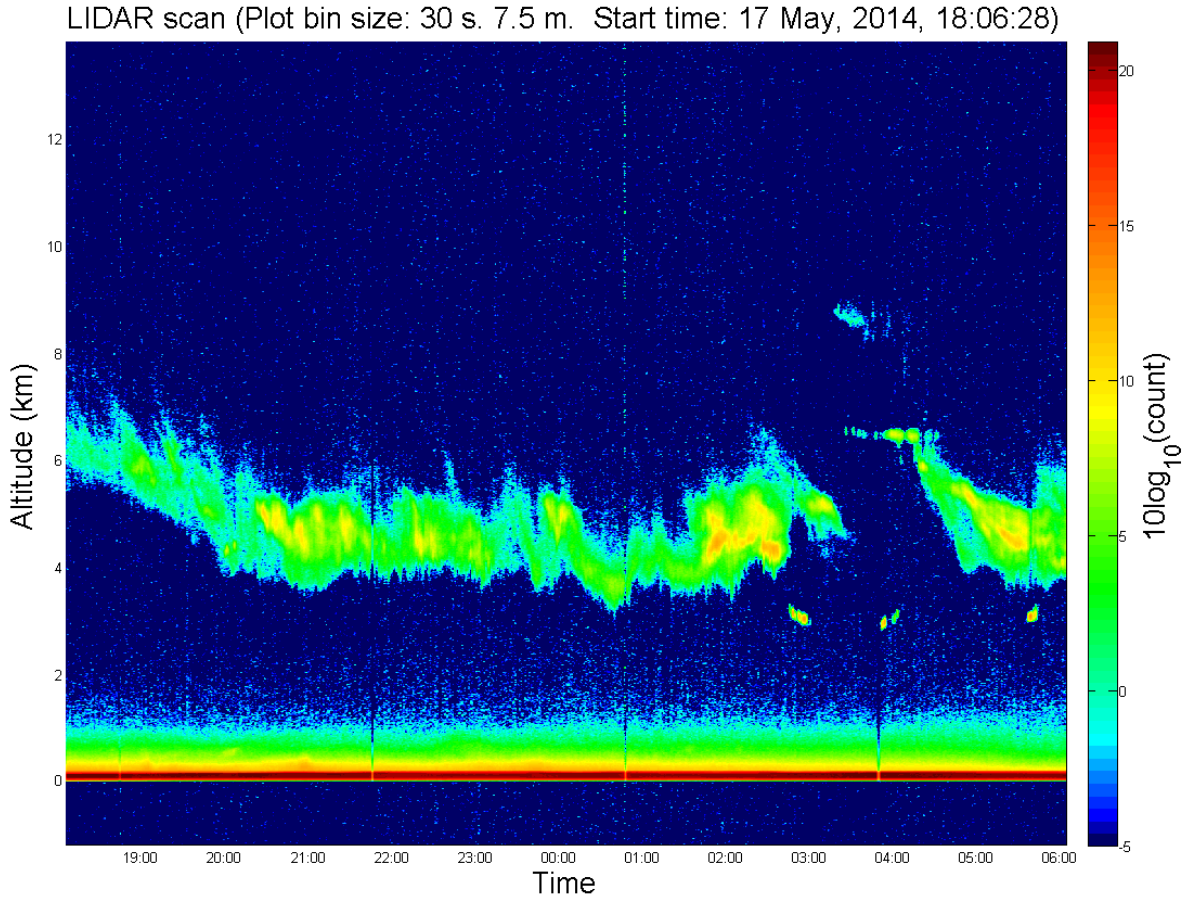

Figure 19: Lidar data from the night of the 17th of May, 2014. It shows a layer of diffuse edged cloud with a downward streaky structure. Times are in local time, not universal time.

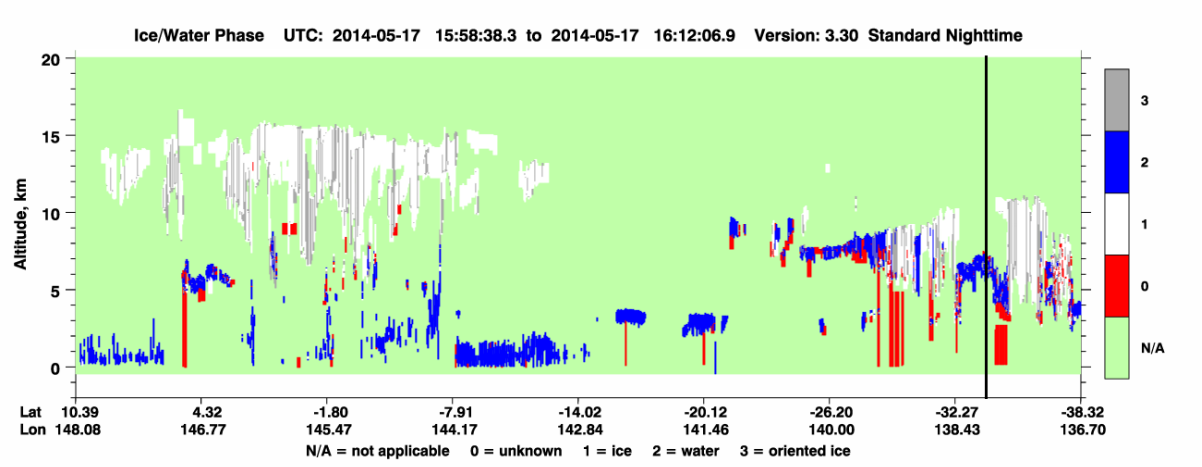

Figure 20: CALIOP thermodynamic phase estimates for the pass on the night of the 17th of May, 2014. Cloud that would pass over Adelaide was classified by CALIOP as a liquid cloud, as shown at Lat: -34. This latitude is shown as a vertical black line. Blue indicates liquid cloud, white indicates ice, grey indicates aligned ice and red indicates unknown. (Source: http://www-calipso.larc.nasa.gov/)

2.4: Optical Thickness and Inversions

2.4.1: Methods:

Optical thicknesses were derived from the lidar data using the transmission method described by Chen (2002) (flowchart in Figure 21). This requires that the clear air background signal is clearly visible above and below the cloud (though it is preferable if there isn't a big change in aerosol levels between the top and base of the cloud, as this will distort the accuracy of the values).

Optical Thickness Calculation:

To determine the optical thickness of a cloud, start with a plot of the returned count, without range squared correction. Identify the base and top of the cloud, e.g., where the signal deviations from an exponential decay start and end. Then plot two curves of $P \times r^{-2}$, where P is an initial value (Figure 22). Adjust the values of P for the two curves until one matches the returned count curve at the base of the cloud. Call this P value P_b. Match the other curve with the top of the cloud and call that P value P_t. If these curves are not fairly parallel to the return curves above and below the cloud, this is an indication of disruption due to incomplete overlap between the transmitter and receiver, variable aerosol densities, or incorrectly identified cloud edges. An effective optical thickness can then be calculated as:

$$\tau_e = -\ln\left(\sqrt{\frac{P_t}{P_b}}\right)$$

This is an effective optical thickness as multiple scattering effects have not been taken into account. Multiple scattering works to reduce the apparent extinction coefficient and hence reduces the apparent optical thickness of the cloud. To account for this we use a multiple scattering factor η (Chen *et al*., 2002):

$$\eta = \frac{\tau_e}{e^{\tau_e} - 1}$$

Where the real value of optical thickness can be recovered via:

$$\tau = \frac{\tau_e}{\eta} = e^{\tau_e} - 1$$

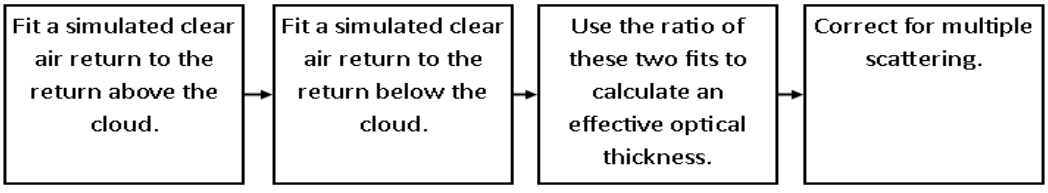

Figure 21: Flowchart of the steps used to obtain an optical thickness.

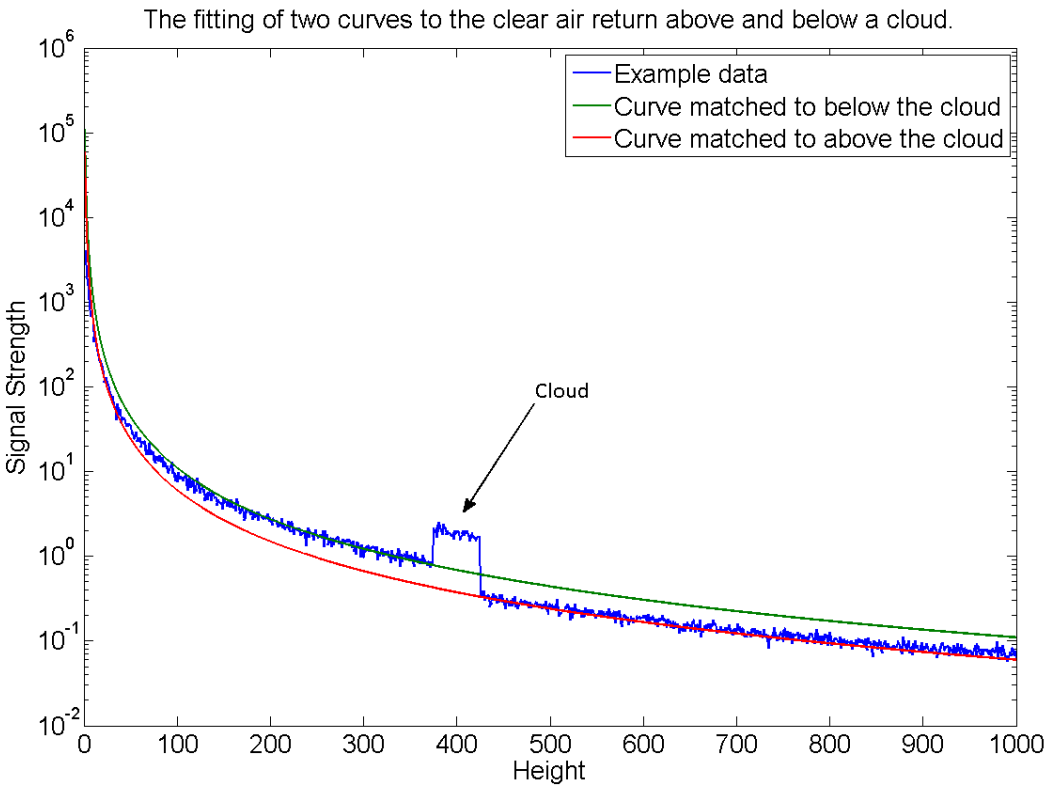

Figure 22: A plot illustrating the fitting of two curves of $P \times r^{-2}$ to the clear air signal above and below the cloud. In this example, the value of P_t is 0.6×10^5 and the value of P_b is 1.1×10^5. Therefore the effective optical thickness is 0.3.

Lidar Ratio Calculation:

To calculate the lidar ratio, the inversion method from Klett (1986) was used (flowchart in Figure 23). This calculation needs the effective optical thickness of the cloud and about 100 m of clear air background signal visible above the cloud. Select a point about 100 m above the cloud top and call it *M*. If the top of the cloud is *T*, then the clear air extinction coefficient, α_m can be estimated via (Klett, 1981):

$$\alpha_m = \frac{P(T)T^2 - P(M)M^2}{2S_M \int_T^M P(r)r^2 dr}$$

$P(r)r^2$ is the range corrected return signal at height r (r in m), S_M is the lidar ratio at M, which is clear air, so $S_M = 4\pi/3$.

To convert the returned signal versus height into an extinction coefficient versus height perform a top-down inversion of the lidar equation. To do this, start at top point M with an initial lidar ratio value S_e.

$$\alpha(r) = \frac{P(r)r^2}{\frac{S_M P(M) M^2}{\alpha_M S_e} + 2\int_r^M P(r')r'^2 dr'}$$

Then calculate an effective optical thickness via: $\tau_e = \int_B^T \alpha(r) dr$

If this value does not match with the effective optical thickness calculated via the transmission method, repeat the inversion and calculation of effective optical thickness with different guess values of S_e until it does. Again, the final value is altered by multiple scattering effects, this is corrected with:

$$S = \frac{S_e}{\eta}$$

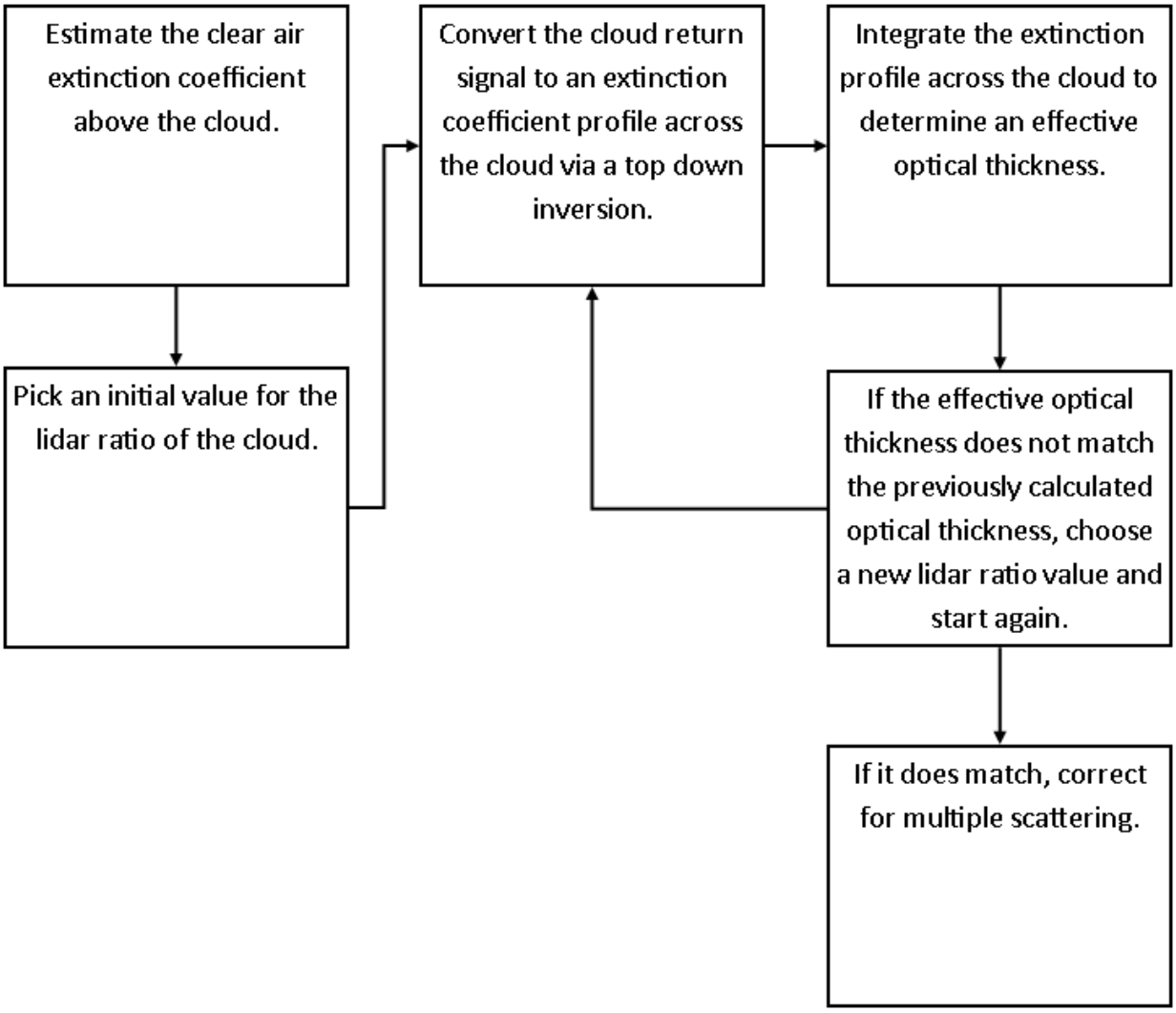

Figure 23: Flowchart of the steps used to obtain a lidar ratio.

2.4.2: Results

The transmission method was used to determine optical thicknesses for 24 clouds. This was done using clouds which ranged from heights of 300 m to 3 km. Optical thickness values ranged from 0.1 to 2.4. Of these 24 clouds, a clear air extinction value (light scattered away from the forward direction) above 14 of them was obtainable, and therefore it was possible to calculate a lidar ratio (extinction divided by backscatter coefficients) for those clouds. Clear air extinction values ranged from 0.00007 to 0.003 m^{-1}. Lidar ratios ranged from 2 to 550.

While the values obtained are reasonable, these results should be treated with some caution for two reasons: Firstly, all the clouds had bases below 2 km, meaning that the data used would contain errors due to ground level aerosols. This would cause the optical thicknesses calculated to be larger than they really are, which then increases the calculated lidar ratio. Secondly, the signal strength above each of these clouds was so weak that the data had to be summed into hourly intervals to get a clear enough signal.

2.5: Chapter Summary

In this chapter the pre-polarisation detection modifications were described. These included changes to the hardware, such as increasing the laser pulse energy and data logging range, and changes to the software such as making the control software read from both data recorders and improving the filtering in the data processing software. A comparison was made between the data from the original instrument and the data from after this upgrade. Validation measurements that were consistent with other sources were shown. Some statistics of the 3 months of data collected were also presented along with some case studies. After these upgrades the lidar was detecting clouds from heights higher than expected from the pulse energy increase. This is likely due to the improved filter. However it was noted that only the thickest of cirrus clouds were detected by the lidar and that reliable optical thickness measurements could not be made.

3: Polarisation Upgrade

This chapter describes the addition of the polarisation measurement equipment to the lidar, along with the needed software changes and additional hardware. A comparison between data from before and after the polarisation equipment was installed is made. Then the averaged nightly occurrence statistics of three months of measurements are presented, followed by some case studies of ice detections.

3.1: Methods and Instrumentation

3.1.1: Physical Components

Polarisation Equipment:

To capture polarisation information, we used a Meadowlark Variable Polarisation Rotator (LCR-300-VIS-TSC) borrowed from the Australian Antarctic Division (Figure 24). This device is composed of a twisted cell nematic liquid crystal and a polariser. Changing the voltage over the liquid crystal allows rapid switching of the retardance of the liquid crystal (with 5 ms and 10 ms transition times). The polariser was placed after the liquid crystal. This combination allows quick switching between filtering out the parallel or perpendicular polarisation components of the returned light. In terms of Stokes Parameters (see A1: Stokes Parameters, page 70), the parallel component plus the perpendicular component is *I*, while the parallel component minus the perpendicular component is *Q*. This method of polarisation filtering allows measurements to be made with only one photo detector, removing the requirement of calibrating two photo detectors. However, half of the signal to noise ratio is lost, due to the filtered light being discarded.

A Meadowlark Liquid Crystal Digital Interface is used to control the voltage on the liquid crystal. It also controls a small heater attached to the liquid crystal, which is used to improve the response time of the crystal. The Digital Interface is controlled from the computer via a serial port.

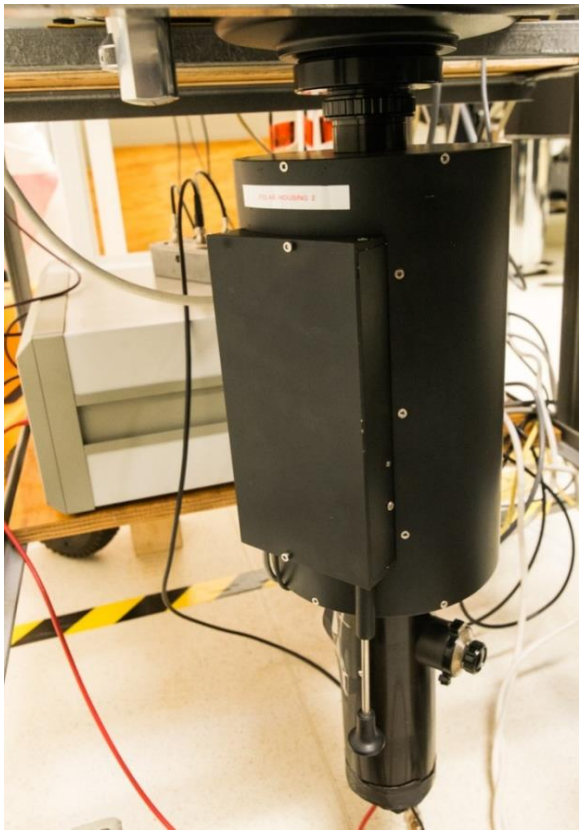

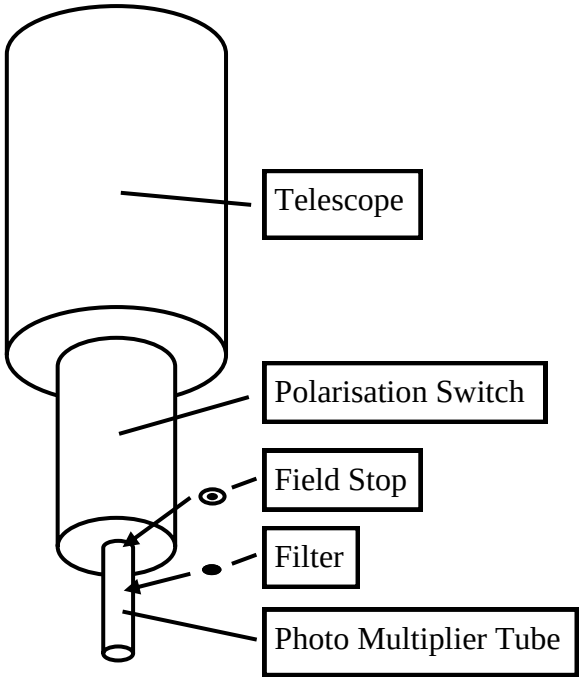

Figure 24: (above left) The polarisation switch, attached to the bottom of the telescope. The photomultiplier tube is then attached to the base of the polarisation switch. The large box in the background is the Licel data acquisition box, with a signal splitter sitting on top.

Figure 25: (above right) Diagram of the receiver system after the installation of the polarisation equipment.

Field of View reducer:

Multiply scattered photons can interfere with polarisation measurements. This is because two or more scattering events are unlikely to have parallel scattering planes. The random angle between these two scattering planes randomises the polarisation of the photon because the coordinate transform between the two scattering planes rotates the polarisation. So it is desirable to receive as many of the single scattered photons and as few of the multiply scattered photons as practical. Every detected photon must have had its final scattering event at a point inside the field of view of the receiver. Every single scattered photon must have had its final scattering event inside the divergence of the laser beam. Therefore, any detected photon that had its final scattering event outside the divergence of the laser beam must be a multiply scattered photon. So reducing the field of view of the receiver to the divergence angle of the laser beam, will remove many multiply scattered photons without any reduction in the amount of single scattered photons being detected. Reducing the receiver field of view

also decreases the amount of atmospheric background noise detected, because the receiver then samples a smaller volume of sky.

The field of view of the receiver was reduced by inserting a field stop between the filter and the telescope (Figure 25). The field stop is a small aluminium disc with a hole in the centre, shaped to fit neatly above the filter. The 4.8 mm diameter of the hole reduces the effective diameter of the photomultiplier from 8 mm to 4.8 mm. This reduces the field of view of the receiver from 2.3 to 1.35 mrad. Theoretically, such a reduction would reduce the amount of sky seen by the receiver by two thirds, thus reducing the atmospheric background noise by two thirds. However, there was only a 25% reduction in background noise. This suggests a significant amount of the noise is instrumental.

One downside to reducing the receiver field of view is that complete overlap between the laser pulses and the receiver field of view now starts at a higher altitude, that of around a kilometre instead of a few hundred metres. This reduces the returned signals below 1 km, resulting in decreased sensitivity to ground level aerosol haze and the clear air signal being undetectable, as seen in Figure 37, page 50.

3.1.2: Software Alterations

Lidar Control Program:

Once the polarisation equipment was installed, another revision of the program was written to add all the new functions needed for polarimetric measurements. These functions include driving the digital interface of the liquid crystal, recording the polarisation state in the saved data, and displaying the polarisation data in real time. The lidar control program opens communication via a serial port to the digital interface during the initialisation sequence of each run, just after the Licel commands have been sent. (Communication to the driver via USB connection is also possible; however I couldn’t get it to respond correctly to commands sent that way.) The program then sets the temperature target point for the heater and enables the Transient Nematic Effect (TNE) voltage overshoot. Both of these settings work to improve the liquid crystal’s response time. The voltage is then set to allow the parallel component through. The voltage setting is changed between each shot (4096 pulses) and a polarisation flag is saved into the saved data. The voltage switching is done when the Licel recorder says it has summed the returns from 4096 pulses, but before the data is read from the

Licel box, to give the liquid crystal the maximum amount of time to switch before the counting restarts.

A new drop down menu called “View” was added to the program (Figure 26). The options in View allow switching the display between the total return counts, the parallel return counts, the perpendicular return counts and the depolarisation ratio values determined from these counts. All plots are updated regardless of whichever view is currently set and can still be switched after the run has finished.

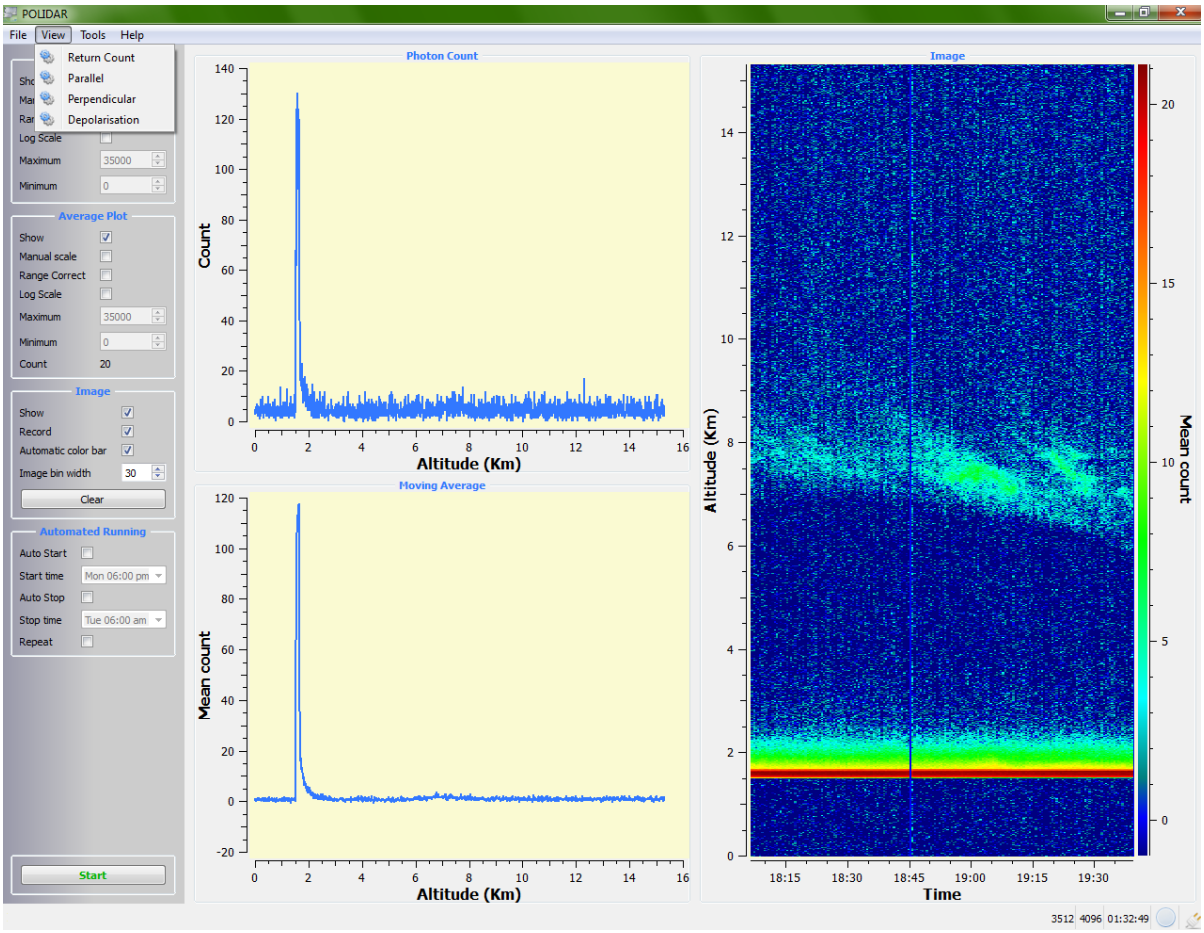

Figure 26: A screenshot of the polarised lidar control program showing the new 'View' menu.

Matlab script

A revised version of the post processing script was made to handle the polarisation data (see Figure 7, page 18 for a flowchart explaining the script steps). The first alteration is the binning of raw counts into three different data sets: total, polarisation parallel to emitted laser and polarisation perpendicular to emitted laser. After these data have been processed and smoothed, a depolarisation ratio data set is generated by dividing the perpendicular data

set by the parallel data set. These values are then constrained to between 0 and 5, and a mask is used to blank out any values generated from signals that are too weak to give a reliable value of the depolarisation ratio. Four plots are then generated, with the colour scales of the parallel and perpendicular plots set to be identical to the total count plot, to assist with comparisons. The depolarisation plot is set to between values of 0 and 1. Additional code was added later to automatically save the plots.

3.2: Polarisation Results

3.2.1: Comparison

Data from before (Figure 27) and after (Figure 28) the installation of the polarisation equipment was compared to assess the loss of range. Both show a layer of cloud slowly descending from 8 to 6 km, over the course of the night. While Figure 27 shows a reasonable signal up to 8 km height, Figure 28 is barely showing the cloud above 6 km. While it is possible that the cloud in the before image is much thicker than the cloud in the after image, many similar clouds had been detected at that height with similar signal strength, before the depolarisation equipment was added, and afterwards nothing stronger than the after plot signal was detected. Taking a measurement of the cloud without the polarisation equipment and then reconstructing it to take an 'after polarisation equipment installation' measurement is impractical.

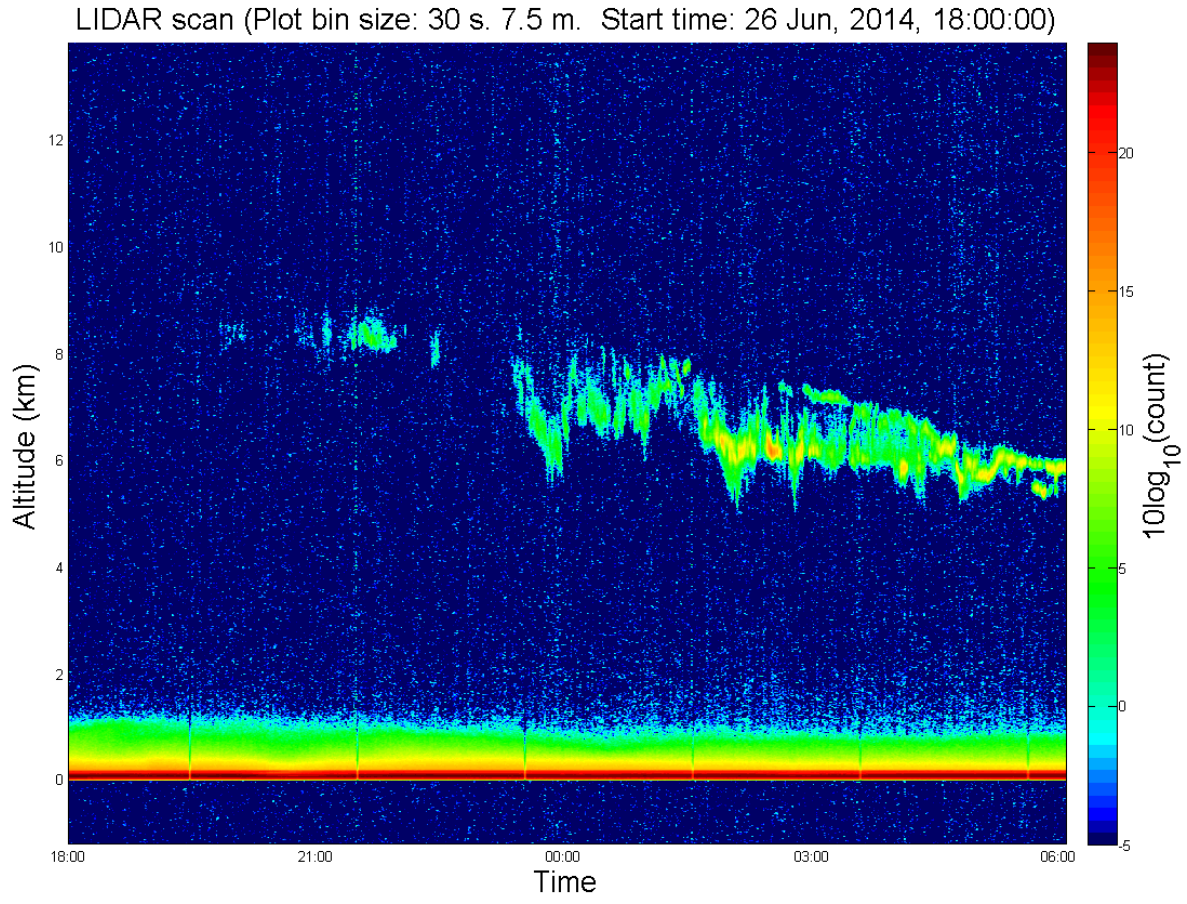

Figure 27: Lidar data from the night of the 26th of June, 2014. It shows a slowly descending cloud layer at 6 to 8 km; detected before installation of the polarisation discriminating equipment. Times are in local time, not universal time.

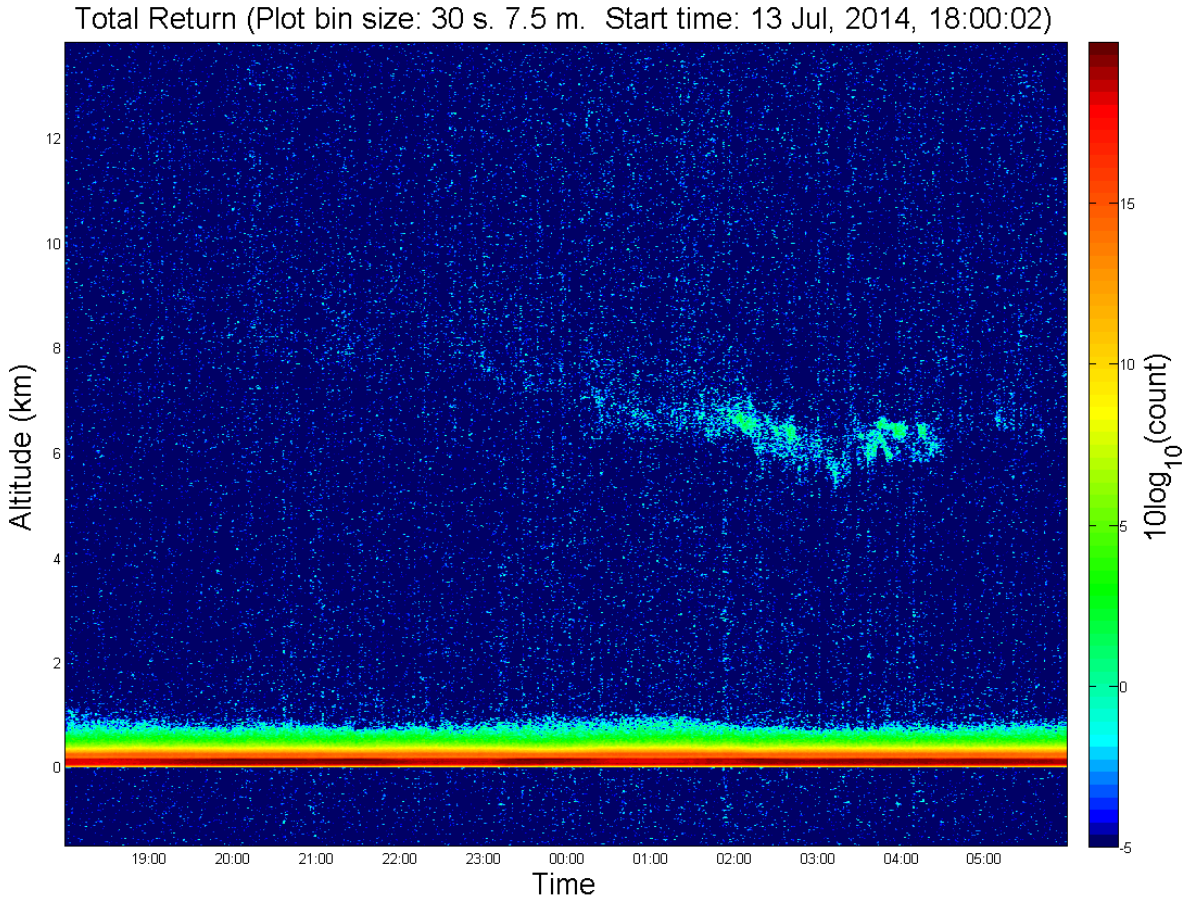

Figure 28: Lidar data for the night of the 13th of July, 2014. It shows a slowly descending cloud layer at 6 to 8 km; detected after installation of the polarisation discriminating equipment. This time the return signal is barely above background and the clear air return is diminished. Times are in local time, not universal time.

3.2.2: Cloud Height Frequencies

As before (page 21), each night was divided into 1 km height and 3 hour time bins and the clouds were counted (Figure 29). After the polarisation equipment was added, the low cloud peak from before remained at 1-2 km, but the high cloud peak was lost. While it is possible that this could have been caused by seasonal variation reducing the amount of high cloud or increasing the thickness of lower clouds, the most likely cause is that the reduced signal strength has reduced the upper limit on cloud detection heights. The highest occurrence fraction for the low cloud peak was for July, of around 50% of the nights at 1 km, while the lowest peak occurrence fraction was for September of 35% of the nights at 2 km.

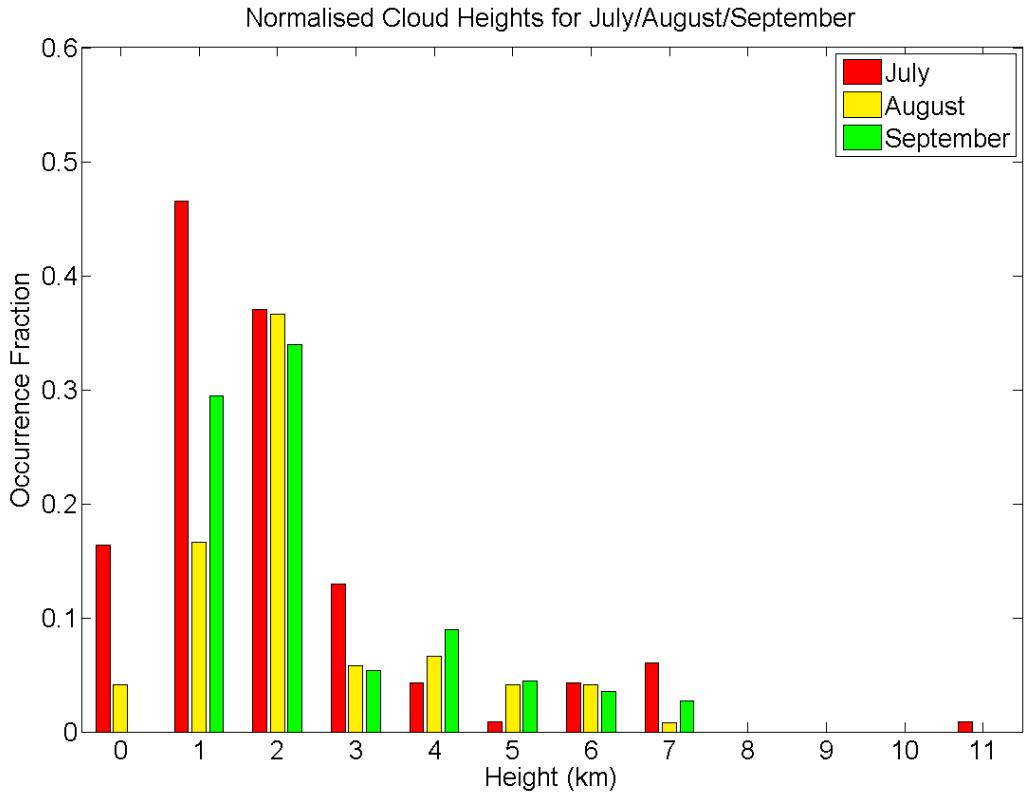

Figure 29: Normalised cloud occurrence fractions at different heights for the months of July, August and September. The analysis used in Figure 10 was applied for the months after the polarisation equipment was added. The loss of range has removed the high peak from around 8 km, while the low peak is still around 1-2 km.

3.2.3: Depolarisation Ratio Statistics

The three months of depolarisation ratio data were divided into the same 1 km and 3 hourly bins as for the frequency statistics. The depolarisation ratio values were split into 4 bins; 0-0.1 which is likely to be horizontally oriented crystals (or very thick aerosol clouds), 0.2-0.3 which is likely liquid phase, 0.4-0.5 which could be ice, multiple scattering off liquid or a combination of liquid and ice, and 0.6-0.8 which is likely ice only. These ranges were chosen based on the work by Hu (2007) and by grouping values based on how they were interpreted. While the depolarisation ratio is usually used in conjunction with the signal ratio for determining thermodynamic phase, the lidar receive no clear air signal near the clouds of interest, which makes all signal ratios infinite and unusable. However a qualitative comparison of signal ratio between two clouds is used when possible. The results for the three months were summed, as the events with depolarisation values outside of the 0.2-0.3 range were sparse (Figure 30). Unfortunately, even summing the three months of data still doesn't show anything interesting for the depolarisation ratios associated with ice. The 0.2-0.3 range however does show a peak at 2 km, the same as the low cloud frequency peaks for each month, which agrees with the hypothesis that the sharp edged clouds are generally composed of liquid phase water (see 2.2.2 Statistics:, page 21).

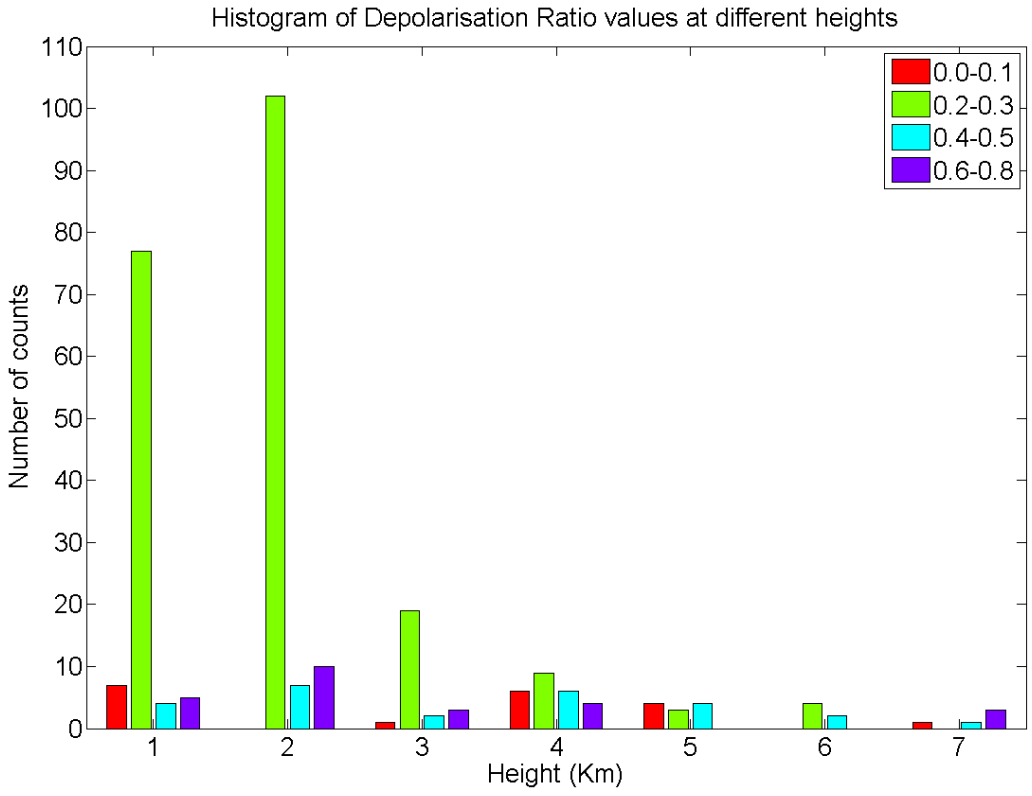

Figure 30: A histogram showing the frequency of different depolarisation ratio ranges for July, August and September. The ratio values were grouped into four groups that have similar interpretations.

Supercooled water clouds were detected in a few nights per month, such as on the night of the 11th of July, 2014 (Figure 31). To be classified as supercooled liquid, a cloud needed to be at least 500 m above the freezing level due to the uncertainty in the height of the freezing level caused by the once per day temperature sampling time. It must also have a depolarisation ratio value of around 0.2-0.3 and not show any signs of being a mixture of very low and high depolarisation ratio values (as the poor vertical resolution would average the two into the liquid depolarisation ratio range). The freezing level and cloud temperatures were approximated using once per day radiosonde data, which was sometimes at 9:30 am the next morning, other times at 9:30 pm that night.

The supercooled liquid water clouds that were detected tended to occur between heights of 2 and 4 km, up to 5 km in September. The temperatures estimated for these clouds were generally around -5°C. The depolarisation ratio values of around 0.5 seen in the precipitation streaks are thought to be caused by the large rain drops becoming too big to retain a near spherical shape, the distorted shape of these drops causes them to produce higher depolarisations than expected for liquid. For Figure 31 the freezing level is around 2 km.

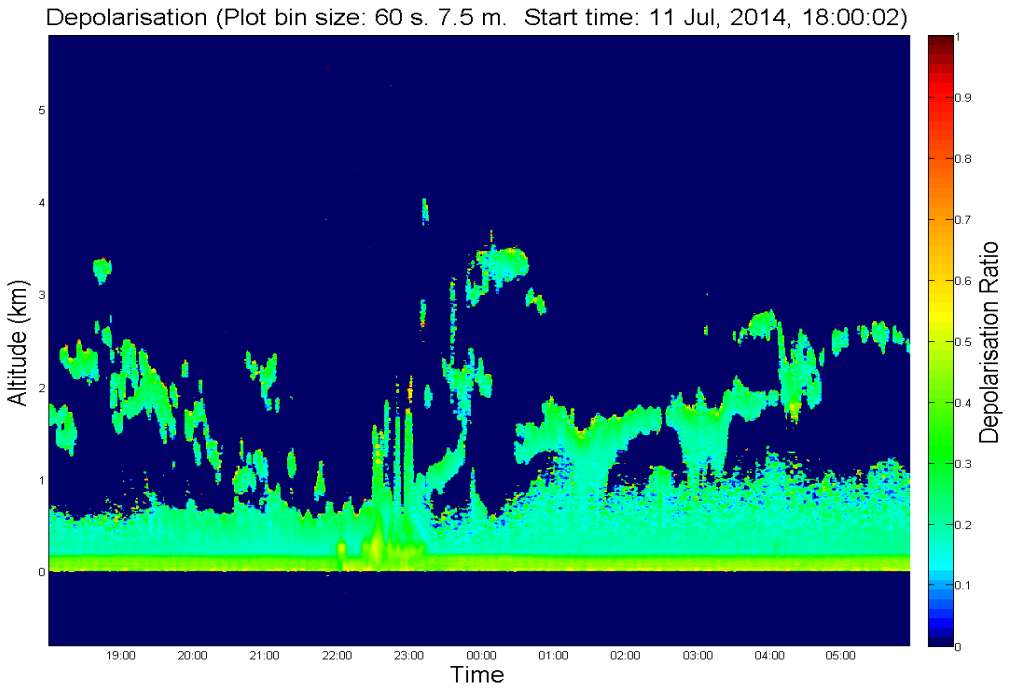

Figure 31: Lidar depolarisation ratio data for the night of the 11th of July, 2014. It shows clouds from 1 to 4 km, most with a depolarisation ratio of 0.2 indicating liquid; however the freezing level is around 2 km. Any depolarisation ratio value resulting from returns that are less than 1 count above background had their depolarisation ratio values set to 0, to avoid clutter. A few small patches of yellow around 2 km indicate the presence of ice crystals. The yellow/green streaks rising from ground level at 22:00 to 23:00 are caused by precipitation reaching the ground. Times are in local time, not universal time.

3.3: Polarisation Case Studies

3.3.1: Ice Detection

Case 1:

The first clear polarimetric measurement that included ice clouds was on the night of the 14th of July, 2014 (Figure 32 and Figure 33). This night featured a cloud layer descending from 4 to 1 km, with precipitation starting after 1 am. Extending a few hundred metres below the main cloud is a diffuse cloud which shows depolarisation ratios up to 0.8. This is likely due to ice crystals precipitating out of the cloud and then evaporating as they fall. Radiosonde data gives the freezing level as being at 2 km in the morning of the 14th and at 1.5 km in the morning of the 15th. There was no CALIPSO overpass that night.

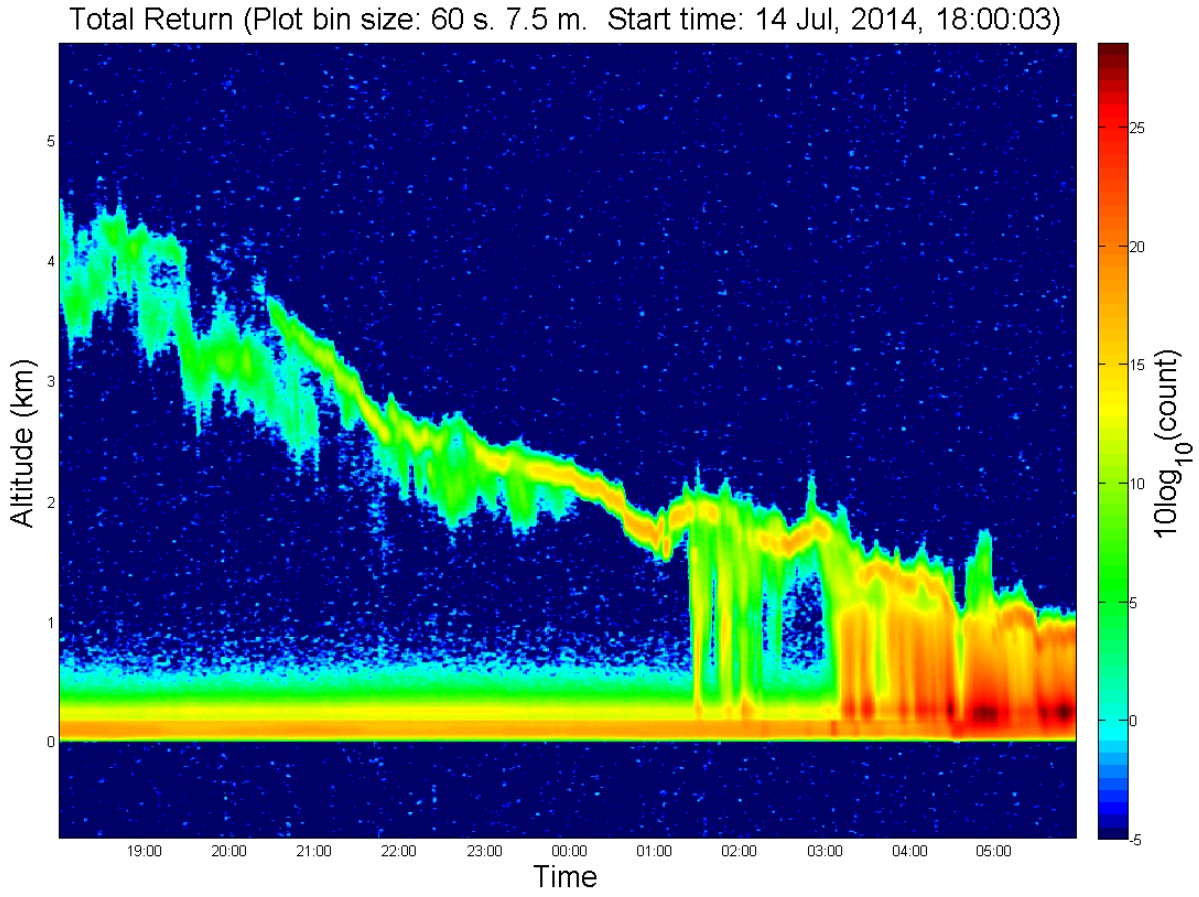

Figure 32: Lidar return strength data for the night of the 14th of July, 2014. It shows a descending cloud layer with diffuse patches underneath it, becoming precipitation early morning. Times are in local time, not universal time.

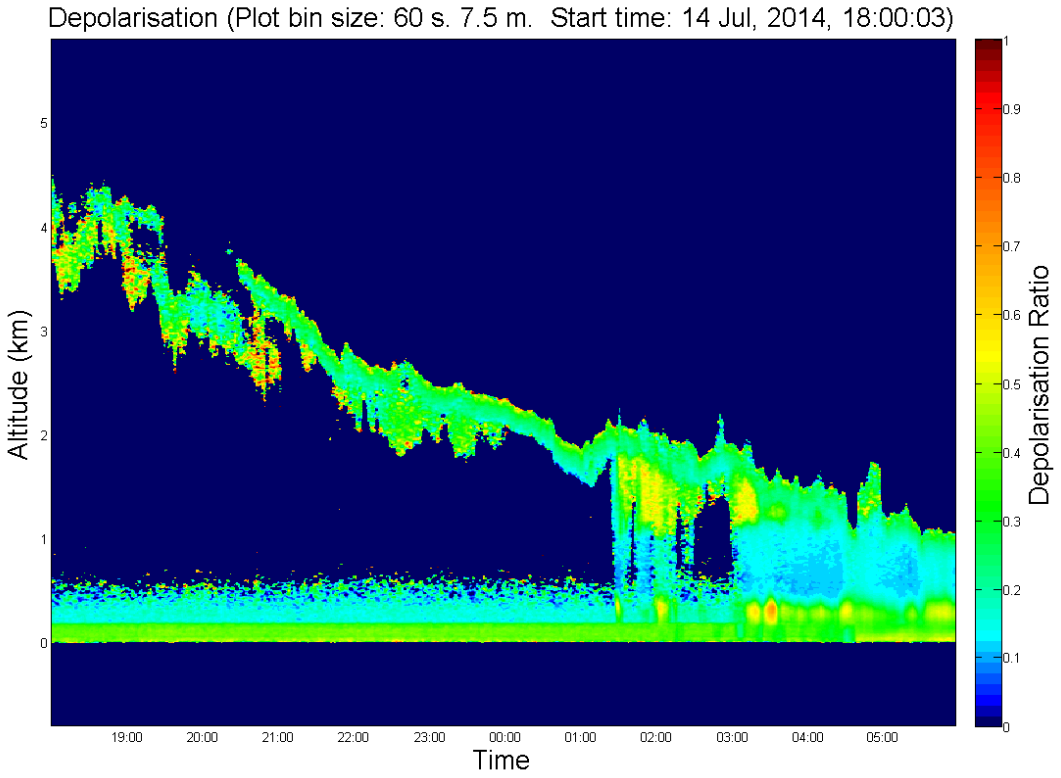

Figure 33: Lidar depolarisation ratio data for the night of the 14th of July, 2014. It shows that the diffuse clouds below the upper cloud are composed of ice crystals that have precipitated out of the cloud and are evaporating shortly later. Interestingly, the freezing level of around 2 km means that the liquid cloud layer is super cooled in the early evening, at around -10°C. This temperature is good for producing hexagonal plate crystals, which would explain why there is a patch around 8pm that appears to have a stronger return signal, but lowered depolarisation ratio. Times are in local time, not universal time.

Case 2:

Another polarimetric detection of ice clouds occurred on the night of the 31st of July, 2014 (Figure 34 and Figure 35). Clouds were detected between 1 and 5 km, though the gusty winds, varied cloud heights and frequent precipitation made it impossible to discern any particular cloud structure or layers. Some patches of cloud had the usual 0.2 depolarisation ratio indicating liquid, while many also contained patches of 0.6 depolarisation ratio indicating ice. This night did not contain a satellite overpass which could have been used to verify the ice detection. However, radiosonde data (Figure 36) puts the freezing point at around 800 m, and sleet fell on Mt Lofty (700 m above sea level, around 10 km away), which is consistent with the lidar data. Some high depolarisation ratio values were detected near ground level as well. However, it is unclear if these are caused by hail or multiple scattering from dense rain.

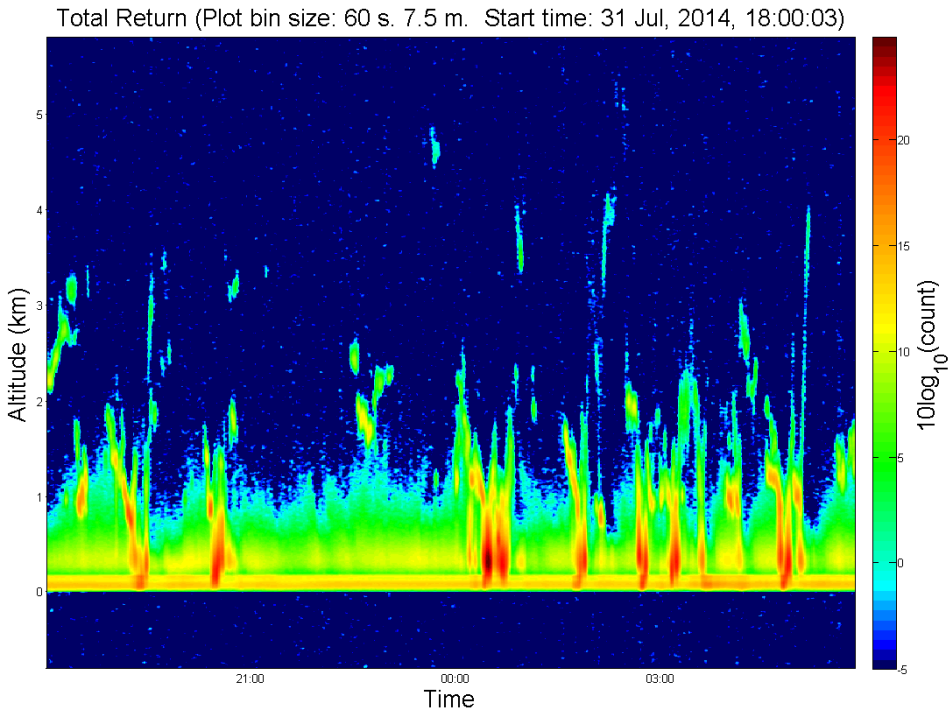

Figure 34: Lidar return strength data for the night of the 31st of July, 2014. The stormy weather made it impossible to distinguish any cloud layer this night. It shows scattered rain and clouds up to 5 km. Times are in local time, not universal time.

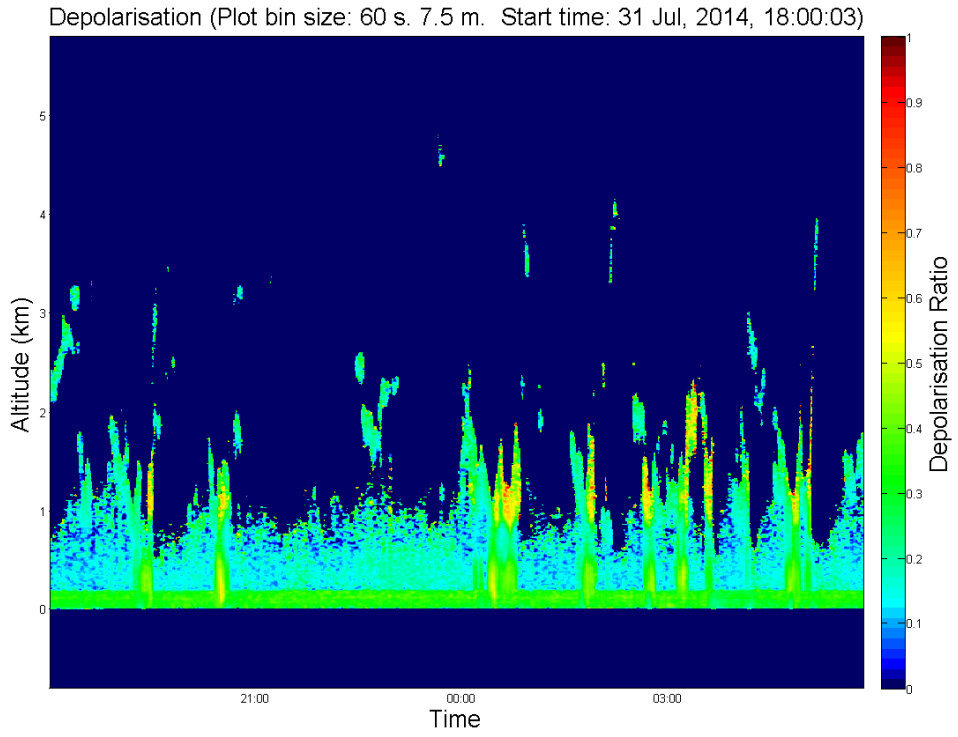

Figure 35: Lidar depolarisation ratio data for the night of the 31st of July, 2014. It shows scattered patches of ice crystals in the clouds. The high depolarisations of the precipitation near the ground could be caused by hail or flattened rain drops. Times are in local time, not universal time.

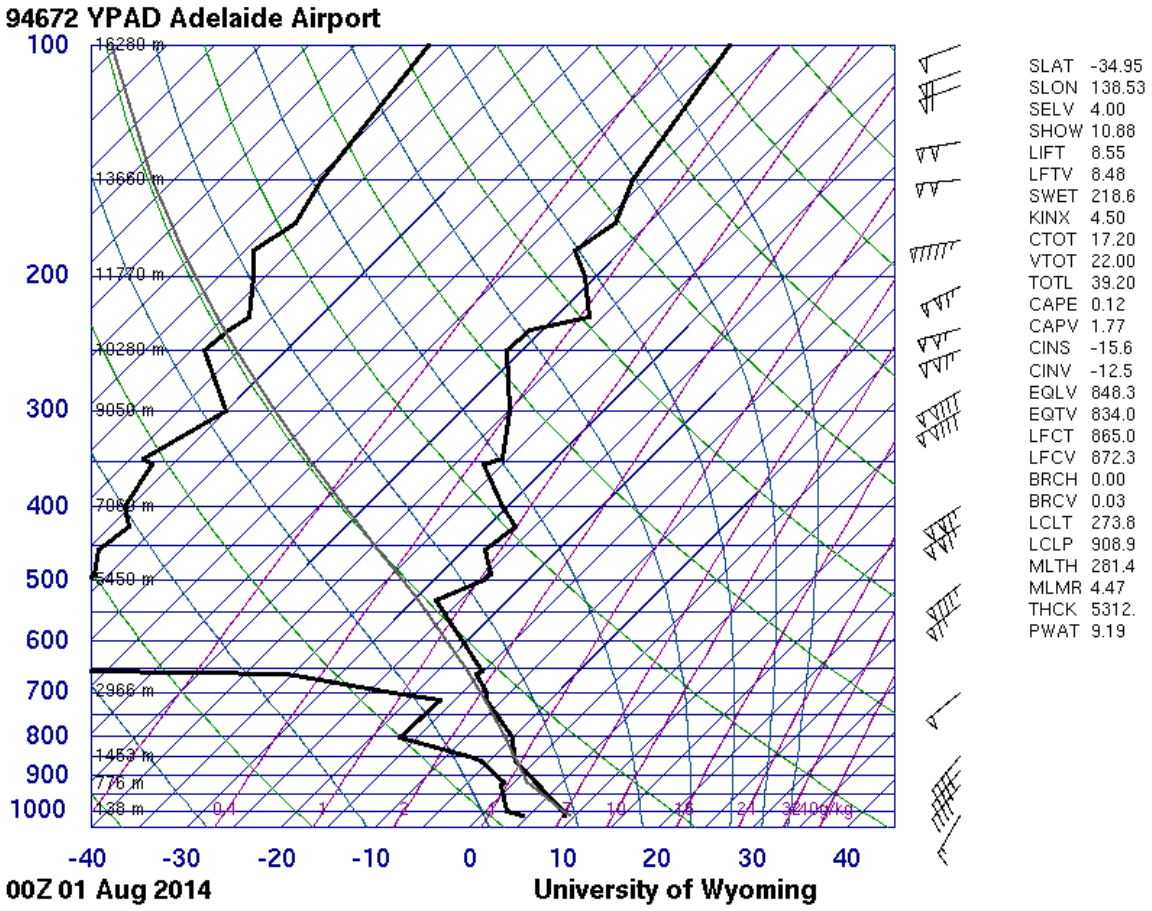

Figure 36: A radiosonde profile from the morning of the 1st of August, 2014, showing the freezing level at around 800 m. This means that it is possible for ice to be in clouds where high depolarisation was detected and also that the water clouds were super cooled. (Source: http://weather.uwyo.edu/upperair/sounding.html)

Case 3:

A third event during less stormy conditions was the night of the 8th of September, 2014 (Figure 37 and Figure 38). It starts with clouds at 3 to 4 km, some showing a depolarisation ratio indicating ice. Below these are fall streaks with varied depolarisation ratio values, showing ice at the top, but not lower down. As the freezing level is at 2.5 km (Figure 39) it seems likely that the ice melted as it fell, which is why it stops returning a high depolarisation value at lower levels. Later in the evening, the precipitation increases and obscures the clouds as they descend to around 1 km. The precipitation returns a strong depolarisation ratio near ground level again. One of the precipitation spikes has a very high depolarisation ratio of 0.7 instead of the usual 0.5-0.6, so it might have been caused by hail instead of just by multiple scattering or droplets too big to remain spherical.

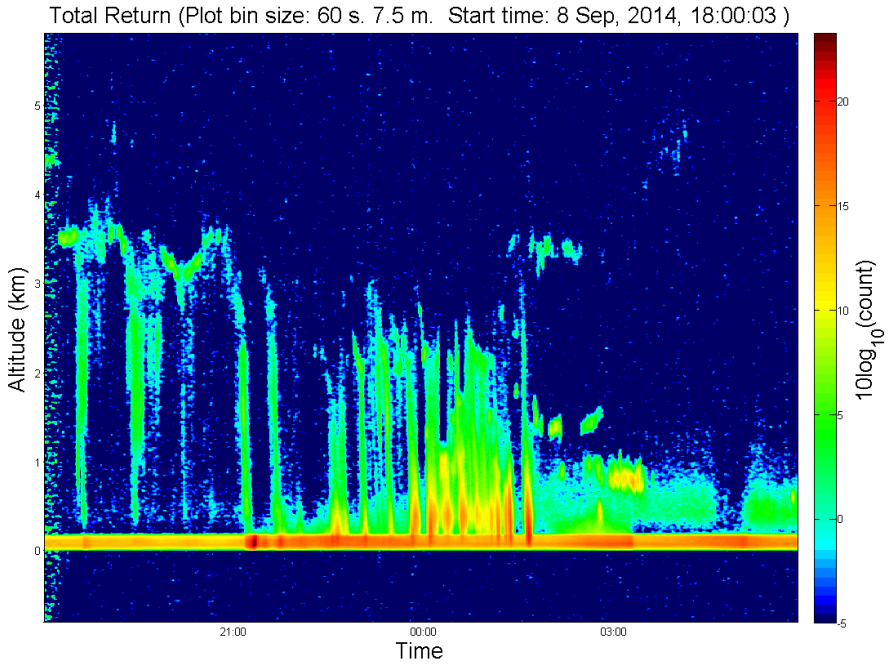

Figure 37: Lidar return strength data for the night of the 8th of September, 2014. It shows scattered cloud descending from 4 km to 1 km, and producing much precipitation (4.6mm in 24hrs, BOM Kent Town) between 9pm and 2am. A thick haze appears after the rain has passed, likely brought in by a frontal system. Times are in local time, not universal time.

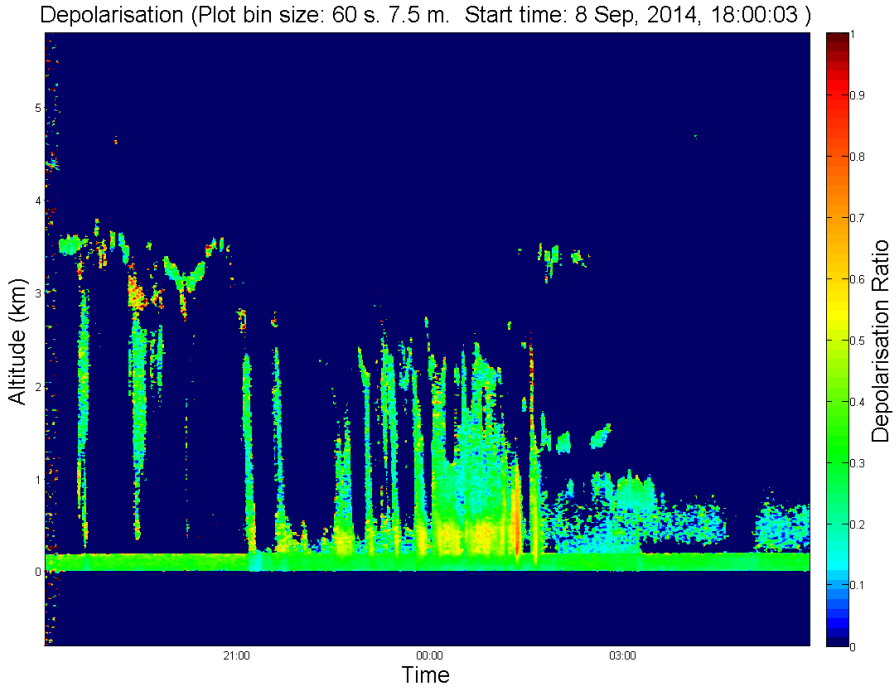

Figure 38: Lidar depolarisation data from the night of the 8th of September, 2014. It shows some ice in the clouds around 3 km. The values of 0.5-0.6 near the ground in the precipitation streaks are likely caused by multiple scattering or flattened rain drops. One particularly strong depolarisation value around 01:30 might be caused by hail. Times are in local time, not universal time.

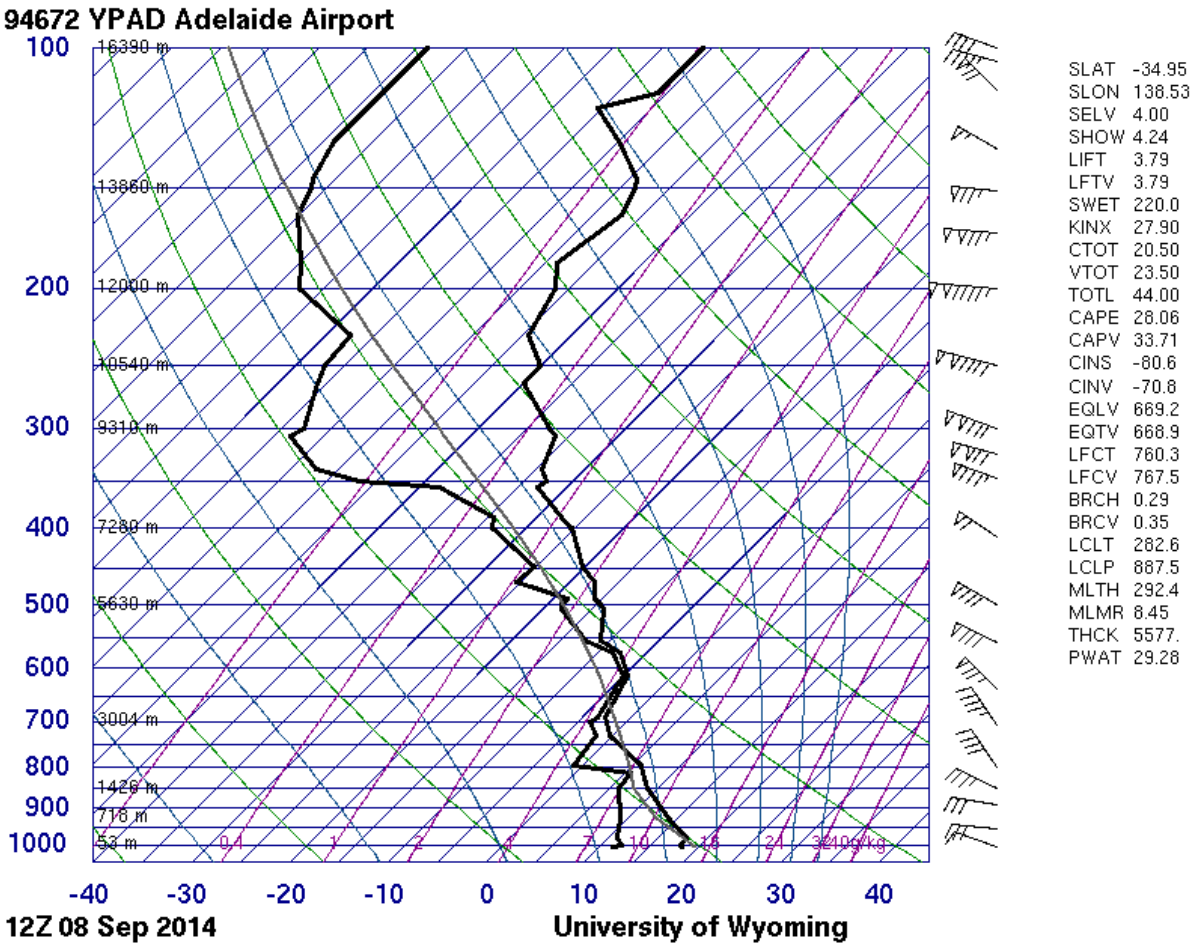

Figure 39: Radiosonde data from the evening of the 8th of September, 2014, puts the freezing level as just below 3 km. Cloud likely from 2 to 5 km. (Source: http://weather.uwyo.edu/upperair/sounding.html)

3.3.2: Horizontally Oriented Plates

In addition to the characteristic returns from liquid clouds and ice clouds, there is a third signature that is detected by lidar instruments, that of horizontally oriented crystals. Studies validating the CALIOP system detected occurrences of strong signal return and low depolarisation ratio values, which indicated liquid water, from temperatures where liquid water has not been previously detected (Hu, 2007). These values had higher return strength and lower depolarisation than water clouds. These anomalous values were determined to be caused by plate crystals that had become aligned horizontally. It was determined that horizontal alignment of crystal plates caused them to have a strong specular reflection, leading to the high return signal strengths and low depolarisation ratios measured (Hu, 2007). Due to these anomalies the CALIOP instrument had its viewing angle changed from 0.3° to 3° off nadir, halting horizontally aligned crystals from returning strong signals and low depolarisation ratios (Sassen, 2009).

Case 1:

A likely instance of horizontally oriented plates was detected on the night of the 8th of August, 2014 (Figure 40 and Figure 41). A faint diffuse layer was detected between 5 and 6 km. While the lidar could have easily resolved this before the depolarisation equipment was added, the loss of signal strength greatly reduced its range. A couple of patches were detected in this layer that had significantly higher signal strength. These patches gave a low depolarisation ratio reading of 0.1. Such low values usually indicate liquid, and is possible as the temperature at that height ranged from -10 to -20 °C (Figure 42). However, a brilliant sun dog was sighted before dusk that day, which can only occur in the presence of horizontally oriented ice crystals. As the lidar points near zenith, such horizontally aligned crystals would give a strong return signal and low depolarisation ratio. So a reasonable proposal is that those patches were horizontally oriented ice crystals.

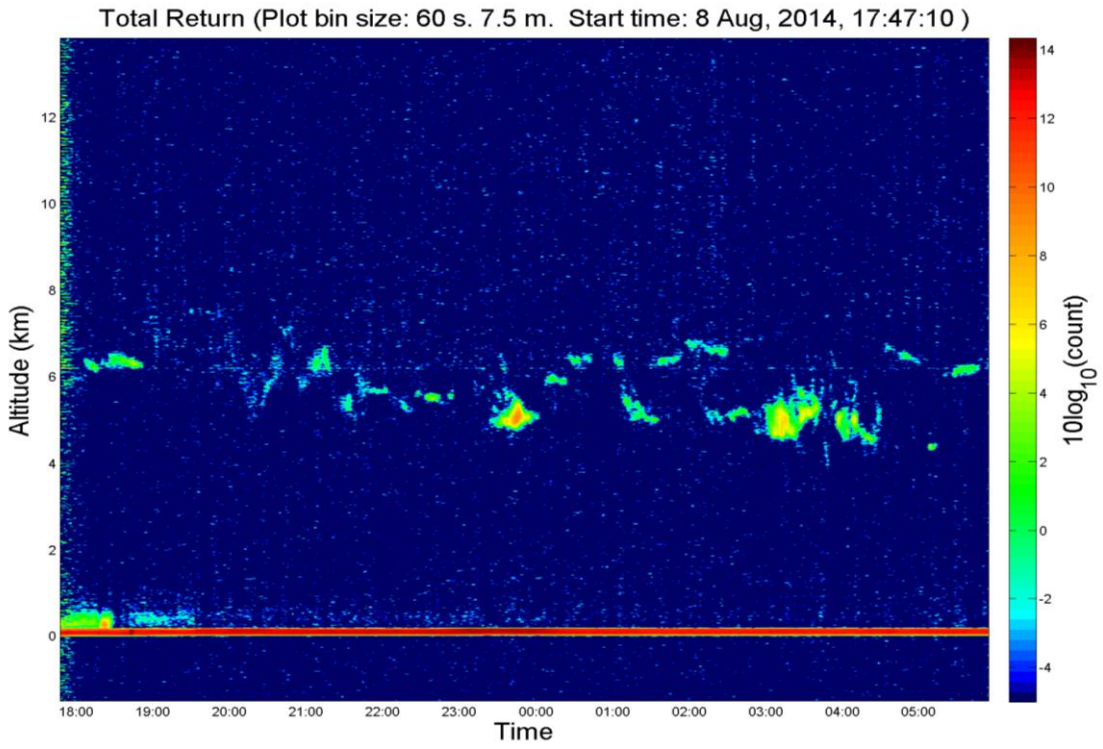

Figure 40: Lidar return strength data from the night of the 8th of August, 2014. It shows a cloud layer on the edge of the detection range containing some cloud with much stronger signal return. Times are in local time, not universal time.

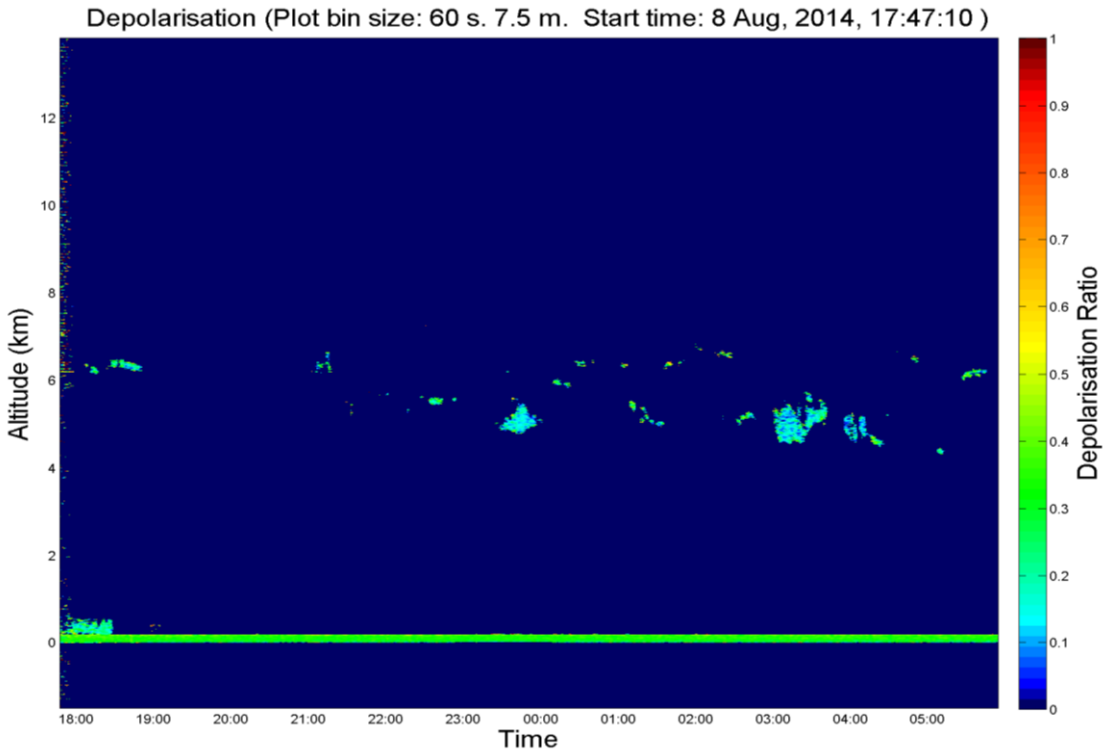

Figure 41: Lidar depolarisation ratio data from the night of the 8th of August, 2014. It shows that the patches with strong signal returns have a very low depolarisation ratio of 0.1, lower than detected from liquid clouds. Times are in local time, not universal time.

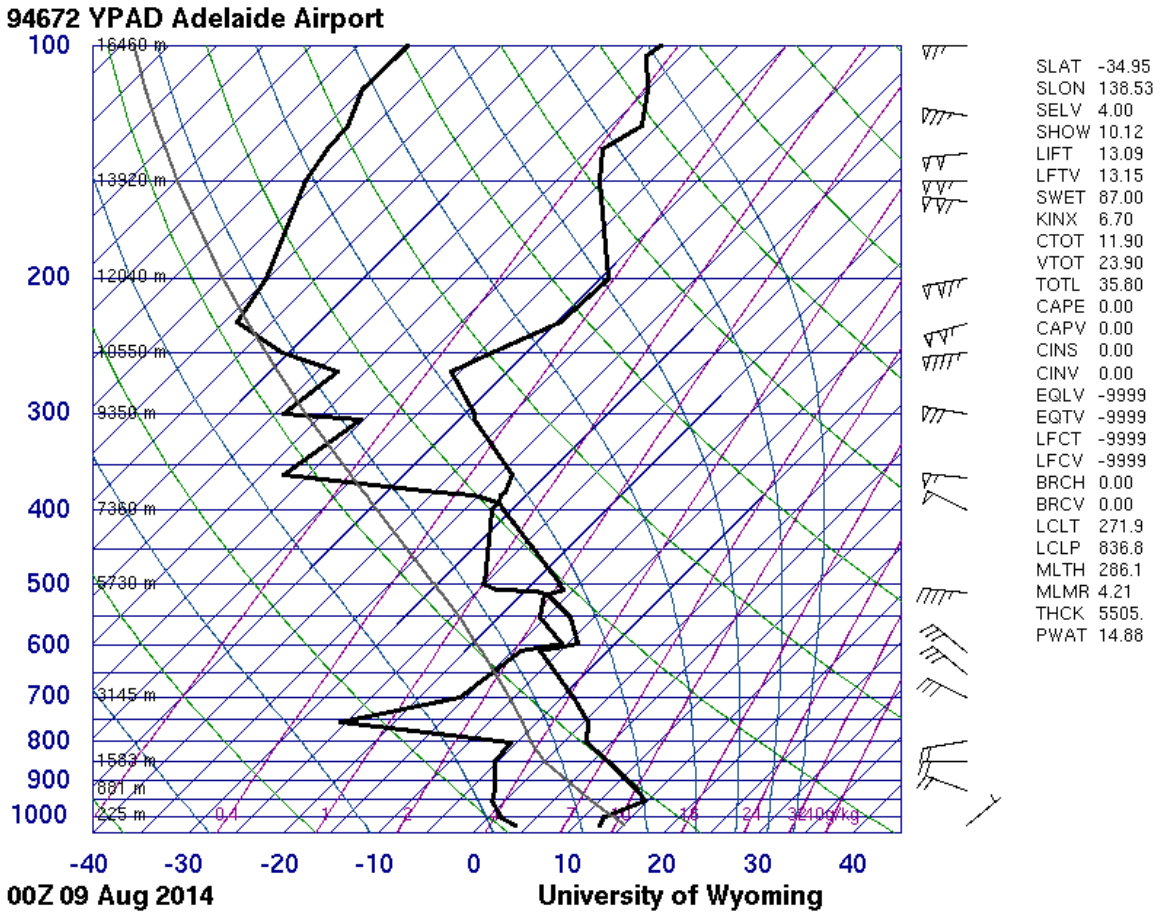

Figure 42: Radiosonde data from the following morning (9th of September) gives the temperature of the 5 to 6 km layer as between -10 and -20 °C. Which means it is possible for ice to exist in the cloud at the time, but we cannot completely discount liquid. (Source: http://weather.uwyo.edu/upperair/sounding.html)

Case 2:

One week later, on the night of the 15th of August, 2014 (Figure 43 and Figure 44), there was a partial layer of liquid water cloud at 2.5 km and what appears to be a gradually subsiding layer of ice cloud moving from 4 to 2 km. The clouds around 4 km had depolarisation ratios ranging from less than 0.1 up to 0.2. While the diffuse edged cloud around 2 km had depolarisation values ranging from 0.1 to 0.8. The freezing level for this night was around 1.5 km (Figure 45), so melting is not likely to have occurred inside this ice cloud. Instead, the lower depolarisation ratio values were likely caused by varying amounts of horizontal orientation by hexagonal plate crystals.

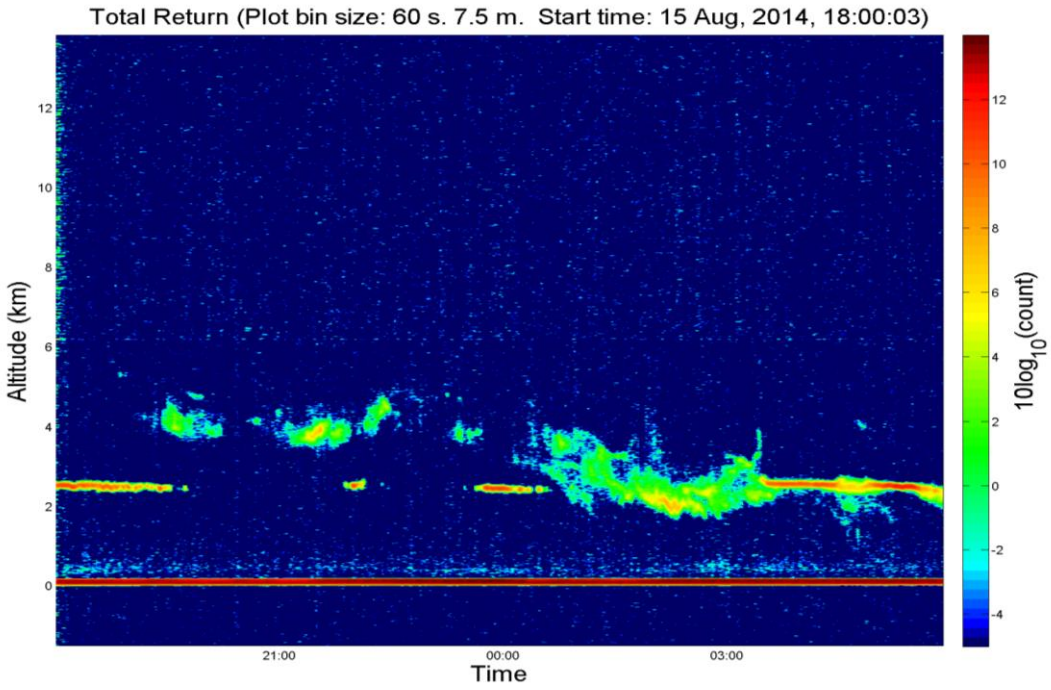

Figure 43: Lidar return strength data for the night of the 15th of August, 2014. It shows a partial layer of sharp edged cloud at 2.5 km and a descending layer of diffuse edged clouds from 4 to 2 km. Parts of the diffuse edged cloud have patches of strong return signal. Times are in local time, not universal time.

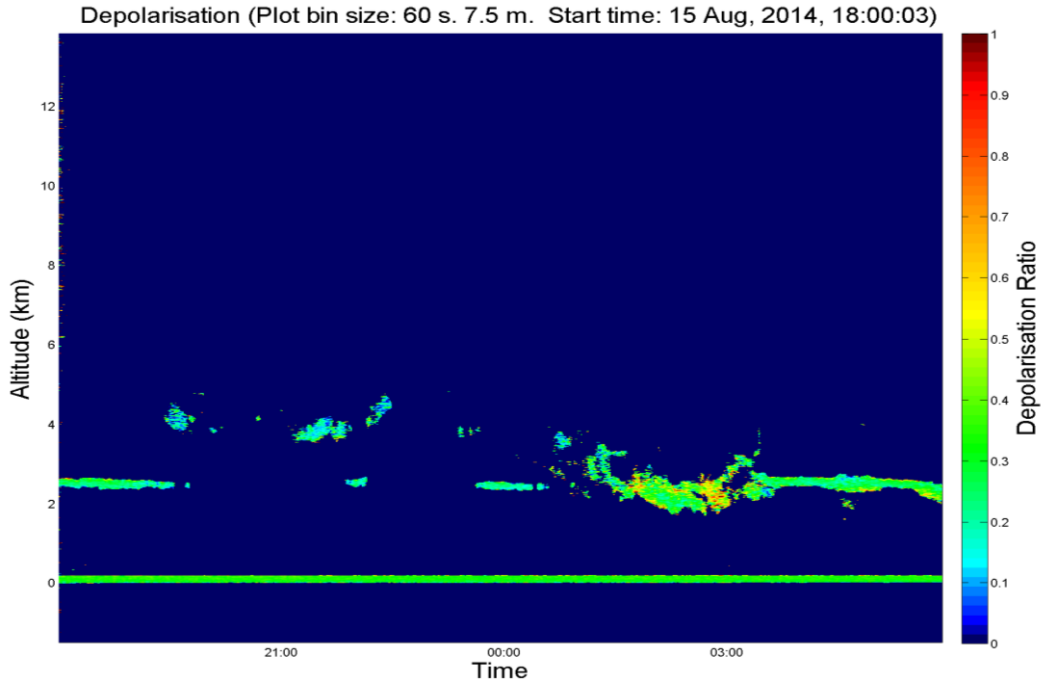

Figure 44: Lidar depolarisation ratio data for the night of the 15th of August, 2014. While the sharp edged clouds show depolarisation ratio values consistent with liquid composition, the diffuse edged clouds contain a wide range of depolarisation ratio values. The depolarisation ratios of around 0.1 at around 4 km are indicative of horizontally aligned hexagonal plate crystals. The wide range of depolarisation ratio values when the cloud goes below 3 km is likely caused by patches of crystals losing their alignment. Times are in local time, not universal time.

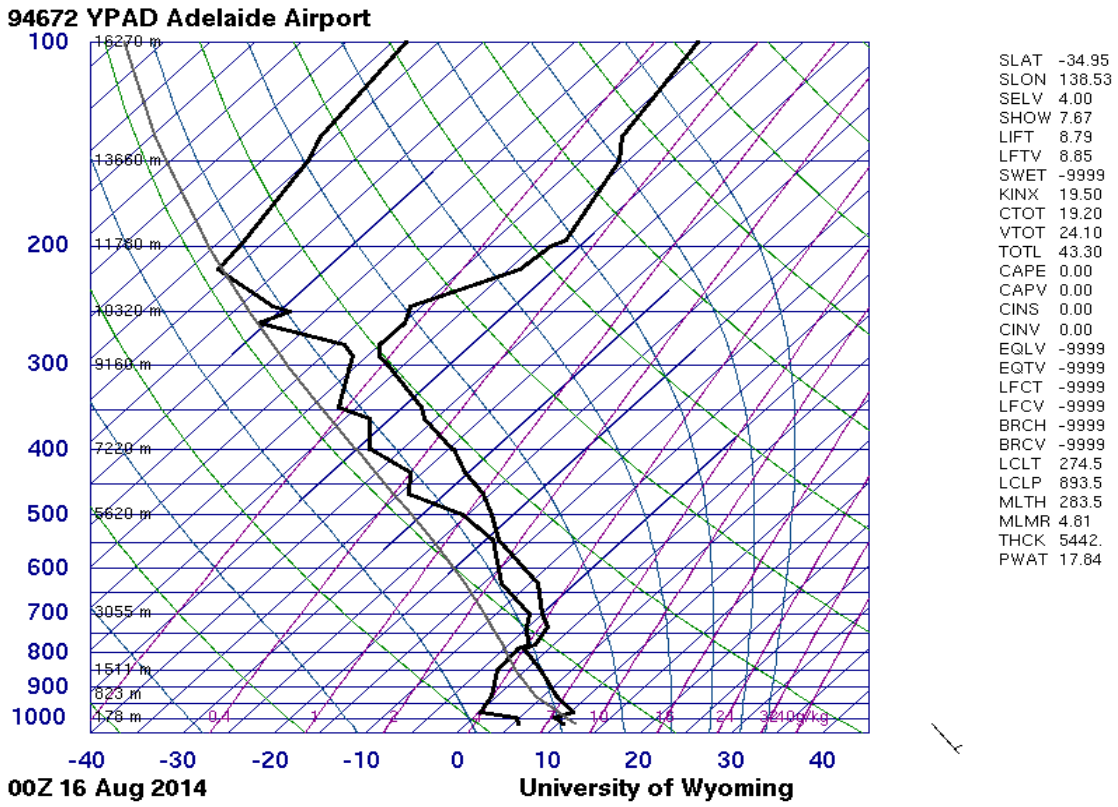

Figure 45: The radiosonde data for the next morning gives the freezing point at 1.5 km. (Source: http://weather.uwyo.edu/upperair/sounding.html)

Case 3:

Another possible detection of horizontally oriented ice crystals happened on the night of the 26th of September, 2014 (Figure 46 and Figure 47). Again, these clouds occurred at heights of 5 km, but this time other patches of cloud gave enough signal for a depolarisation ratio to be measured. In addition to the two patches of cloud with a depolarisation ratio of 0.1, there were some that had depolarisation ratios of 0.3 and one streak with a depolarisation ratio of 0.6 at 4 km. This suggests that the cloud at 5 km with 0.1 depolarisation ratio was actually an ice cloud consisting of horizontally oriented plates. Assuming the same crystal shape comprised all the clouds, then the 0.3 depolarisation ratio patches were partially horizontally oriented and the 0.6 depolarisation ratio streak was randomly oriented. Again, this did not match up with a CALIPSO satellite overpass for verification. However, a radiosonde (Figure 48) launched that evening says that cloud is likely between 4 and 5 km, and that the temperature was between -10 and -20°C. Horizontally oriented plate crystals have frequently been detected in this temperature range (Westbrook, 2010). These occurrences should be investigated further.

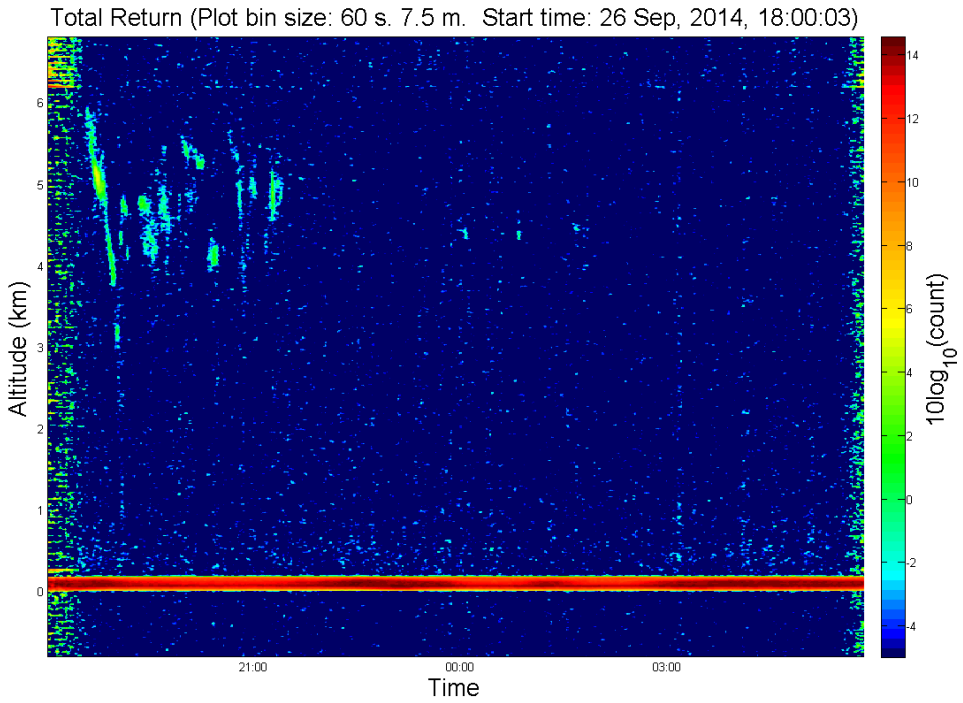

Figure 46: Lidar return strength data for the night of the 26th of September, 2014. It shows a cluster of clouds with a couple of spots of high returned signal strength. The increased noise on the left of this plot is due to sunlight. Times are in local time, not universal time.

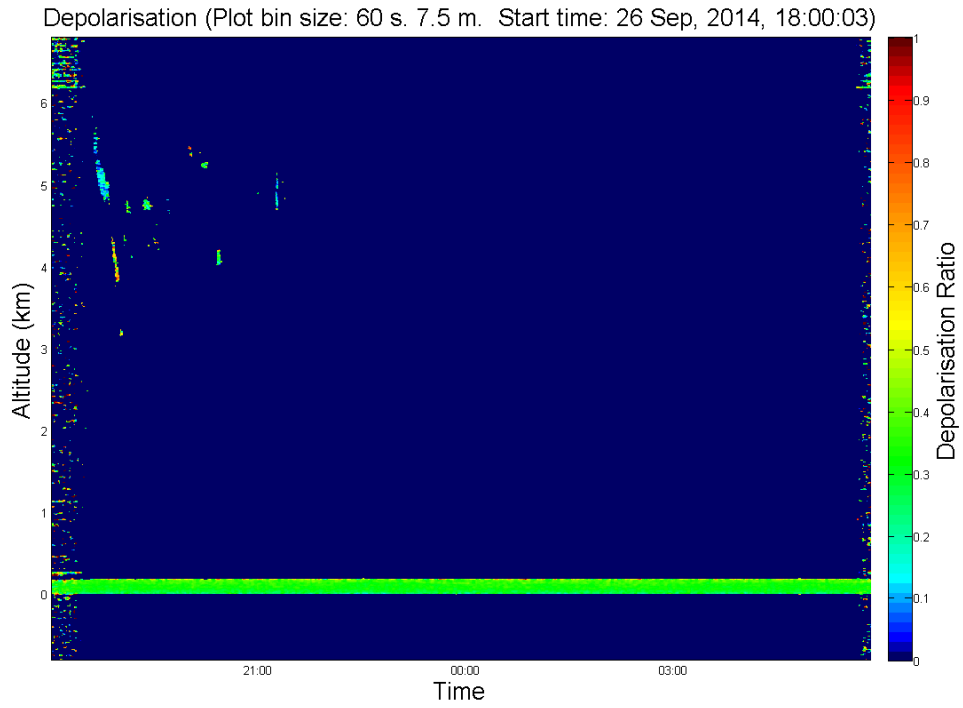

Figure 47: Lidar depolarisation data for the night of the 26th of September, 2014. This time the little clouds returned enough signal to measure a depolarisation ratio. These depolarisation ratio says they are ice clouds. The couple of spots with strong return and low depolarisation are likely composed of horizontally aligned hexagonal plate crystals. Times are in local time, not universal time.

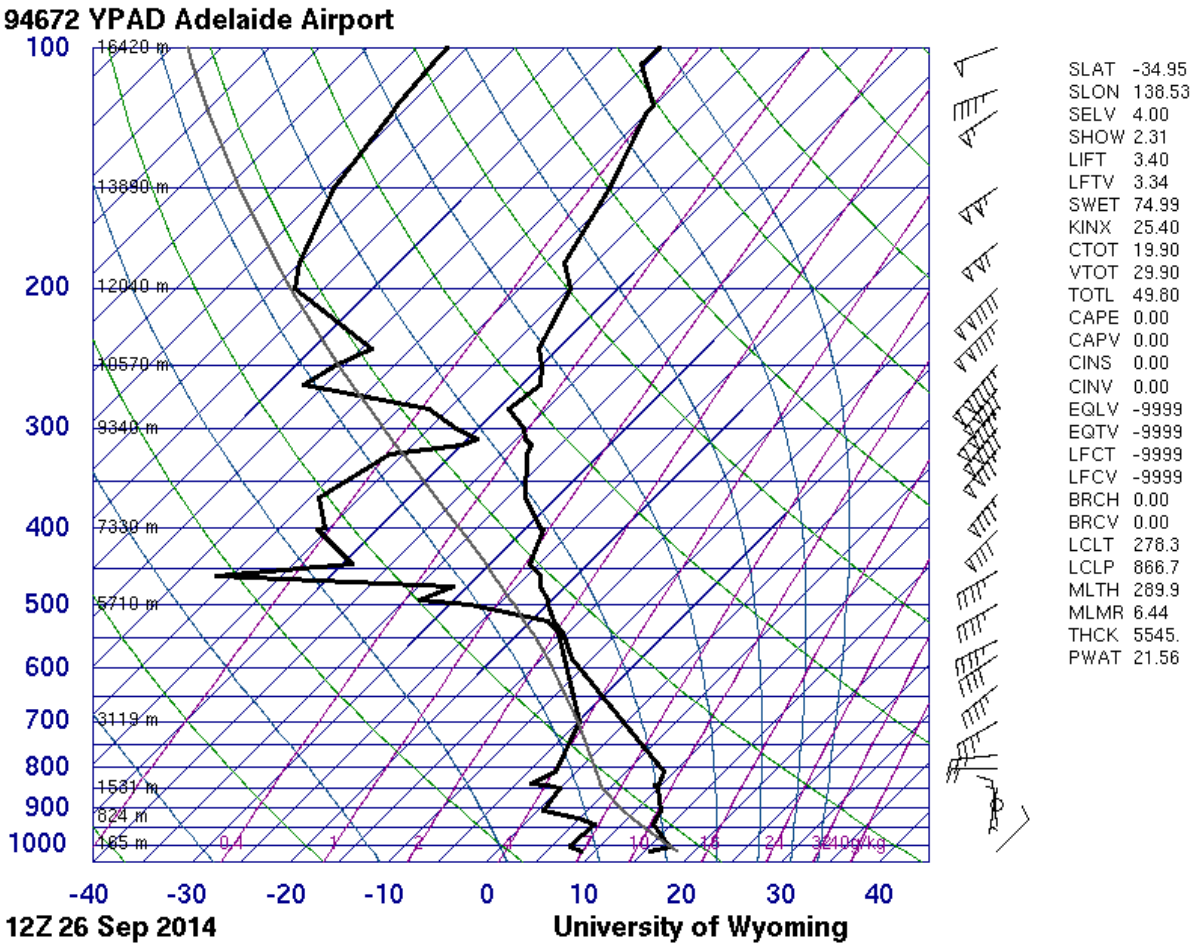

Figure 48: The radiosonde data says that clouds are likely between 4 and 5 km, and the temperatures are between -10 and -20°C, again. (Source: http://weather.uwyo.edu/upperair/sounding.html)

3.4: Chapter Summary

This chapter described the addition of the polarisation measurement equipment to the lidar and the changes made to the software. A summary of three months of data was presented, which showed that the range of the lidar had been reduced. Several case studies of ice detections were presented to show what was gained when the range was lost. Depolarisation values were clearer than expected, only becoming too faint around 6 km which is 1 km below where the return signals are below the background noise. The loss of range however, means that cirrus clouds cannot be detected. Many instances of supercooled water clouds and horizontally oriented crystals were detected.

4: Lidar Simulation

In this chapter a polarimetric lidar simulation is described. Some results from the simulation are presented at the end.

4.1: Background

To complement the work on the lidar, a polarimetric lidar simulation was written. The aim of this was to model the returns from theoretical clouds composed of specific crystal shapes and sizes. This was to help understand how different parameters affect the returned signal and provide a tool for determining the cloud properties from the lidar signal. A newly made database of modelled scattering properties of ice crystals was obtained, covering a wide range of wavelengths, crystals sizes and shapes including aggregates, and also models three different levels of surface roughness (Yang *et al.,* 2013). The lidar simulation was written in Matlab but later moved to C++ when more speed was required. The most significant shortcut is the reduction of the laser divergence angle to zero, which greatly increases the number of photons "detected".

The final simulation program takes around 50 hours per 125 nJ pulse (5×10^{11} photons) per optical thickness of cloud to run. A single pulse run of a 1 km thick cloud of bullet rosettes and one of plates have been run, these having optical thicknesses of 1.1 and 1.5 respectively. Bullet rosettes and plate crystals were chosen to be modelled as they are common constituents of cirrus clouds. With these data an estimate was made of the minimum number of photon detections required to determine the form of the return signal, is around 200 photon detections. For the above clouds, this is around 2% of a pulse and would only take 1 hour and 1.5 hours to run, instead of 55 hours and 80 hours, respectively. The program 'sim5' was written which will simulate photons until 200 detections have been made. 500 detections would be a safer amount to be sure of the results. However, this leaves the runtime at 3 hours, which is too long due to the large number of variations in crystal shape, size and density that would need to be simulated.

4.2: Simulation Description

The scattering simulation is split into three programs. The first one is called ‘build’, which reads phase matrix data that has been pre extracted from the Yang, 2013 dataset, and resample it into equal probability bins. These are then resaved into new files to be read by the main simulation program. The new files are much larger than the original data files, but they are in a form that the main program can use quickly, and this saves the need to resample them for each simulation run. The ‘build’ program needs 5 data files to read from, all of which contain space/tab delimited, 1.E format exponential values. The first file, called ‘angles.txt’ contains the angles in degrees which the values in the other files correspond to. ‘matrix11.txt’, ‘matrix12.txt’, ‘matrix22.txt’ and ‘matrix33.txt’ contain the *P11*, *P12*, *P22* and *P33* phase matrix values of the scatterer being modelled. The output files ‘scattering.txt’, ‘repolarisation.txt’, ‘depolarisation.txt’ and ‘oblique.txt’ contain the resampled scattering values needed for the main program.

The second program is called ‘sim’, and is the main part of the simulation (Figure 49). It loads the resampled phase matrix data created by ‘build’ and runs according to the parameters set in the settings file ‘settings.txt’. The ‘sim’ program also requires an ‘iscat.txt’ file which contains the values from the ‘isca.dat’ file relevant for the scatterer. The ‘sim’ program outputs the properties of the returned photons into three files. One for all down scattered photons ‘downscattered.txt’, one for all down scattered photons that leave the cloud inside the field of view of the receiver ‘infov.txt’ and one for all the photons caught by the receiver ‘detected.txt’. These properties include the total path length the photon travelled, its displacement from origin, the number of times it scattered and its polarisation state.

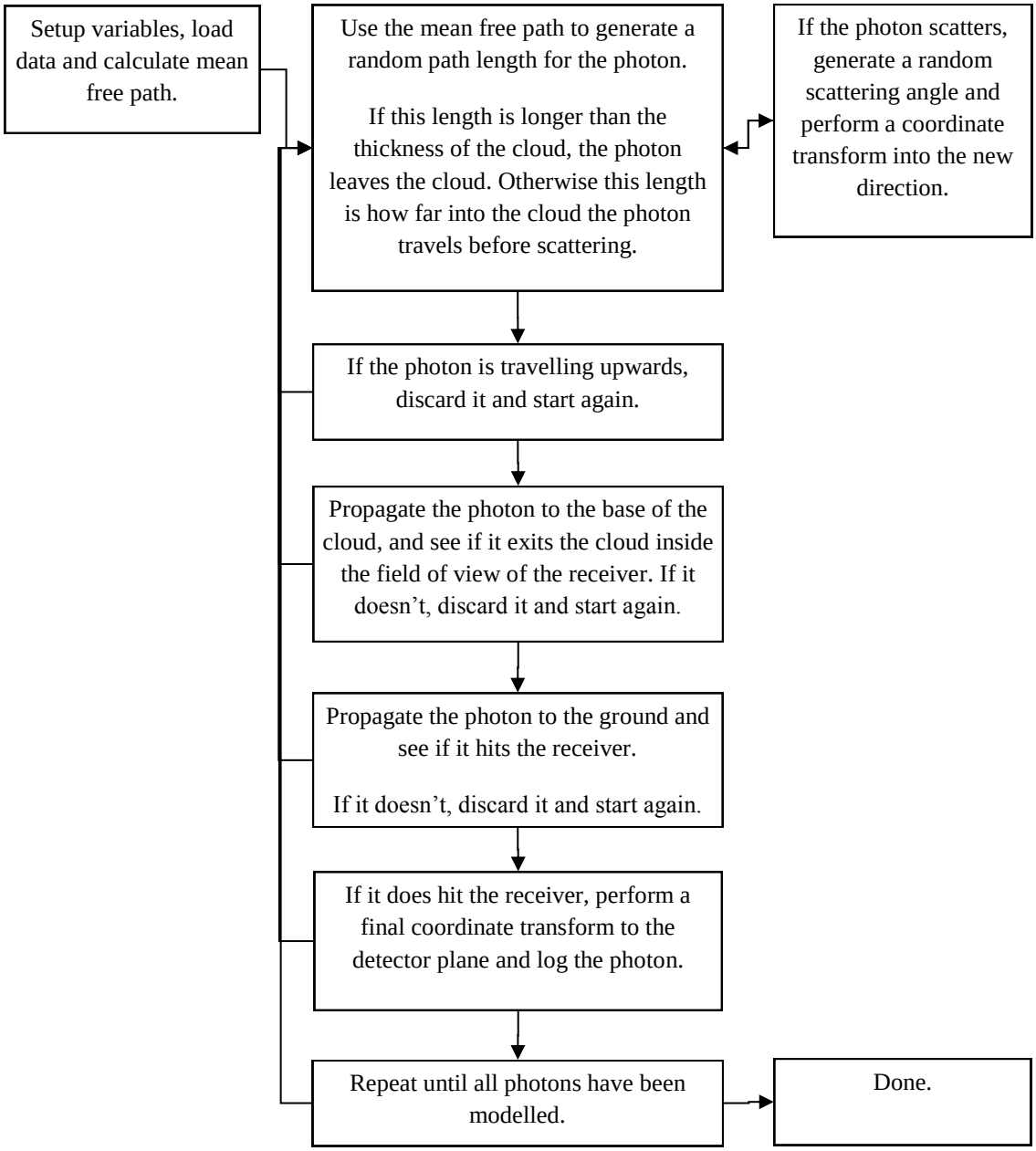

Figure 49: Flowchart describing the main steps of the lidar simulation. Starts in the top left.

To simulate the scattering of photons in a cloud, start with an $I = Q = 1$, $U = V = 0$ state (See A1: Stokes Parameters, page 70). Then apply the appropriate matrix to our photon's Stokes Vector each time it scatters, until the final state is obtained. Since only one photon is modelled at a time, I should remain at 1 after each scatter event. This makes the P11 function a description of the probability of the photon scattering from 0 to 180 degrees. Also, since there are no cross terms between I, Q and U, V and only the final state of Q is sought, it appears that U and V can be ignored.

However, the Stokes Parameters *Q*, *U* and *V* are dependent on the reference frame and more importantly, the scattering plane of each event. If the scattering planes of two scattering events are not parallel then a change of coordinates on the Stokes parameters between these events is needed. This can convert *Q* (horizontal-vertical) polarisation into *U* (oblique) polarisation and vice versa. So the *U* value as well as the *Q* value must be retained in the calculations, otherwise a change of coordinates with an angle of 45 degrees would cause the simulation to lose all polarisation information. This may mean that the *V* value must also be retained as *U* and *V* have cross terms in the scattering matrix. For a single scattering event, this is not the case. A single scattering event can create some *V* polarisation, but it would take a second scattering event for this to make a contribution to *Q*. In multiple scattering cases, the contribution to *Q* from *V* depends on the magnitude of the *P34* term, which is usually nearly 0 in the directions near 0 degrees and 180 degrees and photons scattering in directions away from these leave the field of view of the receiver and are not detected.

The final part is the ’process.m’ matlab program, which takes the data from ‘detected.txt’ and clumps the data into height bins of the specified width. This is output as four vectors: the total return count, the parallel return count, the perpendicular return count and the depolarisation ratio. These data can then be displayed or processed as desired.

4.3: Simulation Results

The simulation was run for a whole 125 nJ pulse of 5×10^{11} photons with a wavelength of 830 nm and no beam divergence, into a 1 km thick cloud of 30000 bullet rosettes per cubic metre. The cloud base is at 10 km, crystals are 250 microns wide, detector aperture is 35 cm and field of view is 1.3 mrad. 117000 photons were detected from this pulse, which means only around one photon per 4 million was detected (for isotropic scattering 1 return per 3000 is expected). The total returned signal is shown in (Figure 50), which shows the signal decreases exponentially with depth into the cloud. The data was split into single and multiply scattered photons to illustrate their differing properties (Figure 51). As expected, single scattered photons return an exponential decay through the cloud. The multiply scattered photons show an exponential increase in return strength for the first 200 m of the cloud, and then appear constant until the cloud tops.

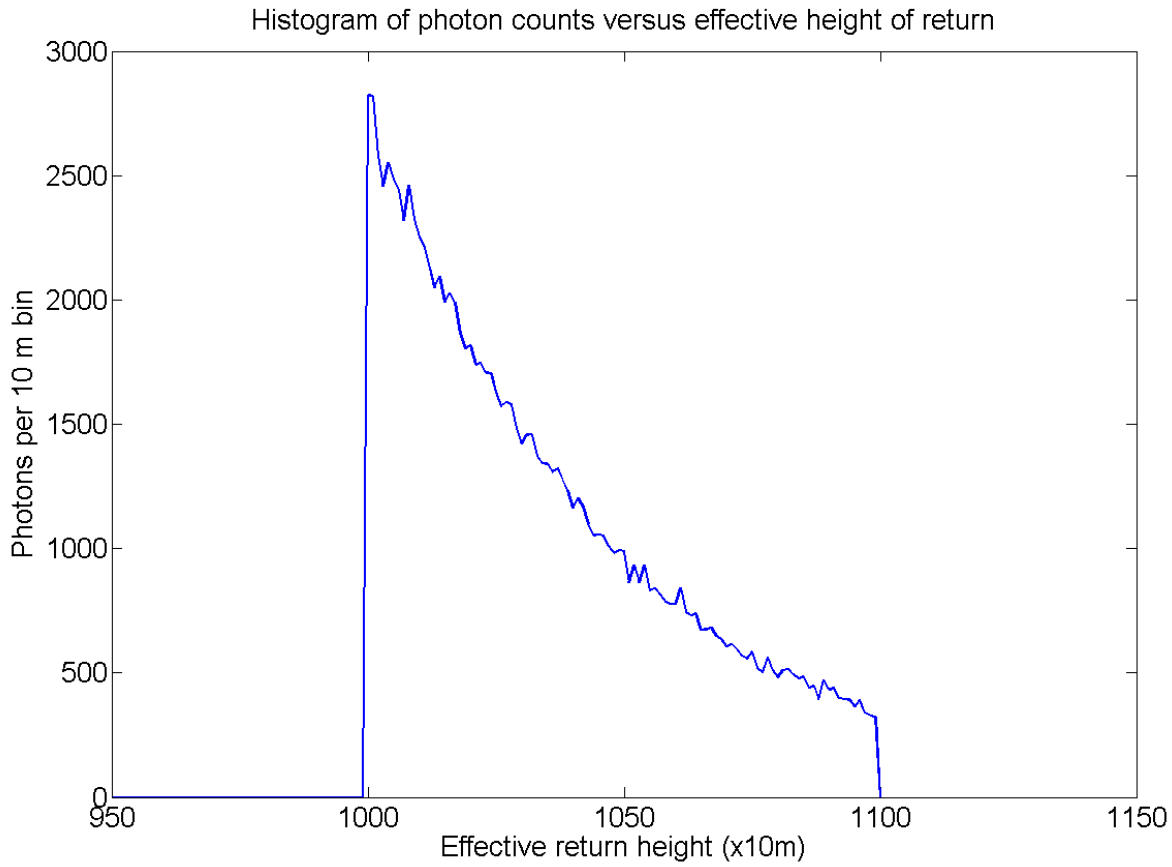

Figure 50: Simulated return from a 1 km thick cloud of bullet rosettes (scattering properties from the Yang (2013) dataset) with a base height of 10 km. It shows the number of detected photons decreasing exponentially from deeper within the cloud.

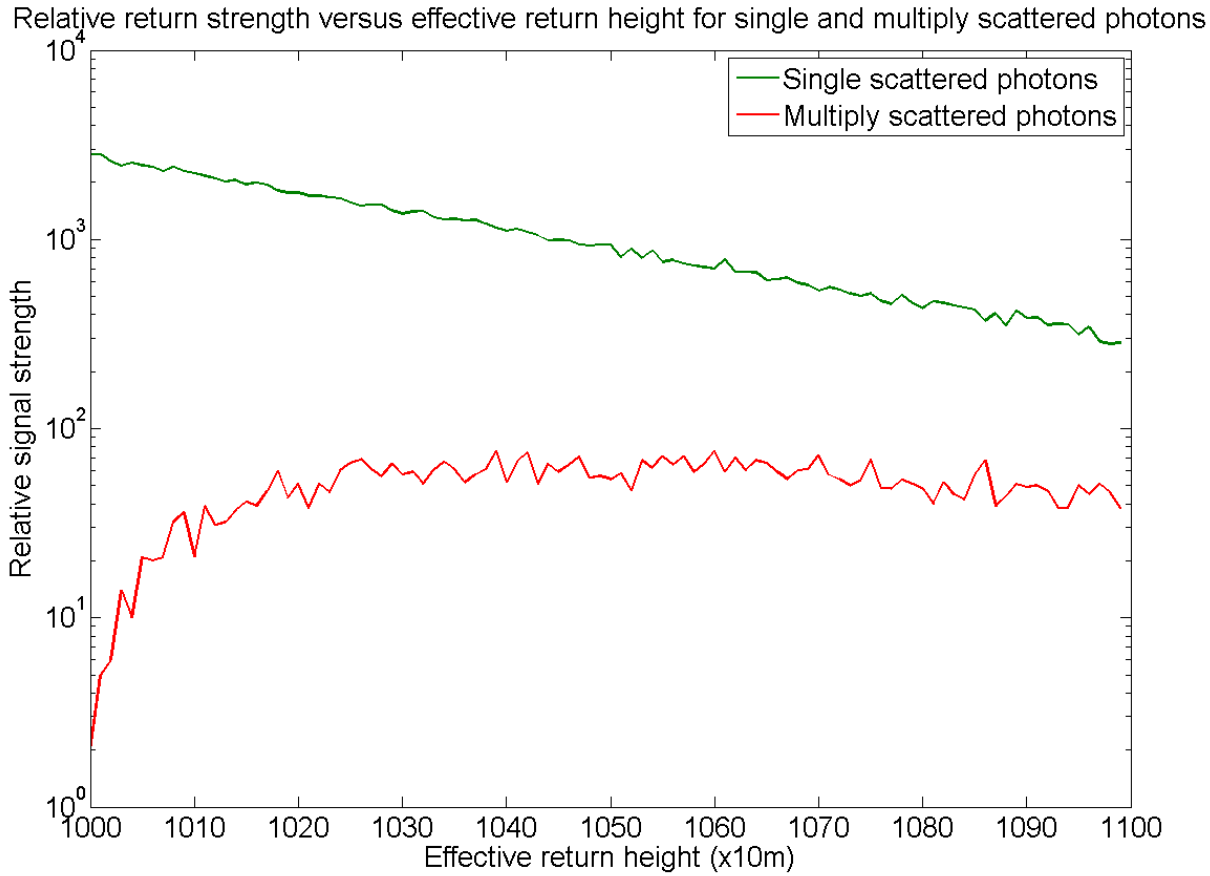

Figure 51: Simulated return from a 1 km thick cloud of bullet rosettes (scattering properties from the Yang (2013) dataset) with a base height of 10 km. Data is split into contributions from single and multiply scattered photons. Relative signal strength plotted on a logarithmic axis for clarity. It shows that the single scattering return decreases with increasing depth through the cloud, while the multiple scattering return initially is increasing and then levels off.

When we compare the depolarisation ratios given by the single and multiply scattered photons, we see that each component is constant throughout the cloud (Figure 52). The single scattered photons give the expected depolarisation ratio of 0.59, while the multiply scattered photons give a depolarisation ratio of around 0.8. While both of the values remain constant, the changing relative strength of the single and multiply scattered photon signals cause the depolarisation ratio to gradually increase with increasing height inside the cloud. In this example, multiple scattering increases the depolarisation ratio by 2% at the top of the cloud.

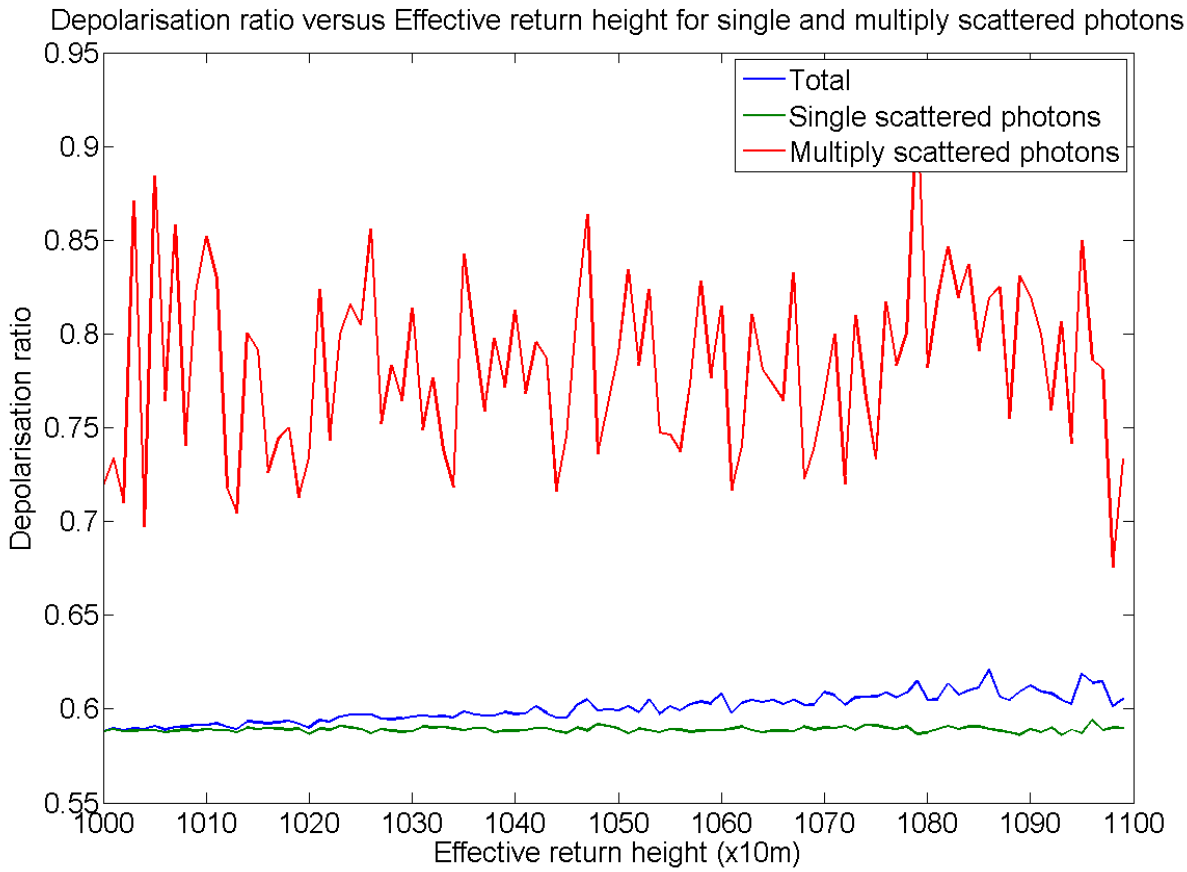

Figure 52: Simulated values of the total depolarisation ratio and the single and multiply scattered components of the depolarisation throughout the thickness of a bullet rosette cloud. While the two components are relatively constant, the total depolarisation ratio changes due to changes in the relative strengths of the two components.

4.4: Chapter Summary

This chapter described a polarimetric lidar simulation, why it was written and how it worked. Some results were given to illustrate the effects of multiple scattering on polarisation measurements. While the simulation produces output consistent with theory, it ran too slowly to play a larger role in the work done. However the program is inherently parallelisable, so the program could be easily adjusted to run efficiently on a multi core system.

5: Discussion

5.1: Review

Over the course of almost two years, many incremental improvements to an existing lidar have been made, with the goal of making measurements of cirrus and mixed phase clouds. All that remains is to increase the pulse energy and reduce the pulse length. The logging range has been increased to include cirrus cloud heights and polarisation discrimination equipment has been installed to determine cloud thermodynamic phase. The control and post processing software has been upgraded to handle the extra range and polarisation data, and the lidar has been set up to run semi-automatically. While it is not enough, the pulse energy has been increased enough to get cirrus cloud detections up to heights of 12 km, before the installation of the polarisation equipment. With the polarisation equipment polarisation measurements have been made up to heights of 5 km. The multiple scattering effect on the depolarisation measurements has been reduced, by adding a field stop to reduce the receiver field of view.

Cloud heights and thicknesses have been verified, within reasonable errors due to the displacement between measurement sites and optical penetration issues, with the CALIOP instrument on the CALIPSO satellite. A lidar simulation program, that includes multiple scattering and polarisation tracking, was written. Initial results are reasonable, though it takes too long to run without some oversimplifications being made. Some optical thicknesses and lidar ratio values have been calculated; however these have not been verified and are likely contaminated due to their proximity to the ground level aerosol layer. Six months of nightly cloud measurements, three months of which have depolarisation values, have been collected.

Initial results have shown that warm liquid clouds, supercooled liquid clouds, aligned plate crystals and randomly aligned crystals all occur between 2 and 4 km heights at this location. Measurements are ongoing and these data can be used to test model predictions about the frequencies of these different cloud compositions.

5.2: Proposed Further Changes

While much has been achieved in this project, the main goals have not been reached. With the final lidar setup, the highest cloud detection has been made at 8 km. The highest depolarisation ratio measurement was made at 5 km. The highest clear air return, which can be used for calculating optical thicknesses and lidar ratios, was 1500 m. The main goal was to be able to be able to make measurements of cirrus clouds, which occur up to the tropopause, up to 15 km high in summer at the study location, and to measure thermodynamic phase in mixed phase clouds, which could occur at heights of up to 10 km at the study location. To meet these goals requires a doubling or tripling of the current range. This could be achieved by increasing the laser pulse energy to ~10 times the current energy, around 1 µJ. The lidar would then be able to make depolarisation measurements up to the tropopause. It is also strongly desirable to reduce the pulse length to improve the vertical resolution. The current 1 µs pulse gives a resolution of 150 m. This is acceptable for detecting clouds and making depolarisation measurements of clouds. But as we wish to examine the internal structure of mixed phase clouds, this will not be sufficient. To make better measurements of internal structure, the pulse length could be reduced to as low as 50 ns to match the 7.5 m resolution of the logger.

Further improvements to the signal to noise ratio would provide extra functionality: To be able to use the transmission technique for calculating optical thicknesses and the inversion technique for calculating lidar ratios, we would need around 10 µJ pulses. To be able to detect and measure sub visual cirrus clouds would require around 100 µJ pulses. While studying aerosol layers would require around 1 mJ pulses. Daylight operation would also be possible with a significant increase in pulse energy. Also, any increase in the signal to noise ratio will increase the ability to detect clouds above other clouds. Instead of just increasing the laser pulse energy, another method for increasing the signal to noise ratio that should be considered is to reduce the divergence of the laser beam and the field of view of the receiver more. This reduces the amount of sky being ‘seen’ by the detector and thus reduces the amount of background light noise, and the narrower beam divergence makes it more likely for scattered photons to get back to the detector, as shown by the lidar simulation.

While the cost of new equipment is the main limitation to improving the signal to noise ratio, if increasing the laser pulse energy is considered, then safety issues need to be addressed as well. There are three locations where exposure to the laser could occur; in the lab, on the roof courtyard and in the sky above the building. For the lab, appropriate eye protection is available that should be sufficient for a significant increase in output power, though connecting the laser to the door interlock would be advised. For the roof space, any increase in laser power would make the danger category above class 1M. However, the existing access restrictions and only at night operation of the laser, combined with needing to climb onto a high raised section to be in the path of the beam, and suitable warning signs should be enough to cover any risk. In the case of exposure to the laser while flying above the building, any increase in laser pulse energy need to be above a factor of 100, to be of any danger. This is because of the increased beam size and the inability of anybody to stay stationary long enough to catch more than one pulse in their eye. The laser wavelength outside of the visible also means that is isn't possible to dazzle a pilot with the laser. The width of the laser beam could also be increased to reduce its danger.

Although not discussed in this thesis, the use of a laser brings many Health, Safety and Welfare issues. Safety improvements could also be made by changing the wavelength of the laser, though this would incur additional cost due to requiring a new filter (and possibly a new photomultiplier tube). The laser safety standards rate 830 nm as being in the most dangerous part of the spectrum for eye damage. This is due to the eye being able to focus this wavelength to a point, but as it is outside the visible range, no aversion reflex will make you blink to protect your eye. If the beam was to remain invisible, to avoid the risk of dazzling aircraft pilots, then changing the wavelength to 1064 nm would reduce the laser's eye danger by a factor of 5, whereas the wavelength of 355 nm would reduce the eye danger by a factor of 4000. This large increase in safety is because 355 nm is not well focussed or transmitted by the human lens, so the energy is never concentrated on a small area; however it can cause fluorescence in the eye which could dazzle. Note that these danger ratings only apply to damage to the eye and these different wavelengths may be more dangerous to skin.

These upper limits due to the safety of the energy pulse and the resolution of the logger give an upper limit on the laser peak power of 500 W, with 25 µJ pulses of 50 ns length (7.5 m resolution). To produce useful data for studying cloud properties would require a peak power of at least 50 W, with 12.5 µJ pulses of 250 ns (40 m resolution).

5.3: Proposed Future Measurements

Once the lidar has sufficient resolving power, its data could be used to study a variety of things. The simplest of these is to collect a year or more of data and compile a climatology of the clouds above Adelaide. In addition to the geometric properties of the clouds, the depolarisation ratio and potentially the optical thickness, thermodynamic phase and lidar ratios, it has been shown to be possible to derive liquid particle size and content of a cloud from the depolarisation measurements (Kim and Lee, 2014). This can be investigated and potentially applied to the data from this lidar. The colocation of a radar instrument would also increase the range and accuracy of properties that can be derived. Adelaide's location between the inland deserts and Indian/Southern Ocean would allow for investigating the effects of these very different aerosol sources on cloud formation. This would be done by running back trajectories, using the Bureau of Meteorology's wind data, to determine the predominate source of aerosols in a cloud layer. Also, with the use of a better computer, the lidar simulation could be run to compile a database/look up table that might be able to narrow down size/shape of the cloud particles detected.

Appendices

A1: Stokes Parameters

The polarisation state of photons can be described by the Stokes parameters (*I, Q, U,* and *V*). *I* is the total intensity, *Q* is the degree of linear polarisation in the horizontal/vertical direction, *U* is the degree of linear polarisation in the 45 degrees off axis direction, and *V* is the degree of circular polarisation (Mishchenko *et al*., 2000). They are defined as positive *Q* being horizontal polarisation, and negative *Q* being vertical polarisation, similar with *U*. These values depend on the reference frame. In terms of these parameters, the depolarisation ratio is given by:

$$\delta = \frac{I - Q}{I + Q}$$

Any transformation applied to light can have its effect on the Stokes parameters described by a Mueller matrix, which acts on the Stokes vector and is 4x4 in size. A Mueller matrix describing a scattering event looks like (Mishchenko *et al*., 2000):

$$\begin{pmatrix} I' \\ Q' \\ U' \\ V' \end{pmatrix} = \begin{pmatrix} P11 & P12 & 0 & 0 \\ P12 & P22 & 0 & 0 \\ 0 & 0 & P33 & P34 \\ 0 & 0 & -P34 & P44 \end{pmatrix} \mathrm{X} \begin{pmatrix} I \\ Q \\ U \\ V \end{pmatrix}$$

These 6 independent P values are dependent on the properties of the scatterer and the scattering angle relative to its incident direction.

Another useful transformation is that used to transform the values to a new reference frame, such as is needed between two scattering events that have non-parallel scattering planes. This takes the form of:

$$\begin{pmatrix} I' \\ Q' \\ U' \\ V' \end{pmatrix} = \begin{pmatrix} 1 & 0 & 0 & 0 \\ 0 & \cos(2\theta) & \sin(2\theta) & 0 \\ 0 & -\sin(2\theta) & \cos(2\theta) & 0 \\ 0 & 0 & 0 & 1 \end{pmatrix} \mathrm{X} \begin{pmatrix} I \\ Q \\ U \\ V \end{pmatrix}$$

Where θ is the change in azimuthal angle between the two scattering planes.

Bibliography

1. C. Allemand, "Depolarization Ratio Measurements in Raman Spectrometry," *Appl. Spectrosc. 24, 348-353 (1970).*
2. A. Ansmann, M. Riebesell, U. Wandinger, C. Weitkamp, E. Voss, W. Lahmann, W. Michaelis. Combined raman elastic-backscatter LIDAR for vertical profiling of moisture, aerosol extinction, backscatter, and LIDAR ratio. *Applied Physics B, July 1992, Volume 55, Issue 1, pp 18-28, DOI:10.1007/BF00348608*
3. Anthony J. Baran, From the single-scattering properties of ice crystals to climate prediction: A way forward. *Atmospheric Research, Volume 112, August 2012, Pages 45-69, ISSN 0169-8095, http://dx.doi.org/10.1016/j.atmosres.2012.04.010.*
4. Chen, W. N., Chiang, C. W., and Nee, J. B.: Lidar ratio and depolarization ratio for cirrus clouds. *Appl. Optics, 41, 6470–6476, doi:10.1364/AO.41.006470, 2002.*
5. Daniel J. Cziczo, Karl D. Froyd, Corinna Hoose, Eric J. Jensen, Minghui Diao, Mark A. Zondlo, Jessica B. Smith, Cynthia H. Twohy, and Daniel M. Murphy, Clarifying the Dominant Sources and Mechanisms of Cirrus Cloud Formation. *Science 14 June 2013: 340 (6138), 1320-1324.Published online 9 May 2013 [DOI:10.1126/science.1234145]*
6. Das, S. K, S. S. Das, C-W. Chiang, J-B. Nee, (2013), Descending cirrus associated with planetary scale disturbance: An observational study from lidar, radiosonde and reanalysis data. *Journal of Atmospheric and Solar-Terrestrial Physics, Volume 104, November 2013, Pages 137-147, ISSN 1364-6826,* http://dx.doi.org/10.1016/j.jastp.2013.08.019.
7. Dionnisi, D., P. Keckhut, G. L. Liberti, F. Cardillo, F. Congeduti (2013), Mid-latitude cirrus classification at Rome Tor Vergata through a multi-channel Raman–Mie–Rayleigh lidar. *Atmospheric Chemistry and Physics Discussions, Volume: 13 Issue: 4 Pages: 9615-9652 DOI: 10.5194/acpd-13-9615-2013.*
8. Dupont, J.-C., M. Haeffelin, Y. Morille, V. Noël, P. Keckhut, D. Winker, J. Comstock, P. Chervet, and A. Roblin *(2010),* Macrophysical and optical properties of midlatitude cirrus clouds from four ground-based lidars and collocated CALIOP observations. *J. Geophys. Res., 115, D00H24, doi:10.1029/2009JD011943.*
9. Franklin, C. N., Z. Sun, D. Bi, M. Dix, H. Yan, and A. Bodas-Salcedo (2013), Evaluation of clouds in ACCESS using the satellite simulator package COSP: Global,

seasonal, and regional cloud properties. *J. Geophys. Res. Atmos., 118, 732–748, doi:10.1029/2012JD018469.*

10. Hlavka, D. L., J. E. Yorks, S. A. Young, M. A. Vaughan, R. E. Kuehn, M. J. McGill, and S. D. Rodier *(2012),* Airborne validation of cirrus cloud properties derived from CALIPSO lidar measurements: Optical properties, *J. Geophys. Res., doi:10.1029/2011JD017053*

11. Hoareau, C., P. Keckhut, V. Noel, H. Chepfer (2013), A decadal cirrus clouds climatology from ground-based and spaceborne lidars above south of France (43.9° N–5.7° E). *Atmospheric Chemistry and Physics Discussions, Volume: 13 Issue: 3 Pages: 6379-6417 DOI: 10.5194/acpd-13-6379-2013.*

12. Hu, Y. *(2007),* Depolarization ratio–effective lidar ratio relation: Theoretical basis for space lidar cloud phase discrimination, *Geophys. Res. Lett., 34, L11812, doi:10.1029/2007GL029584.*

13. Intergovernmental Panel on Climate Change. (2007), Climate change 2007: impacts, adaptation and vulnerability. *ISBN: 9780521705974*

14. Josset, D., J. Pelon, A. Garnier, Y. Hu, M. Vaughan, P.-W. Zhai, R. Kuehn, and P. Lucker *(2012),* Cirrus optical depth and lidar ratio retrieval from combined CALIPSO-CloudSat observations using ocean surface echo. *J. Geophys. Res., 117, D05207, doi:10.1029/2011JD016959.*

15. Kanitz, T., P. Seifert, A. Ansmann, R. Engelmann, D. Althausen, C. Casiccia, and E. G. Rohwer *(2011),* Contrasting the impact of aerosols at northern and southern midlatitudes on heterogeneous ice formation. *Geophys. Res. Lett., 38, L17802, doi:10.1029/2011GL048532*

16. Klett, J., "Stable Analytical Inversion Solution for Processing Lidar Returns," *Appl. Opt. 20, 211 (1981).*

17. Klett J., "Extinction boundary value algorithms for lidar inversion," *Appl. Opt. 25, 2462-2464 (1986).*

18. Kim, D. and J. Lee, "Measuring cloud droplet effective radius and liquid water content using changes in degree of linear polarization along cloud depth," *Opt. Lett. 39, 3378-3381 (2014). http://dx.doi.org/10.1364/OL.39.003378*

19. Yumi Kim, Sang-Woo Kim, Man-Hae Kim, Soon-Chang Yoon, Geometric and optical properties of cirrus clouds inferred from three-year ground-based lidar and CALIOP measurements over Seoul, Korea. *Atmospheric Research, Volume 139, 15*

March 2014, Pages 27-35, ISSN 0169-8095, http://dx.doi.org/10.1016/j.atmosres.2013.12.016.

20. Susan Gabriela Lakkis, Mario Lavorato, Pablo Osvaldo Canziani, Héctor Lacomi, (2011), Cirrus Clouds and Multiple Tropopause Events over Buenos Aires. *Atmospheric and Climate Sciences, Volume: 01 Issue: 03 Pages: 113-119 DOI:10.4236/acs.2011.13013*

21. Susan Gabriela Lakkis, Mario Lavorato, Pablo Osvaldo Canziani, Monitoring cirrus clouds with lidar in the Southern Hemisphere: A local study over Buenos Aires. 1. Tropopause heights. *Atmospheric Research, Volume 92, Issue 1, March 2009, Pages 18-26, ISSN 0169-8095,* http://dx.doi.org/10.1016/j.atmosres.2008.08.003.

22. Lohmann, U., K. Broekhuizen, R. Leaitch, N. Shantz, and J. Abbatt (2004), How efficient is cloud droplet formation of organic aerosols? *Geophys. Res. Lett., 31, L05108, doi:10.1029/2003GL018999.*

23. Manoj, M.G., P.C.S. Devara, Y. Jaya Rao, S.M. Sonbawne, Lidar investigation of aerosol–cloud–precipitation interactions over a tropical monsoon environment: Recharging of atmosphere. *Journal of Atmospheric and Solar-Terrestrial Physics, Volume 93, February 2013, Pages 80-86, ISSN 1364-6826,* http://dx.doi.org/10.1016/j.jastp.2012.10.009.

24. M. I. Mishchenko, J. W. Hovenier, and L. D. Travis, Light Scattering by Nonspherical Particles *(Academic, 2000).*

25. Minnis, P., S. T. Bedka, D. P. Duda, K. M. Bedka, T. Chee, J. K. Ayers, R. Palikonda, D. A. Spangenberg, K. V. Khlopenkov, and R. Boeke *(2013),* Linear contrail and contrail cirrus properties determined from satellite data. *Geophys. Res. Lett., 40, 3220–3226, doi:10.1002/grl.50569.*

26. Nazaryan, H., M. P. McCormick, and W. P. Menzel (2008), Global characterization of cirrus clouds using CALIPSO data. *J Geophys. Res., 113, D16211, doi:10.1029/2007JD009481.*

27. Platt, C. M. R. *(1973),* Lidar and radiometric observations of cirrus clouds, *J. Atmos. Sci., 30, 1191–1204, doi:10.1175/1520-0469(1973)030<1191:LAROOC>2.0.CO;2.*

28. Robock, A. *(2010),* New START, Eyjafjallajökull, and Nuclear Winter, Eos Trans. *AGU, 91(47), 444–445, doi:10.1029/2010EO470004.*

29. Rosefeld, D. and Woodley, W. L. *(2000)* Deep convective clouds with sustained supercooled liquid waterdown to −37.5 ◦C. *Nature, 405, 440–442 doi:10.1038/35013030*

30. Rotstayn, L. D., Keywood, M. D., Forgan, B. W., Gabric, A. J., Galbally, I. E., Gras, J. L., Luhar, A. K., McTainsh, G. H., Mitchell, R. M. and Young, S. A. *(2009),* Possible impacts of anthropogenic and natural aerosols on Australian climate: a review. *Int. J. Climatol., 29: 461–479. doi: 10.1002/joc.1729*

31. Kenneth Sassen and Byung Sung Cho, 1992: Subvisual-Thin Cirrus Lidar Dataset for Satellite Verification and Climatological Research. *J. Appl. Meteor., 31, 1275–1285. doi: http://dx.doi.org/10.1175/1520-0450(1992)031<1275:STCLDF>2.0.CO;2*

32. Sassen, K., and Z. Wang *(2008),* Classifying clouds around the globe with the CloudSat radar: 1-year of results. *Geophys. Res. Lett., 35, L04805, doi:10.1029/2007GL032591*.

33. Sassen, K., and J. Zhu *(2009),* A global survey of CALIPSO linear depolarization ratios in ice clouds: Initial findings. *J. Geophys. Res., 114, D00H07, doi:10.1029/2009JD012279.*

34. Matthew D. Shupe, John S. Daniel, Gijs de Boer, Edwin W. Eloranta, Pavlos Kollias, Edward P. Luke, Charles N. Long, David D. Turner, and Johannes Verlinde, *(2008):* A Focus On Mixed-Phase Clouds. *Bull. Amer. Meteor. Soc., 89, 1549–1562. doi: http://dx.doi.org/10.1175/2008BAMS2378.1*

35. Suzuki, J., M. Fujiwara, T. Nishizawa, R. Shirooka, K. Yoneyama, M. Katsumata, I. Matsui, and N. Sugimoto *(2013),* The occurrence of cirrus clouds associated with eastward propagating equatorial n = 0 inertio-gravity and Kelvin waves in November 2011 during the CINDY2011/DYNAMO campaign. *J. Geophys. Res. Atmos., 118, 12,941–12,947, doi:10.1002/2013JD019960.*

36. Tan, I., T. Storelvmo, and Y.-S. Choi *(2014),* Spaceborne lidar observations of the ice-nucleating potential of dust, polluted dust and smoke aerosols in mixed-phase clouds. *J. Geophys. Res. Atmos., 119, 6653–6665, doi:10.1002/2013JD021333.*

37. Thorsen, T. J., Q. Fu, J. M. Comstock, C. Sivaraman, M. A. Vaughan, D. M. Winker, and D. D. Turner *(2013),* Macrophysical properties of tropical cirrus clouds from the CALIPSO satellite and from ground-based micropulse and Raman lidars. *J. Geophys. Res. Atmos., 118, 9209–9220, doi:10.1002/jgrd.50691.*

38. Twomey, S. *(1991),* Aerosols, clouds and radiation. *Atmospheric Environment, Volume 25, Issue 11, Pages 2435–2442, doi:10.1016/0960-1686(91)90159-5.*

39. Mark A. Vaughan, Kathleen A. Powell, David M. Winker, Chris A. Hostetler, Ralph E. Kuehn, William H. Hunt, Brian J. Getzewich, Stuart A. Young, Zhaoyan Liu, and Matthew J. McGill, *2009:* Fully Automated Detection of Cloud and Aerosol Layers in

the CALIPSO Lidar Measurements. *J. Atmos. Oceanic Technol., 26, 2034–2050. doi: http://dx.doi.org/10.1175/2009JTECHA1228.1*

40. Jin Wang, Lei Zhang, Jianping Huang, Xianjie Cao, Ruijin Liu, Bi Zhou, Hongbin Wang, Zhongwei Huang, Jianrong Bi, Tian Zhou, Beidou Zhang, Tengjiao Wang, Macrophysical and optical properties of mid-latitude cirrus clouds over a semi-arid area observed by micro-pulse lidar. *Journal of Quantitative Spectroscopy and Radiative Transfer, Volume 122, June (2013), Pages 3-12, ISSN 0022-4073,* http://dx.doi.org/10.1016/j.jqsrt.2013.02.006.

41. Westbrook, C. D., Illingworth, A. J., O'Connor, E. J. and Hogan, R. J. *(2010),* Doppler lidar measurements of oriented planar ice crystals falling from supercooled and glaciated layer clouds. *Q.J.R. Meteorol. Soc., 136: 260–276. doi: 10.1002/qj.528*

42. Yang, P., Bi, L., Baum, B. A., Liou, K., Kattawar, G. W., Mishchenko, M. I., & Cole, B. *(2013).* Spectrally Consistent Scattering, Absorption, and Polarization Properties of Atmospheric Ice Crystals at Wavelengths from 0.2 to 100 μm. *Journal Of The Atmospheric Sciences, 70(1), 330-347. doi:10.1175/JAS-D-12-039.1*